



**ROYAL INSTITUTE
OF TECHNOLOGY**

Experimental and analytical study of thermal mixing at reactor conditions

MATTIA BERGAGIO

Doctoral Thesis
Stockholm, Sweden 2018

TRITA-SCI-FOU 2018:45
ISBN 978-91-7873-001-8

AlbaNova
Roslagstullsbacken 21
10691 Stockholm
Sweden

Akademisk avhandling som med tillstånd av Kungl Tekniska högskolan framlägges till offentlig granskning för avläggande av teknologie doktorexamen i kärnenergi-teknik torsdagen den 6:e december 2018 kl 13.00 i FB53, AlbaNova, Stockholm.

© Mattia Bergagio, November 2018

Tryck: Universitetsservice US AB

Abstract

High-cycle thermal fatigue due to turbulent mixing of streams at distinct temperatures is an interdisciplinary issue affecting safety and life extension of existing reactors together with the design of new reactors. It is challenging to model damage and thermal loads arising from the above mixing.

In order to collect vast data sets for the validation of codes modeling turbulent thermal mixing under reactor conditions, temperatures were sampled at the inner surface of the vertical annular volume between two concentric 316LN stainless steel tubes. This annulus simplifies that between control-rod guide tube and stem in Swedish boiling water reactors (BWRs) Oskarshamn 3 and Forsmark 3. In 2008, several stems there were reported as broken or cracked from thermal fatigue. Cold water entered the annulus at 333 K, at axial level $z = 0.15$ m. It moved upward and mixed with hot water, which entered the annulus at 549 K, at $z = 0.80$ m. Pressure read 7.2 MPa. Hot and cold inlet temperatures and pressure match BWR conditions. The thermocouples attached to the inner tube could only acquire inner-surface temperatures at six locations, so the inner tube was translated and rotated about the z -axis to expand the measurement zone.

Mixing inhomogeneity was estimated from such measurements. In the cases examined, the inner-surface temperatures from areas with the highest mixing inhomogeneity show dominant frequencies lower than ten times the inverse of the experiment time.

The uncertainty of this temperature measurement appears to be equal to 1.58 K. A large eddy simulation (LES) of mixing in the above annulus was conducted. Experimental boundary conditions were applied. The conjugate heat transfer between water and tubes was modeled. The wall-adapting local eddy viscosity (WALE) sub-grid model was adopted. A finite element analysis (FEA) of the inner tube was performed using LES pressure and temperature as loads. Cumulative fatigue usage factors (CUFs) were estimated from FEA stress histories. To this end, the rain-flow cycle-counting technique was applied. CUFs are highest between $z = 0.65$ m and $z = 0.67$ m. Cracking is predicted to initiate after 97 h. LES and experimental inner-surface temperatures agree reasonably well in relation to mean values, ranges, mixing inhomogeneity, and critical oscillation modes in areas sensitive to fatigue. LES inner-surface temperatures from areas with the highest CUFs show dominant frequencies lower than ten times the inverse of the simulation time.

A robust, effective iterative algorithm for reconstructing the transient temperature field in the inner tube from redundant boundary data was implemented and verified. Temperature-dependent properties were included. Initial conditions and over-specified boundary data in the inverse problem were perturbed with Gaussian noise to check the robustness of the solving method to noise.

Keywords: High-cycle thermal fatigue, Hilbert-Huang transform, large eddy, WALE, rainflow, inverse heat conduction, adjoint conjugate gradient

Doktorsavhandlingssammanfattning

Termisk högcykelutmattning på grund av turbulent blandning av flöden av olika temperaturer är en tvärvetenskaplig fråga som har bäring på säkerhet, underhåll och livstidsförlängning av kärnkraftverk i drift tillsammans med utvecklingen av nya reaktorer. Det är utmanande att modellera delskador och termiska belastningar som härrör från denna blandning.

För att samla stora datamängder för validering av koder modellerande turbulent termisk blandning vid reaktordriftförhållanden, mättes temperaturer vid den inre ytan av den vertikala annulära (ringformade) kanalen mellan två koncentriska rör i 316LN rostfritt stål. Denna annulära kanal representerar den verkliga geometrin mellan styrstavsledrör och styrstavs förlängare i svenska kokvattenreaktorer (BWR) Oskarshamn 3 och Forsmark 3. Vid dessa reaktorer uppvisade ett antal styrstavs förlängare sprickbildning till följd av termisk utmattning under år 2008. I den annulära kanalen strömmade kallare vattenflöden vid 333 K, vid axiell nivå $z = 0.15$ m. Flödena rörde sig uppåt och blandades med varmare vattenflöden, vilka strömmade i den annulära kanalen vid 549 K, vid $z = 0.80$ m. Trycket sattes till 7.2 MPa. 333 K, 549 K och 7.2 MPa överensstämmer med BWR-förhållanden. Termoelement fastlödda vid det inre röret kunde endast mäta innerytans temperatur på sex platser. För att kunna mäta temperaturen i hela blandningsområdet kunde röret roteras från 0° till 360° och förflyttas vertikalt över en sträcka av 387 mm.

Blandningsinhomogenitet uppskattades från sådana mätningar. I de undersökta fallen visar innerytans temperatur från områden där blandningen är som minst homogen dominerande frekvenser som är lägre än tio gånger inversen till experimenttiden.

Osäkerheten i dessa temperaturmätningar visar sig vara 1.58 K.

En storvirvelsimulering (LES) av blandning i den annulära kanalen utfördes. Experimentella randvillkor applicerades. Den konjugerade värmeöverföringen mellan vatten och rör modellerades. De små virvlarna (oupplösta skalor) approximerades med hjälp av en turbulensmodell kallad WALE, som ger rätt asymptotiskt beteende för turbulent viskositet nära väggen. En finitelementanalys (FEA) av det inre röret utfördes med LES-tryck och temperatur som belastningar. Totala delskador uppskattades från FEA-spänning/tid kurvor. För detta ändamål applicerades regndroppsmetoden. De totala delskadorna når sina högsta värden mellan $z = 0.65$ m och $z = 0.67$ m. Sprickinitiering förväntas inträffa efter 97 timmar. Innerytans CFD-

temperatur är i en rimlig överensstämmelse med experimentella data med avseende på medelvärde, omfång, blandningsinhomogenitet och kritiska svängande modalfunktioner som utgör temperaturtidsserier i områden som är utsatta för utmattning. Innerytans CFD-temperatur från områden med högsta totala delskador visar dominerande frekvenser som är lägre än tio gånger inversen till simuleringstiden. En robust, effektiv, iterativ algoritm för att beräkna det transienta temperaturfältet i det inre röret utifrån överflödiga randdata implementerades och verifierades. Temperaturberoende egenskaper inkluderades. Initiala förhållanden och överflödiga randdata i det inversa problemet stördes av gaussiskt brus för att undersöka lösningsmetodens robusthet mot brus.

List of publications

Publications included in this thesis

- Paper 1. M. Bergagio and H. Anglart. 2017. Experimental investigation of mixing of non-isothermal water streams at BWR operating conditions. *Nuclear Engineering and Design*, 317:158–176.
- Paper 2. M. Bergagio, R. Thiele, and H. Anglart. 2017. Analysis of temperature fluctuations caused by mixing of non-isothermal water streams at elevated pressure. *International Journal of Heat and Mass Transfer*, 104:979–992.
- Paper 3. M. Bergagio, H. Li, and H. Anglart. 2018b. An iterative finite-element algorithm for solving two-dimensional nonlinear inverse heat conduction problems. *International Journal of Heat and Mass Transfer*, 126:281–292.
- Paper 4. M. Bergagio, W. Fan, R. Thiele, and H. Anglart. 2018a. Large eddy simulation of thermal mixing with conjugate heat transfer at BWR operating conditions. Submitted to Nuclear Engineering and Design.

The author’s contribution to the included publications

Paper 1. Mattia Bergagio (MB) wrote the data acquisition code with help from Stefan Rydström. Stellan Hedberg ran the experiments in the HWAT loop. MB wrote the post-processing code. He wrote the paper with feedback from Henryk Anglart (HA).

Paper 2. MB developed the post-processing code. He wrote the paper with feedback from Roman Thiele (RT) and HA.

Paper 3. MB wrote the code and ran the simulations. He wrote the paper with feedback from Haipeng Li and HA.

Paper 4. RT wrote a preliminary version of the paper. He also ran the precursor $k - \varepsilon$ simulation and an LES on a mildly refined mesh. After changing initial

and boundary conditions, water properties, solver parameters and discretization schemes, MB ran a new LES, using a mesh built by Wenyuan Fan (WF). MB ran the FEA of the inner tube and performed the fatigue assessment. He updated the paper, with feedback from HA and WF.

Publications not included in this thesis

- M. Bergagio, S. Hedberg, S. Rydström, and H. Anglart. 2015. Instrumentation for temperature and heat flux measurement on a solid surface under BWR operating conditions. In *Proceedings of the 16th International Topical Meeting on Nuclear Reactor Thermal Hydraulics*, volume 7, pages 5962–5975.
- H. Anglart, M. Bergagio, S. Hedberg, S. Rydström, and W. Frid. 2015. Measurement of wall temperature fluctuations during thermal mixing of non-isothermal water streams. In *Proceedings of the 16th International Topical Meeting on Nuclear Reactor Thermal Hydraulics*, volume 1, pages 807–818.

Both conference papers are peer-reviewed.

Acknowledgments

I would like to thank my colleagues for creating a nice working environment and providing thoughtful feedback. Among them, I am most grateful to Prof. Henryk Anglart for his valuable guidance and support during this project. Special thanks to Wenyuan Fan and Drs. Haipeng Li and Roman Thiele for insightful advice and discussions.

I extend my gratitude to Stellan Hedberg and Stefan Rydström for their help in the lab.

The LES in Subsection 3.6.1 and FEA simulations in Subsection 3.6.7 were performed on resources provided by the Swedish National Infrastructure for Computing (SNIC) at PDC Center for High Performance Computing, KTH. Jing Gong at PDC is acknowledged for assistance concerning technical aspects in making the FEA code run on the Tegner supercomputer.

I would like to thank Profs. Bo Alfredsson, Waclaw Gudowski, Pär Olsson, and Janne Wallenius, along with Assoc. Profs. Jan Dufek, Pavel Kudinov, and Weimin Ma, for submitting SNIC proposals on my behalf and/or for adding me to SNIC projects.

I acknowledge the financial support of the Swedish Radiation Safety Authority (SSM), the Swedish Center for Nuclear Technology (SKC), and Beräkningsgruppen (a panel of representatives from Forsmarks Kraftgrupp AB, Oskarshamns Kraftgrupp AB, Ringhals AB, and Teollisuuden Voima Oyj).

Contents

Contents	xi
List of Figures	xiii
List of Tables	xv
List of Symbols	xvii
1 Introduction	1
2 Background	3
2.1 Thermal mixing and thermal fatigue	3
2.1.1 Thermal mixing	3
2.1.2 Thermal fatigue	5
2.1.3 Correlation between thermal mixing and thermal fatigue	7
2.1.4 Experiments of thermal mixing	9
2.1.5 Estimators of thermal mixing	9
2.1.6 CFD simulations of thermal mixing	11
2.1.7 CFD-FEA coupling for fatigue assessment	13
2.2 Uncertainty	14
2.3 IHCP	15
3 Methods	17
3.1 Experimental setup	17
3.1.1 Overview of the facility	17
3.1.2 Test-section thermocouples	18
3.1.3 Boundary conditions	21
3.2 Data acquisition	25
3.2.1 Data acquisition tasks	25
3.2.2 Inner-tube movement pattern	27
3.3 Postprocessing	28
3.3.1 Inverse- and low-pass filtering	29
3.3.2 Empirical mode decomposition	29

3.3.3	Windowing, DFT, HHT, and Hilbert-Huang marginal spectrum	31
3.4	Mixing intensity	33
3.5	Uncertainty analysis	35
3.6	LES, FEA, and fatigue assessment	36
3.6.1	Governing equations	37
3.6.2	SGS model	38
3.6.3	Numerical methods	39
3.6.4	Properties	39
3.6.5	Space domain and mesh	40
3.6.6	Boundary and initial conditions	44
3.6.7	Linear elastic analysis and fatigue damage assessment	45
3.7	IHCP	46
4	Results	51
4.1	Inverse- and low-pass filtering	51
4.2	Mixing intensity	53
4.3	Frequency analysis	61
4.4	Uncertainty analysis	69
4.5	LES, FEA, and fatigue assessment	71
4.6	IHCP	84
4.6.1	Test Problem 1	84
4.6.2	Test Problem 2	87
5	Conclusions and outlook for future work	95
5.1	Conclusions	95
5.2	Outlook for future work	97
	Bibliography	99

List of Figures

2.1	Example of level-2 mixing (Kickhofel <i>et al.</i> (2016)).	4
2.2	Damaged control rod (Tinoco <i>et al.</i> (2010)).	6
2.3	Temperature in structures made of 316LN stainless steel.	8
3.1	Major components of the HWAT loop.	19
3.2	A picture of the test section.	20
3.3	A picture of the motor shaft.	20
3.4	A picture of a thermocouple disc.	20
3.5	Cylindrical coordinate system fixed to the test section.	21
3.6	Sectional view of the test section.	22
3.7	Exploded drawing of the inner tube.	23
3.8	Sketch of the left and right thermocouple discs.	24
3.9	Longitudinal section of an inner-tube thermocouple.	24
3.10	Inner-tube movement pattern for Case 9	28
3.11	Representative temperature time series $T(t)$ and its spectra.	34
3.12	Time-averaged y^+ , at $0.60 \text{ m} \leq z \leq 0.73 \text{ m}$. Inner surface.	41
3.13	Meshed regions. LES.	42
3.14	Optimal LES mesh.	43
3.15	IHCP domains.	46
4.1	Inner-surface temperatures in Case 1 at $(45^\circ, 0.65 \text{ m})$	52
4.2	Inner-surface temperatures at 0.65 m in Case 1, from thermocouple $H2$	54
4.3	Inner-surface temperatures at 360° in Case 1, from thermocouple $H2$	55
4.4	Axial distribution of the highest, mean, and lowest values of the normalized inner-surface temperatures $T_{f,d}^*$ in Cases 1, 2, 5, and 9.	57
4.5	Mixing estimator in Case 1.	58
4.6	Mixing estimator in Case 5.	58
4.7	Mixing estimator in Case 2.	59
4.8	Mixing estimator in Case 9.	59
4.9	Low-pass filtered and detrended inner-surface temperatures in Case 1 at 45° . Data from thermocouple $H1$	63

4.10	Low-pass filtered and detrended inner-surface temperatures in Case 1 at 225°	64
4.11	Low-pass filtered and detrended inner-surface temperatures in Case 2 at 315°	65
4.12	DFTs in Case 1 at 45°. Data from thermocouple $H1$	65
4.13	Hilbert-Huang marginal spectrum in Case 1, at (45°, 0.65 m). Data from thermocouple $H1$	66
4.14	Hilbert-Huang marginal spectrum in Case 1, at (45°, 0.65 m). Data from thermocouple $V1$	66
4.15	DFTs in Case 1 at 225°.	67
4.16	Hilbert-Huang marginal spectrum in Case 1, at (225°, 0.67 m).	67
4.17	DFTs in Case 2 at 315°.	68
4.18	Hilbert-Huang marginal spectrum in Case 2, at (315°, 0.68 m).	68
4.19	Peaks in the Hilbert-Huang marginal spectra of the inner-surface temperatures with the highest mixing estimator.	70
4.20	Locations at which LES temperatures are sampled.	72
4.21	LES temperature at eight times. Water region. $z = 0.67$ m.	73
4.22	LES velocity magnitude at eight times. $z = 0.67$ m.	74
4.23	Time-averaged Q isocontours colored by time-averaged temperature.	76
4.24	LES temperatures at WB, on the inner surface, and at TB.	77
4.25	LES and experimental inner-surface temperatures, at four angles and $z = 0.67$ m.	77
4.26	Axial distribution of the highest, mean, and lowest values of the normalized LES inner-surface temperatures $T_{f,d}^*$	78
4.27	Mixing estimator. LES.	79
4.28	Stresses at 0.993 R_{io}	80
4.29	Inner-surface CUF.	81
4.30	ℓ^2 -norm of the difference between old and new CUFs.	82
4.31	Hilbert-Huang marginal spectra of LES and experimental inner-surface temperature time series at (45°, 0.67 m).	82
4.32	Peaks in the Hilbert-Huang marginal spectra of 20 LES inner-surface temperatures from fatigue-prone areas.	83
4.33	Meshes. Left: for the DHCP. Right: for the IHCP (Cases 1.1 and 1.2).	84
4.34	Temperature distributions. Left of each subfigure: Y . Right of each subfigure: T (Case 1.1), at $k = 11$	85
4.35	T_u (Case 1.1) at $k = 11$	86
4.36	Instantaneous error with respect to iteration number and time. Case 1.1.	88
4.37	Difference between non-dimensional volume-averaged temperatures in Cases 1.1 ($\xi = 1.0$) and 1.2 ($\xi = 0.1$). $k = 11$ in both cases.	89
4.38	Temperature distributions. Left of each subfigure: Y . Right of each subfigure: T (Case 2.1), at $k = 3$	92
4.39	Left: Y_u . Right: T_u (Case 2.1) at $k = 3$	93
4.40	Time-integrated errors in Cases 2.1 (fine mesh), 2.2 (medium mesh), and 2.3 (coarse mesh).	94

List of Tables

2.1	T-junction experiments on mixing of water streams at different temperatures.	10
3.1	Key parameters in the test section of the HWAT loop and in BWRs. . .	18
3.2	Locations of the inner-tube thermocouple tips.	23
3.3	Experimental matrix listing boundary conditions and T_{mix}^* when test-section temperatures are sampled at 1000 Hz.	25
3.4	Experimental matrix listing boundary conditions and T_{mix}^* when test-section temperatures are sampled at 100 Hz.	25
3.5	Overview of relevant data acquisition parameters.	27
3.6	Key mesh quality parameters.	41
3.7	LES inlet boundary conditions.	44
4.1	Highest gains G and lowest, highest, and mean differential spreads Δ at a sampling rate of 1000 Hz.	55
4.2	Maximum mixing estimator in each experimental case.	60
4.3	Elements in arrays \tilde{B}^+ , \tilde{B}^- , and \tilde{S} with a sampling rate of 1000 Hz. . .	69
4.4	Elements in arrays \tilde{B}^+ , \tilde{B}^- , and \tilde{S} with a sampling rate of 100 Hz. . .	71
4.5	Key parameters in the cases considered. Test Problem 2.	89

List of Symbols

Symbol	Description	Acronyms	Units
CGM	conjugate gradient method		-
CHT	conjugate heat transfer		-
CRGT	control-rod guide tube		-
CUF	cumulative usage factor		-
DES	detached eddy simulation		-
DFT	discrete Fourier transform		-
DHCP	direct (forward) heat conduction problem		-
EMD	empirical mode decomposition		-
FIR	finite impulse response		-
HCTF	high-cycle thermal fatigue		-
HHT	Hilbert-Huang transform		-
IHCP	inverse heat conduction problem		-
IHTP	inverse heat transfer problem		-
IMF	intrinsic mode function		-
LES	large eddy simulation		-
NC	number of channels		-
OI	orthogonality index		-
PISO	pressure-implicit split-operator		-
RANS	Reynolds-averaged Navier-Stokes		-
SGS	subgrid scale		-
SIMPLE	semi-implicit method for pressure-linked equations		-
TB	location in the inner tube, at $\delta = 0.035$ mm from the inner surface		-
URANS	unsteady RANS		-
WALE	wall-adapting local eddy viscosity		-
WB	location in the water region, at $\delta = 0.035$ mm from the inner surface		-

Greek Symbols		
Symbol	Description	Units
α	thermal diffusivity times density	$\text{kg m}^{-1} \text{s}^{-1}$
$\hat{\alpha}$	optimal step size	-
β	conjugation coefficient	-
γ	regularization parameter	$\text{K}^2 \text{m}^4 \text{W}^{-2}$
Γ	boundary	m
Γ_j	boundary where q_j is prescribed	m
δ	distance from the wall	m
Δ	LES filter width	m
Δq_u	direction in which q_u is perturbed	W m^{-2}
Δt	time step	s
ΔT	absolute temperature difference between cold and hot inlets	K
ε	instantaneous error	-
$\boldsymbol{\varepsilon}$	strain tensor	-
ζ	dimensionless axial coordinate	-
η	time-integrated error	-
θ	angle	$^\circ$
$\hat{\theta}$	solution to the sensitivity problem	K
$\Theta_Q[l; m]$	m -th position of Q in terms of θ for case l	$^\circ$
λ	thermal conductivity	$\text{W m}^{-1} \text{K}^{-1}$
μ	dynamic viscosity	Pa s
$\hat{\mu}$	mean of the normal distribution	K
ξ	standard deviation of the Gaussian noise	-
ρ	density	kg m^{-3}
σ	standard deviation	K
$\hat{\sigma}$	standard deviation of the normal distribution	K
$\bar{\sigma}$	mixing estimator	-
$\boldsymbol{\sigma}$	Cauchy stress tensor	Pa
$\boldsymbol{\tau}$	shear-rate tensor	Pa
ϕ	solution to the dual problem	$\text{m}^2 \text{K}^2 \text{W}^{-1}$
ω	instantaneous frequency	Hz
Ω	spatial domain	m^2

Roman Symbols		
Symbol	Description	Units
A	length of each $T_{f, DAS}$ after being low-pass filtered	$\text{S it}^{-1} \text{ch}^{-1}$

Continued on next page

Continued from previous page

Roman Symbols		
Symbol	Description	Units
B^-	negative-side systematic uncertainty	K
B^+	positive-side systematic uncertainty	K
c	specific heat capacity	$\text{J kg}^{-1} \text{K}^{-1}$
c_0	index of the first mode in the trend	-
c_p	specific heat capacity at constant pressure	$\text{J kg}^{-1} \text{K}^{-1}$
ch	channel	-
Co	Courant number	-
D	cumulative usage factor, or CUF	-
D_p	inner diameter of the inlet pipes	m
f	frequency	Hz
f_S	sampling rate	Hz
g	IMF	-
\mathbf{g}	gravitational acceleration	m s^{-2}
G	number of IMFs extracted from a time series	-
h	enthalpy	J kg^{-1}
\hat{h}	convective heat transfer coefficient	$\text{W m}^{-2} \text{K}^{-1}$
it	iteration of a given task	-
\mathcal{J}	objective function	m s K^2
k	iteration number	-
l	case identifier	-
L_p	distance between inlet and sampling plane	m
m	progressive entry number in the movement pattern for case l	-
\dot{m}	mass flow rate	kg s^{-1}
m^*	number of entries in the movement pattern for case l	-
m_u	progressive entry number in the deduplicated movement pattern for case l	-
n^*	number of temperature arrays at a certain position for case l	-
\mathbf{n}	outward-pointing unit normal vector	-
NS_j	number of samples per iteration j per channel	$\text{S it}^{-1} \text{ch}^{-1}$
p	pressure	Pa
\hat{p}	conjugate search direction	W m^{-2}
Pe	Péclet number	-
Pr	Prandtl number	-
\mathbf{q}	heat flux	W m^{-2}

Continued on next page

Continued from previous page

Roman Symbols		
Symbol	Description	Units
q_j	scalar normal heat flux	W m^{-2}
\hat{Q}	center of the circular base of the mid thermocouple disc	-
(r, θ, z)	cylindrical coordinate system attached to the inner tube	$(\text{m}, ^\circ, \text{m})$
R_1	region defined as $R_1 = \{(\theta, z) : 135^\circ \leq \theta \leq 225^\circ\}$	-
R_2	region defined as $R_2 = \{(\theta, z) : (315^\circ \leq \theta \leq 360^\circ) \cup (0^\circ < \theta \leq 45^\circ)\}$	-
R_{io}	outer radius of the inner tube	m
R_{oi}	inner radius of the outer tube	m
Re	Reynolds number	-
\mathbf{s}	displacement at the current time	m
\mathbf{s}^0	displacement at the last time	m
\mathbf{s}^{00}	displacement at the time previous to the last	m
S	samples	-
S	random uncertainty	K
\mathbf{S}	rate-of-strain tensor	s^{-1}
t	time	s
t_f	final integration time	s
t_{\max}	end time	s
T	temperature; in sections on the IHCP, solution to the primal problem	K
$T_{f,d}$	inner-surface temperature	K
T^*	normalized temperature	-
\mathcal{T}	time domain $[0, t_{\max}]$	s
\mathbf{u}	instantaneous velocity	m s^{-1}
V	cell volume	m^3
(x, y, z)	Cartesian coordinate system attached to the inner tube	$(\text{m}, \text{m}, \text{m})$
\mathbf{x}	spatial coordinate	m
y^+	dimensionless distance from the wall	-
Y	noise-free solution to the DHCP	K
\tilde{Y}	initial noise-free temperature	K
Y_∞	temperature of the medium	K
$Z_Q[l; m]$	m -th position of Q in terms of z for case l	m

Subscripts		
Symbol	Description	Units
<i>b</i>	branch pipe	-
<i>bc</i>	before calibration	-
<i>C</i>	cold inlets	-
<i>DAS</i>	acquisition of temperatures from the test section	-
<i>eff</i>	effective	-
<i>f</i>	any of thermocouples <i>H1</i> , <i>H2</i> , <i>H3</i> , <i>H4</i> , <i>V1</i> , and <i>V4</i>	-
<i>g</i>	related to the known heat flux	-
<i>H</i>	hot inlets	-
<i>if</i>	inverse-filtered	-
<i>lf</i>	low-pass filtered	-
<i>m</i>	main pipe	-
<i>S</i>	solid	-
<i>u</i>	related to the unknown heat flux	-
<i>w</i>	windowed	-

Superscripts		
Symbol	Description	Units
<i>I</i>	lower sampling rate	-

Operators		
Symbol	Description	Units
$\bar{\cdot}$	low-pass filtered, unless otherwise specified	-
$\tilde{\cdot}$	Favre-filtered, unless otherwise specified	-

Chapter 1

Introduction

This thesis presents an experimental and analytical investigation of the turbulent mixing of cold and hot streams in a vertical annular volume between an inner and an outer tube. Experimental and computational temperature time series from the inner surface of this annulus are mainly analyzed here.

High-quality measurements with low uncertainty are necessary to validate codes coupling computational fluid dynamics (CFD) with finite element analysis (FEA) to predict thermal fatigue cracking due to turbulent mixing. This topic is worthy to be studied because thermal fatigue threatens the safe and affordable operation of nuclear power and process plants. Specifically, it is challenging to monitor high-cycle thermal fatigue using existing plant instrumentation and to predict it using standard models, because the current understanding of turbulent mixing, heat transfer between fluid and adjoining walls, stress changes due to cyclic thermal loads, and fatigue life under such stress cycles is lacking.

The experiments on turbulent thermal mixing discussed here were conducted in 2014 and 2015 in the HWAT (High-pressure Water Test) loop at KTH, Stockholm, Sweden, under conditions corresponding to those in Oskarshamn 3 and Forsmark 3. In 2008, several control-rod stems in these twin reactors were found to be damaged by thermal fatigue due to turbulent mixing in the annuli formed by stems and control-rod guide tubes. In the HWAT loop, pressure alongside hot and cold inlet temperatures matched reactor conditions; namely, they were set to 7.2 MPa, 333 K, and 549 K, respectively. Hence, hot and cold water streams differed by 227 kg m^{-3} in density and by 2.1 in Prandtl number. These remarkable changes in water properties cannot be disregarded when experimental data are analyzed and simulations of turbulent mixing under reactor conditions are performed.

These simulations provide a large amount of detailed data, which, among other purposes, can be used to verify methods for solving inverse heat transfer problems.

This thesis is structured into three chapters. Chapter 2 outlines thermal mixing, thermal fatigue, and the connection between them. Topics such as uncertainty evaluation for the above temperature measurements, CFD simulations of turbulent

thermal mixing, coupling of CFD and FEA for thermal fatigue assessment, and reconstruction of the inner-tube temperature field from over-specified boundary data are also introduced.

Chapter 3 describes test facility, inner-tube thermocouples, and data acquisition system (DAS); post-processing of the inner-surface temperatures, including filtering and spectral analysis; mixing inhomogeneity assessment through a simple scalar estimator; and uncertainty sources. Chapter 3 also explains the CFD-FEA coupling approach adopted here, which comprises a large eddy simulation (LES) of turbulent thermal mixing in the above annulus; an FEA of the inner tube under LES thermal and pressure loads; and a fatigue damage assessment method based on the FEA stress history. Moreover, Chapter 3 presents an iterative algorithm for solving transient inverse heat conduction problems (IHCPs) on two-dimensional domains.

Chapter 4 describes some of the LES and experimental inner-surface temperatures; LES velocities and vortices in areas of interest; mean inner-surface temperatures in the measurement region, along with their ranges and the mixing estimator there; FEA stresses on the inner surface; cumulative fatigue usage factors (CUFs); power spectra of experimental inner-surface temperatures at locations with high mixing inhomogeneity, together with their dominant frequencies; power spectra of LES inner-surface temperatures at fatigue-susceptible locations, along with their dominant frequencies; an uncertainty estimate for inner-surface temperature data; and solutions to two test IHCPs, with a verification of the solving algorithm.

Chapter 2

Background

2.1 Thermal mixing and thermal fatigue

2.1.1 Thermal mixing

Mixing of flows at distinct temperatures – see Fig. 2.1 – can apply cyclic thermal loads to the walls, which can then trigger fatigue damage.

The non-isothermal mixing (thermal mixing) under study can be classified as turbulent, of level 2 (Dimotakis (2005)), based on LES results in Figs. 4.21, 4.22 and 4.23: here, mixing involves water streams at different densities (usually between 803 kg m^{-3} and 986 kg m^{-3}) and velocities (whose axial components usually vary between -1.4 m s^{-1} and 0.4 m s^{-1}) in a gravitational field, so it alters the flow dynamics.

Turbulent mixing is a multi-scale phenomenon involving three stages: (1) entrainment or injection, which happens at large scales; (2) stirring or dispersion, which occurs at intermediate scales; (3) and diffusion, which is driven by small-scale dynamics (Eckart (1948)). For liquids, the Schmidt number is high (i.e., kinematic viscosity exceeds mass diffusivity), so diffusion comprises two steps: in Step 1, kinematic viscosity acts on small-scale vorticity, which is mainly driven by straining at larger scales, whereas in Step 2 mass or heat diffusion happens, if mass fractions or temperature gradients can be specified.

Three levels are distinguished in mixing: 1, 2, and 3. In level-1 mixing, or passive mixing, the distribution of a scalar descriptor of the mixing process depends on molecular diffusion and fluid advection, but it does not alter the flow dynamics. Temperature can be regarded as a passive scalar in incompressible flows (Sakowitz (2013)) if temperature gradients are small.

Contrarily, level-2 mixing alters the flow dynamics. Misaligned density and pressure gradients add a baroclinic contribution $\nabla\rho\times\nabla p$ to the vorticity equation, which increases instability. Instability in turn creates more isopycnic (constant-density) or isobaric (constant-pressure) surfaces; that is, it reduces density or pressure gradients, which in turn change the generation of baroclinic vorticity (Dimotakis (2005)).

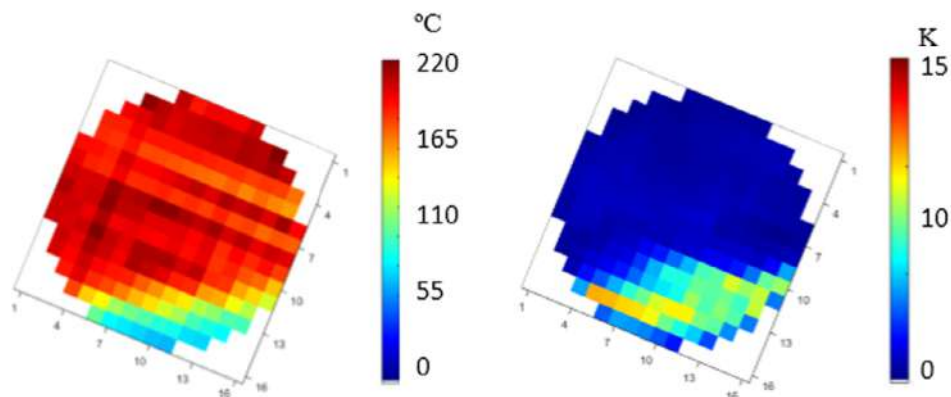


Figure 2.1: Mean (left) and RMS (right) temperatures at 3.5 main-pipe diameters downstream of a mixing tee where level-2 mixing occurs (Kickhofel *et al.* (2016)). Data from the mesh sensor module there. Main-pipe and branch-pipe temperatures equal 529 K and 297 K, respectively. Pressure reaches 7 MPa.

Rayleigh-Taylor and Richtmyer-Meshkov instabilities epitomize level-2 mixing.

Level-3 mixing changes fluid-intensive properties, including density and composition. Here, the coupling between mixing and flow dynamics is strong. Combustion exemplifies level-3 mixing.

Together, level-2 and level-3 mixing are called “active mixing”. Level-2 and level-3 mixing are not well understood yet, to the extent that they can be considered open research areas. This is mainly because, here, turbulence is anisotropic at some scales. Anisotropy arises from the asymmetry originated by large-scale features, such as acceleration/gravitational fields. Consequently, the classical Kolmogorov-Obukhov-Corrsin (KOC) theory, which assumes local isotropy (i.e., at small scales) at sufficiently high Re , cannot be readily applied (Movahed and Johnsen (2015)). Moreover, concerning flows at high Re , researchers have mainly analyzed canonical flows (for example, flow in jets, pipes, and free shear layers) and obtained their results from empirical data (Dimotakis (2005)).

In industrial applications (e.g., stirred vessels and multifunctional heat exchanger-reactors), three other levels are identified: macromixing, mesomixing, and micromixing. Macromixing is related to the macroscale circulation time and to the volume of the mixer; thus, it occurs at large scales. Mesomixing is driven by turbulent diffusion and occurs at transitional scales. Micromixing is driven by kinematic viscosity and molecular diffusion. It occurs at small scales (Torbacke and Rasmuson (2004)) and is typically much faster than macromixing (Bird *et al.* (2007)).

2.1.2 Thermal fatigue

Before uniformity, homogeneity, and good mixedness are obtained, mixing non-isothermal water streams causes cyclic temperature oscillations. These oscillations propagate into the adjoining walls according to their frequency content and result in cyclic thermal stresses. These stresses, even if below the yield stress, could cause thermal fatigue, a damage accumulation process: first, short cracks appear on the wall surface; then, deep cracks might originate and either arrest at certain depths or propagate through the wall under specific conditions (Paffumi *et al.* (2015)). As stress gradients are large, cracks caused by thermal fatigue are usually long defects (“elephant skin”) of high aspect ratio (Gosselin *et al.* (2007)). Thermal loads, geometry, and material properties appear to drive the crack growth.

Thermal fatigue is one of the main safety-related issues affecting aging management and life extension of current reactors (Walker *et al.* (2009)), as well as the design of new reactors.

The probability of thermal fatigue does not increase continuously with time, as several failures ascribable to this damage mechanism, which happened in less than a year, evidenced (Dahlberg *et al.* (2007)). Thermal fatigue usually corresponds to biaxial strains and stresses (Dahlberg *et al.* (2007)) and appears more dangerous than uniaxial isothermal fatigue (Fissolo *et al.* (2009)). Two regimes can be identified: low-cycle (LCTF) and high-cycle thermal fatigue (HCTF). HCTF may occur above $10^4 - 10^5$ stress cycles to failure. HCTF assessment methods are usually too conservative or not sufficiently conservative because of the following reasons: (1) unlike LCTF, HCTF may not be monitored or detected by typical plant instrumentation systems, including thermocouples installed on the outer surface of the components under inspection, owing to delays in response and to the low-pass filtering effect of the wall (Bergholz and Bruckmueller (2012)). (2) HCTF assessment methods may not cover all material responses and loading conditions (Metzner and Wilke (2005)). (3) Lack of proper data on HCTF inhibits a better understanding of crack initiation and growth.

To date, thermal fatigue incidents have occurred in light-water reactors (LWRs), including Farley 2 in 1987, Tihange 1 in 1988, Loviisa 2 in 1994 and 1997, Civaux 1 in 1998, Tsuruga 2 in 1999, and Tomari 2 in 2003 (Farley (1987); Hytönen (1998); Shah *et al.* (1999); Faidy *et al.* (2000); Sugano *et al.* (2000)); sodium-cooled fast reactors (e.g., PHENIX in 1991); refineries; petrochemical and liquefied natural gas facilities (Maegawa (2006); Qian *et al.* (2015)), particularly close to T-junctions. Between 2013 and 2015 fatigue damaged some US PWRs and BWRs. Most events were due to thermal fatigue (McDevitt *et al.* (2015)).

The present study moves from thermal fatigue failures in the twin boiling water reactors (BWRs) Oskarshamn 3 and Forsmark 3 in 2008. There, many control-rod stems were detected to be either broken or cracked, mostly in zones of high stress concentration such as holes, welds, and abrupt shape changes – see Fig. 2.2.

Some projects on thermal fatigue assessment are listed here:

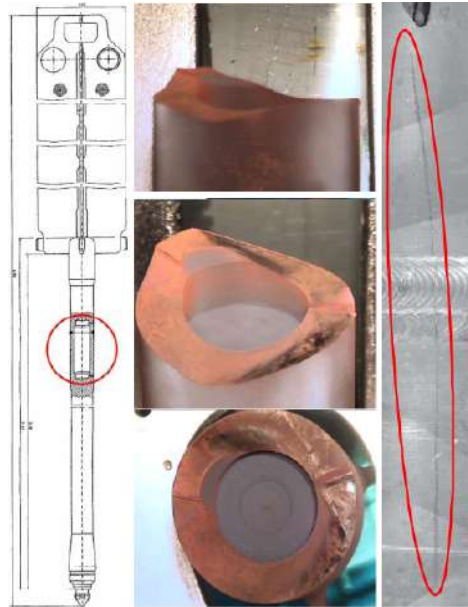


Figure 2.2: Left: control rod with a welded joint between sheets and stem (red circle). Middle: views of a fracture which is level with a so-called gas hole. This hole is filled by welding. Right: axial crack on the stem (red ellipse). From Tinoco *et al.* (2010).

- The “Materials Reliability Project” (MRP), sponsored by the Electric Power Research Institute (EPRI) to define guidelines for evaluating, attenuating, and monitoring thermal fatigue (Keller *et al.* (2004)).
- The “THERmal FATigue evaluation of piping system tee-connections” (THER-FAT), financed by the European Commission (EC). Among other goals, it sought to identify parameters causing fatigue in T-junctions, assess current safety margins against fatigue failure, define screening criteria for fatigue analysis, and devise methodologies for preventing thermal fatigue (Metzner and Wilke (2005)).
- The Thermal Fatigue Project (NESC-TF), set up by the Network for Evaluation of Structural Components (NESC) to develop a common methodology for preventing HCTF. NESC-TF focused on turbulent mixing in T-junctions of LWR piping systems (Dahlberg *et al.* (2007)).
- The “Thermal Fatigue - Basics of the system-, outflow- and material-characteristics of piping under thermal fatigue”, funded by the German Federal Ministry of Education and Research (BMBF) to create and validate mate-

rial models of crack initiation and growth under cyclic thermal loads (Work Package 2; see Schuler *et al.* (2012)).

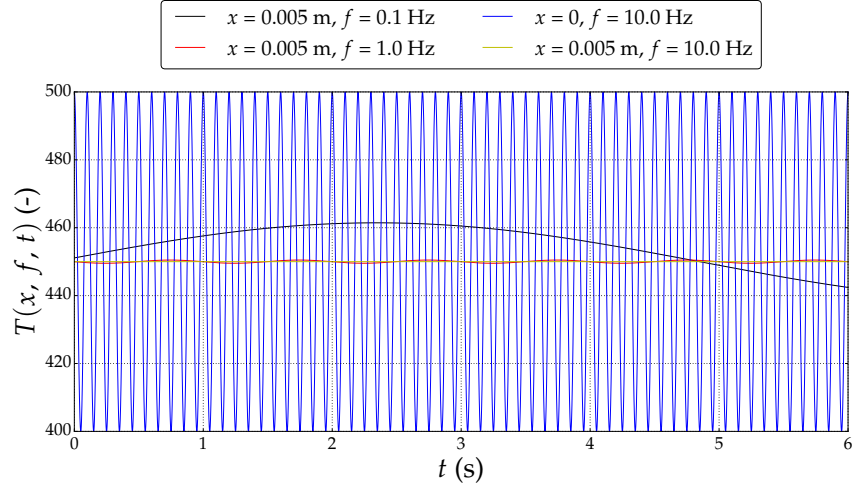
Moreover, guidelines – e.g., that issued by JSME (JSME (2003)) –, codes – e.g., the ASME Code Section III for design (ASME (2015b)) and the French RCC-M and RCC-MR codes –, and standards – e.g., the German safety standard KTA – allow to assess thermal fatigue. However, no full international consensus has yet emerged on thermal fatigue assessment.

2.1.3 Correlation between thermal mixing and thermal fatigue

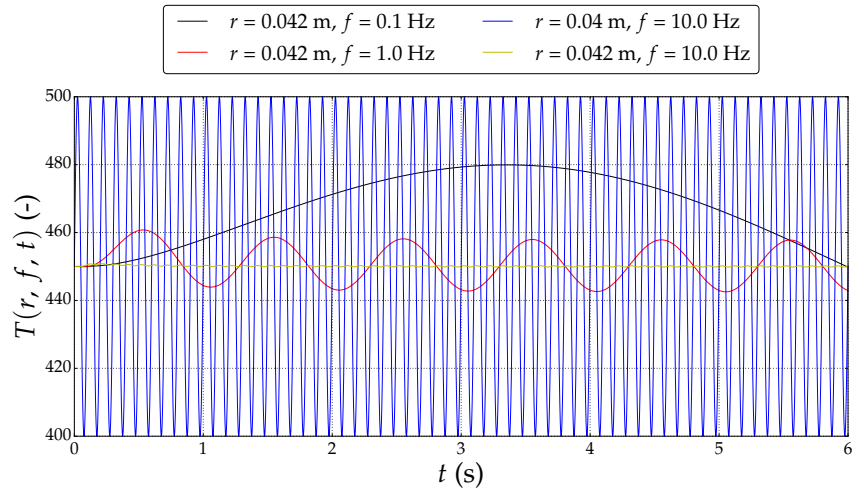
Subsection 2.1.2 suggests that thermal fatigue is an interdisciplinary subject, involving thermal-hydraulics; heat transfer; mechanics; and materials science. Understanding thermal-hydraulics is crucial to adequately assess load types: turbulent mixing; thermal stratification; turbulent penetration and thermal cycling; and thermal striping. Knowledge of heat transfer is essential to model the heat flux between fluid and wall. A good grasp of mechanics is necessary to predict stresses induced by thermal loading. Advances in materials science could help to investigate the resistance of the wall material to cracking (Chapuliot *et al.* (2005)), crack initiation and propagation, along with sequence effects; i.e., whether the damage induced by high-amplitude load cycles (that is, low-cycle fatigue) followed by low-amplitude load cycles (that is, high-cycle fatigue) is more significant than the opposite (Taheri *et al.* (2013)).

Only the first topic – i.e., thermal-hydraulics – is commented upon in this subsection. Concerning temperatures in the neighboring walls, the amplitude of quasi-steady temperature in a half-infinite wall changes over the space coordinate x as $\Delta T_{wall} \exp\left(-x\sqrt{\pi f/\alpha}\right)$ (Taler and Duda (2006)). Here, ΔT_{wall} indicates the amplitude of temperature fluctuations at the wall surface ($x = 0$ and $t = 0$); f denotes the frequency of these fluctuations; and α represents the thermal diffusivity of the wall material. The above formula holds if (1) the temperature at the wall surface equals $\Delta T_{wall} \cos(2\pi ft)$ (i.e., it is cosinusoidal over time t); and (2) the wall temperature at $x \rightarrow \infty$ and that at $t = 0$ equal the mean temperature at $x = 0$. Consequently, if stainless steel diffusivity $\alpha \approx 4 \times 10^{-6} \text{ m}^2 \text{ s}^{-1}$ and f is 0.1 Hz, the amplitude of temperature fluctuations at 5 mm off the wall surface is roughly one quarter of that at the surface. If f is 10 Hz, this amplitude is less than 10^{-6} times that at the surface. Thus, high frequencies only contribute to the wall temperature in the immediate vicinity of the wall surface (see Fig. 2.3).

Correspondingly, thermal fatigue cracks are ostensibly initiated by surface temperatures oscillating from 0.01 Hz (Tinoco *et al.* (2009)) to 0.5 Hz (Angele *et al.* (2011)) in annuli, and from 0.1 Hz (Chapuliot *et al.* (2005)) to 3-5 Hz (Ayhan and Sökmen (2012)) in T-junctions. These values were encountered in areas where turbulent mixing of streams at distinct temperatures occurred. In detail, Kasahara *et al.* (2002) modeled fatigue damage in a half-infinite wall when the temperature of the fluid near the wall surface changes sinusoidally with time, at frequency f . The



(a) At 5 mm off the surface of a half-infinite wall. Temperature at $x \rightarrow \infty$ is set to T_0 . The inner-surface temperature is expressed as $\Delta T_{wall} \cos(2\pi ft)$. Equations from Taler and Duda (2006).



(b) At 2 mm off the inner surface of a hollow cylinder. The outer-surface temperature is set to T_0 . The inner-surface temperature is expressed as $\Delta T_{wall} \sin(2\pi ft)$. Inner and outer surfaces at $r = 0.04$ m and at $r = 0.05$ m, respectively. Equations from Radu *et al.* (2008).

Figure 2.3: Temperature time series in structures made of 316LN stainless steel. Thermal diffusivity at $T_0 = 450$ K. The initial temperature is T_0 everywhere. $\Delta T_{wall} = 50$ K.

introduction of a heat transfer coefficient allowed to express the frequency response function, evaluating wall stress ranges induced by varying fluid temperatures, as the product of an effective thermal stress function, computing the above wall stresses caused by surface temperatures, and of an effective heat transfer function, reducing temperature from fluid to surface. With increasing f , less thermal homogenization increases the gain of the effective thermal stress function, whereas heat transfer loss reduces the gain of the effective heat transfer function. Consequently, the highest stress ranges, which may result in fatigue damage, are induced at intermediate frequencies f , from 0.1 to 10 Hz.

Sinusoidal methods provide overconservative predictions of fatigue lifetime (Hanink and Blom (2011)), so conducting an appropriate spectral analysis of surface temperatures can clearly help to predict and prevent thermal fatigue cracking. Given the complexity of thermal loads due to turbulent mixing, CFD-FEA simulations on 3D domains ought to be performed (Dahlberg *et al.* (2007)).

2.1.4 Experiments of thermal mixing

The lack of accurate methods for predicting HCTF caused by mixing of non-isothermal streams justifies the many studies attempting to devise these methods. To date, this kind of mixing has been investigated through computations (see Subsection 2.1.6) and experiments. Some of the latter, performed in T-junctions, are listed in Table 2.1. This table highlights that, to date, only a few experiments on mixing of streams with a temperature difference of more than 100 K have been performed. Furthermore, the T-junction geometry does not correspond to that between the control-rod guide tube (CRGT) and stem under inspection, which is essentially annular. This issue was addressed by performing experiments in two test sections reproducing the annulus around a stem (Angele *et al.* (2011)): the first test section was a plexiglass structure, which limited ΔT (i.e., the temperature difference between hot and cold inlets) to 30 K at ambient pressure; the second test section was a steel structure, so ΔT could reach 80 K. 0.13-mm \varnothing thermocouples sampled water temperatures at 50 Hz. They were located 1 mm off the surfaces of the inner and outer tubes – i.e., in the water region –, at several azimuthal and axial coordinates. Nevertheless, these experiments were performed at low pressures and temperatures, far from BWR conditions. The need for more experimental studies on mixing of water streams under BWR conditions led to the current research.

2.1.5 Estimators of thermal mixing

When thermal mixing is to be described in terms of non-uniformity, intensity, and efficiency, deriving appropriate indicators from vast data sets, be they computational or experimental, and creating algorithms to correctly analyze such data appear to be daunting tasks. For example, in Angele *et al.* (2011), these data came from experiments, scale-adaptive simulations (SAS), and unsteady Reynolds-averaged Navier-Stokes (URANS) of water streams at different temperatures mixing

Table 2.1: Experiments on mixing of water streams at different temperatures in T-junctions. Only sensors sampling water temperature are listed here.

Source (test facility)	T_m (K)	T_b (K)	$ \mathbf{u}_m $ (m s^{-1})	$ \mathbf{u}_b $ (m s^{-1})	p (MPa)	Sensors	f_S (Hz)	y^* ¹ (-)
Fukushima <i>et al.</i> (2003)	296.98,	296.93,	0.02,	0.04,	~ 0.1	0.5-mm \varnothing , ungrounded thermocouples	50	0,
	...,	...,	0.15	0.3				...
	343.63	343.36						0.5
Kawamura <i>et al.</i> (2003), Hu and Kazimi (2006) (Hitachi and Toshiba tests)	290.85,	324.95,	0.27,	0.21,	~ 0.1	Thermocouples	25	0.03
	...,	...,	...,	...,				
	297.95	329.65	2.54	2.52				
Westin <i>et al.</i> (2006) (Vattenfall)	297.15,	332.95,	1.69,		~ 0.1	Thermocouples	90	$1/190$
	...,	...,	...,	1.68				
	300.45	339.05	3.97					
Kamide <i>et al.</i> (2009) (WATLON)			0.11,	0.5,	~ 0.1	0.25-mm \varnothing thermocouples	100	$1/150$,
	321	306	...,	...,				...
			2.9	1.5				0.5
Braillard and Edelin (2009), Kuhn <i>et al.</i> (2010) (FATHERINO)					~ 0.1	0.5-mm \varnothing K-type thermocouples	5	$2/54, 5/54$
	356	281	2.55	0.85				
Naik-Nimbalkar <i>et al.</i> (2010)	303	318	0.33,	0.5,	~ 0.1	Constant-current, hot-wire anemometer	1000	0.1,
			...,	...,				...
			1	1.32				0.5 ²
Kuschewski <i>et al.</i> (2013) (FSI)	415,		0.11,		3	1-mm \varnothing K-type thermocouples	100	$2/71.8$
	421	298	0.16	0.08				
Chen <i>et al.</i> (2014) (EXTREME)	363	293	0.05,	0.96,	0.49	Thermocouples	NA	0.112,
			...,	...,				...
			0.2	3.37				0.5
Kickhofel <i>et al.</i> (2016) (FSI)	438,	295,	0.11,		7	0.25-mm \varnothing K-type thermocouples and mesh sensor	100 (thermocouples), 10000 (mesh sensor)	$2/71.8$
	...,	...,	...,	0.08				(thermocouples)
	529	297	0.12					(thermocouples)

¹Scalar quantity y^* is ratio of the distance between measurement points and wall, to the hydraulic diameter of the conduit.²For the data analyzed.

in an annulus. Mean and RMS temperatures were computed at several axial and azimuthal coordinates. Power spectral densities (PSD) of SAS and experimental temperatures were calculated to show that the dominant frequencies are lower than 0.5 Hz, a hallmark of thermal fatigue.

In Sakowitz *et al.* (2014), three estimators evaluated the mixing quality in a T-junction, on the basis of the passive scalar modeling the mixing phenomenon: (1) the RMS value of this scalar, accounting for how the passive scalar changes over time; (2) a uniformity index, derived from the difference between the time-averaged scalar and the time-averaged, space-averaged scalar over a cross section of the domain; and (3) the integral time scale of the scalar oscillations, which represents the longest time during which they are correlated.

In El Omari and Le Guer (2010), where heat transfer and thermal mixing in a two-rod mixer were studied, an estimator termed “composite mixing indicator” was computed as the time-averaged ratio of the cell-averaged non-dimensional fluid temperature to its standard deviation; i.e., to its level of homogenization in the mixer. A high composite mixing indicator implies good thermal mixing. An estimator termed “temperature scalar dissipation indicator” was computed to measure the creation and destruction of the temperature gradient.

Other researchers investigated mixing parameters estimating micro- and macromixing; for example, in Koop and Browand (1979), a parameter termed “mixedness” (Konrad (1977)) was introduced to gauge micromixing.

2.1.6 CFD simulations of thermal mixing

Computations comparable to those discussed here have recently been performed by other research teams.

Angele *et al.* (2011) (see Subsection 2.1.4 for the respective experiments) conducted a CFD analysis of thermal mixing in the annulus between CRGT and stem. A URANS approach with the $k-\omega$ SST turbulence model and SAS were considered, as mentioned in Subsection 2.1.5. Experimental and computational results agreed reasonably well; nevertheless, peaks in SAS temperature spectra were larger and sharper than in experiments, so SAS results should be considered with caution if used to assess thermal fatigue under reactor conditions. Angele *et al.* (2011) suggested that their research be enhanced by running detached eddy simulations (DES) and large eddy simulations (LES). In a DES, URANS modeling is applied near the wall, whereas regions far from the wall are treated using LES.

Comparably to Angele *et al.* (2011), Lillberg (2013) conducted an LES of thermal mixing in the annulus between CRGT and stem. The LES was run using the open-source software OpenFOAM. A one-equation eddy viscosity subgrid-scale (SGS) model was adopted to model the smaller scales. Using wall functions would yield incorrect results: most wall functions assume steady, fully developed flow, whereas the boundary layer in the mixing region grows and decays quickly. Conjugate heat transfer (CHT) was added: the temperature equation was also solved in the solid regions and coupled to the water energy equation at the water-solid

interface. Computational and experimental results agreed fairly well in terms of key variables, including temperature amplitudes and frequencies, at a position where RMS temperatures are high.

As a preliminary to the experiments in Section 3.1, Pegonen *et al.* (2014) conducted an LES of thermal mixing at BWR conditions ($\Delta T = 216$ K) in a simplified CRGT. The dynamic Smagorinsky model was adopted. This LES was conducted to determine dominant frequencies and the size of the mixing region. Zero heat flux was assumed at the walls, which were left unmodeled. In the most dangerous region, temperatures at 1 mm from the control-rod stem exhibited dominant frequencies at about 0.1 Hz. When two cold inlets were introduced at 90° and 270° – i.e., at 90° from the two hot inlets –, at a lower level than the hot inlets, the most dominant spectral peaks were found at positions aligned with the hot inlets.

Concerning thermal mixing in T-junctions, Westin *et al.* (2008) compared LES results with experimental data from the Vattenfall test facility ($\Delta T = 15$ K). The wall-resolved adapting local eddy-viscosity (WALE) SGS model (Nicoud and Ducros (1999)) was adopted. Westin *et al.* (2008) focused on how different inlet conditions, mesh resolutions, and turbulence modeling approaches affect LES results. Three velocity boundary conditions were tested at the inlets: (1) mean velocities, or no perturbation; (2) isotropic turbulence read from file; and (3) perturbation from an oscillating vorticity field generated using a 2D vortex method. Westin *et al.* (2008) proved that LES results are only slightly sensitive to the above inlet conditions. They also conducted a DES with boundary condition (2). Both LES and DES produced acceptable mean temperatures at 90° and 270° near the pipe wall downstream of the T-junction (its top is at 0°); however, only the LES produced accurate RMS temperatures there, because of excessive dissipation in the DES model: RMS values from DES are 1.5 to 2 times their experimental counterparts at the same cross sections, 4-10 diameters downstream of the T-junction. Moreover, the coarser mesh could reproduce the large-scale unstable flow in the mixing zone, but the finer mesh provided better results. This is expected because a finer mesh can resolve the relevant turbulence length scales.

Jayaraju *et al.* (2010) validated the WALE model against experimental data from the Vattenfall T-junction and compared this model with a wall-modeled (i.e., wall-function based) approach. The wall-modeled approach underpredicted RMS heat fluxes along the streamwise direction and gradients of time-averaged RMS temperatures and axial velocities near the walls. Hence, a wall-resolved approach ought to be adopted.

Timperi (2014) compared LES results with experimental data from the Vattenfall T-junction. The Smagorinsky SGS model was adopted. Timperi (2014) examined two inlet conditions: no perturbation (steady inlets); and perturbation from an oscillating vorticity field generated using a 2D vortex method (turbulent inlets). For both inlet conditions, good agreement was observed between LES results and experimental data; notwithstanding, comparably to Westin *et al.* (2008), the turbulent inlets slightly worsened the agreement of RMS temperatures at two locations, possibly because of insufficient mesh resolution. CHT was shown to strongly

affect the RMS temperatures at the wall surface, which are damped by the thermal inertia of the wall.

Selvam *et al.* (2017) conducted LES of non-isothermal mixing in T-junctions with low branch velocities. The WALE model was adopted. LES results were compared with measurement values from the FSI facility (Kickhofel *et al.* (2016)). CHT was taken into account. Two cases were examined: (1) $\Delta T = 143$ K; and (2) $\Delta T = 65$ K. The optimal mesh size was estimated via the *a priori* analysis in Addad *et al.* (2008) – this strategy is described in Subsection 3.6.5. On average, LES and experimental temperatures showed good agreement in mean and power spectral density. LES and experimental RMS temperatures showed reasonable agreement, because LES either under- or overpredicted the experimental values at some locations. In the inspected areas, no dominant frequencies could be found from 0.1 to 10 Hz – see Subsection 2.1.3 for details about this frequency range.

2.1.7 CFD-FEA coupling for fatigue assessment

Fatigue can be predicted by coupling CFD and FEA. In this respect, NESC (see Subsection 2.1.2) proposed a four-level approach for predicting thermal fatigue life. In Level 3, fatigue damage is evaluated by considering the full local load spectra alongside fatigue *S-N* (Wöhler) curves (Dahlberg *et al.* (2007)).

Several authors have tried to predict fatigue damage using CFD data. In the studies reported below, unless otherwise noted, coupled CFD-FEA simulations of thermal, turbulent mixing in T-junctions were conducted; CHT was included; thermal loads were transferred from CFD to linear elastic analyses; and cumulative usage factors (CUFs) were computed using the rainflow-counting procedure and the Palmgren-Miner linear damage rule.

Chapuliot *et al.* (2005) conducted a very large eddy simulation (VLES) of thermal mixing in an austenitic steel T-junction with four upstream bends ($\Delta T = 160$ K). The Smagorinsky SGS model was adopted. Zero heat flux was prescribed at the steel-water interface. The simulation time equaled 20 s. Elastic stresses were computed by assuming steel properties at room temperature, a constant heat transfer coefficient, and thermal loading from the last 10 s of the VLES. The CFD mesh conformed to the FEA one. Crack growth was described through Paris' law.

Jhung (2013) conducted a URANS of thermal mixing in a T-junction ($\Delta T = 117$ K). The SST model was adopted. The CFD mesh conformed to the FEA one. CFD and FEA simulation times equaled 300 s and 200 s, respectively. CUFs at the seven locations inspected – four at the junction, three downstream – were similar to one another and very low.

Kim *et al.* (2013) conducted a DES of thermal mixing in an austenitic steel T-junction. The boundary conditions resembled those in Jhung (2013). In the one-way separate analysis, thermal stresses were only computed downstream of the T-junction, by assuming steel properties at a mean temperature. CFD and FEA simulation times reached 15 s and 5 s, respectively. CUFs became noteworthy after

applying a mean stress correction to one of the S - N curves under consideration via the modified Goodman equation.

Hurrell *et al.* (2015) conducted a URANS of thermal mixing in a T-junction with internal sleeve ($\Delta T = 200$ K). They conducted an LES on a subregion of interest. The WALE model was adopted. An adiabatic heat transfer model was applied: upstream heat losses through convection and conduction were neglected. Only the fluid and fluid-wall interfaces were meshed. Area-averaged heat transfer coefficients and temperature oscillations on the fluid-wall interfaces were mapped from the CFD mesh to the FEA one. The simulation time equaled 27 s. A mean stress correction was applied via the modified Goodman equation, analogously to Kim *et al.* (2013). Fatigue damage was also evaluated using modified maximum stress and sinusoidal in-phase cycling criteria, which ensured more conservatism than the rainflow approach.

Zhang and Lu (2016) conducted large eddy simulations of thermal mixing in a T-junction ($\Delta T = 80$ K). The Smagorinsky model was adopted. Three simulation times were examined: 5, 10, and 20 s; however, only LES temperature fluctuations of 5 s were applied as thermal loads to the FEA model. The CFD mesh was finer than the FEA one. A mean stress correction was applied via the modified Goodman equation, analogously to Kim *et al.* (2013) and Hurrell *et al.* (2015). The Von Mises equivalent stress concept converted the multiaxial stress tensor histories to uniaxial ones. Even though the Wöhler curve was extrapolated below the fatigue limit, CUFs appeared to be negligible.

Wilson *et al.* (2016) conducted large eddy simulations of thermal mixing in a T-junction at $\Delta T = 195$ K (Transient 1) and $\Delta T = 155$ K (Transient 2). The simulation time equaled 20 s, but the first 2 s were discarded. In areas of concern, CFD and FEA meshes had the same element size. For better statistics, the whole nodal stress history was decomposed into four intervals of 2.5 s each. After that, a simplified rainflow-counting method was applied to each interval. To enhance statistical confidence, CUF contour plots were created after the fatigue analysis results from each node had been merged with those from up to 46 adjoining nodes. The final CUFs increased considerably in Transient 1.

2.2 Uncertainty

In this work, the uncertainty of temperature measurement is estimated. Methods predicting the impact of thermocouple design and mounting on uncertainty, such as that suggested in Ould-Lahoucine and Khellaf (2005), could not be employed here, because these methods presume that water temperature can be expressed analytically.

This flaw was overcome in Dusarlapudi *et al.* by building a finite element model of the thermocouple. However, this technique alone is not sufficient to assess the relationship between uncertainty and thermocouple design and mounting when the vast dataset of temperature time series from the experiments under study is

considered.

Time constraints limited the application of methods requiring end-to-end calibration data for the data acquisition system (DAS) (Nakos (2004)).

2.3 IHCP

Inverse heat transfer problems (IHTPs) have gained attention during the last decades thanks to their technical and scientific applications. Following Hadamard, the IHTP is ill-posed (Beck *et al.* (1985)): i.e., this problem is highly affected by error, introduced by material properties, input data, or rounding. Furthermore, the solution may not be unique or exist.

Four classes of IHTPs can be distinguished by the type of information to be recovered: boundary, coefficient, retrospective (time-reverse), and geometric problems (Alifanov (1994)).

Moreover, IHTPs can be distinguished by heat transfer mechanism: conduction, convection, radiation, phase change (solidification or melting), or a blend of them (Özisik and Orlande (2000)).

Disparate discretization strategies can be applied: finite difference (Deng and Hwang (2007); Mohammadiun (2016)), control volume (Taler *et al.* (1997); Cebula and Taler (2014)), boundary element (Huang and Tsai (1998)), classical finite element (Jang *et al.* (2006); Lu *et al.* (2012); Dennis and Dulikravich (2012)), finite element with Trefftz functions (Grysa (2003)), or combinations of finite element and differential quadrature (Golbahar Haghghi *et al.* (2008)).

IHTPs are usually solved using regularization methods (Tikhonov and Arsenin (1977)), function specification procedures (Beck *et al.* (1985); Meresse *et al.* (2012)), gradient iterative methods (Alifanov (1974); Huang and Tsai (1998); Guo *et al.* (2017)), stochastic optimization approaches (Tian *et al.* (2011)), Monte Carlo techniques (Haji-Sheikh and Buckingham (1993); Orlande and Dulikravich (2012)), methods incorporating filtering techniques (Jang *et al.* (2006)), or neural networks (Krejsa *et al.* (1999); Aquino and Brigham (2006); Deng and Hwang (2007)).

Regularization allows to obtain a well-posed, stable problem by minimizing a cost function. Well-known regularization methods are Tikhonov regularization (Tikhonov and Arsenin (1977)), generalized eigensystem methods (Throne and Olson (2001)), energetic regularization (Ciałkowski *et al.* (2007)), and Alifanov's iterative regularization (Alifanov (1994)).

In the current CFD simulations, temperatures are sampled in the inner tube, a hollow cylinder echoing the control-rod stem under study. A boundary IHCP can be defined: transient temperature and heat flux on an inaccessible boundary (e.g., the water-inner tube interface) are estimated from transient temperature and heat flux on an accessible boundary (e.g., the unwet surface of the inner tube). The reconstructed temperature field can help to estimate thermal stresses and validate CFD results against temperature measurements taken at unwet surfaces of analogous structures. Here, recent work on 2D and 3D transient IHCPs is summarized:

2D domains are examined in Sections 3.7 and 4.6, but the method described here can be extended to 3D domains of arbitrary geometry.

In Cebula and Taler (2014), the transient heat flux on the wet surface of the control-rod stem was recovered using a space marching method from temperatures measured in the wall. Gram's polynomials filtered the input temperature histories to improve the robustness of the proposed method to measurement noise. The IHCP results were verified against CFD predictions (Tinoco *et al.* (2010)).

In Mohammadiun (2016), a hybrid optimization method, employing the conjugate gradient method (CGM) with an adjoint equation, allowed to calculate the heat flux on the outer boundary of a three-layer hollow cylinder from temperatures measured at one point in the domain. Side and inner boundaries were assumed to be insulated. A finite-difference discretization was applied. The proposed method proved stable to measurement noise, so no explicit regularization was added. The IHCP results were verified numerically. A mesh independence test was conducted.

In Guo *et al.* (2017), least-squares optimization allowed to determine temperatures on the inner boundary of a horizontal mixing tee from those on the outer boundary. Steepest descent and conjugate gradient methods were merged to solve the IHCP. The direct heat conduction problem (DHCP) was discretized using a finite difference method. Singular spectrum analysis was applied to denoise the input temperature time series. Time-step and mesh independence tests were conducted.

Despite the numerous attempts to solve boundary IHCPs satisfactorily, obtaining accurate, stable solutions is challenging, particularly if heat fluxes change substantially in space and transients are fast (Orlande and Dulikravich (2012)). Therefore, a theoretically well-grounded approach should be adopted which provides accurate results under noise corruption, on 3D domains, if material properties depend on temperature, with no assumptions on the functional forms (i.e., shapes) of the unknown boundary conditions.

Chapter 3

Methods

3.1 Experimental setup

3.1.1 Overview of the facility

The current experiments were performed in the HWAT (High-pressure WAter Test) loop at the Royal Institute of Technology, Stockholm, Sweden. The HWAT loop and test section are portrayed in Figs. 3.1, 3.2, 3.5, 3.6, and 3.7. The test section consists of an inner and an outer coaxial vertical tube. The inner tube (see Fig. 3.6) is manufactured from 316LN stainless steel. It is 2000 mm long. Its inner radius, R_{ii} , reads 12.5 mm, whereas its outer radius, R_{io} , reads 17.5 mm. The outer tube (see Fig. 3.6) can be pressurized at 9 MPa. Its inner radius, R_{oi} , reads 40 mm, whereas its outer radius, R_{oo} , reads 50 mm.

Hot and cold water streams flow into the annulus between the two tubes from two hot and two cold inlets. Mixed water exits the annulus from two outlets. All inlet pipes feature inner and outer diameters of 7.5 mm and 16 mm, respectively. The hot inlets are at $z = 800$ mm (see Fig. 3.6), at $\theta = 180^\circ$ and $\theta = 360^\circ$. The cold inlets are at $z = 150$ mm (see Fig. 3.6), at $\theta = 90^\circ$ and $\theta = 270^\circ$; hence, they are 90° from the hot inlets. This azimuthal offset homogeneously distributes residual stresses after welding and keeps the test section straight. Two cold inlets, instead of one, evenly distribute the incoming cold water. These inlets are so far from the mixing region that they are expected not to interfere with phenomena happening there (Pegonen *et al.* (2014)).

The two outlet pipes feature inner and outer diameters of 14 mm and 22.5 mm, respectively. They are at $z = 1000$ mm, not to affect the hot inlets.

The water flow is driven by a circulating pump, which supplies water to the preheater in Fig. 3.1. This heat exchanger includes 18 heating elements, each rated at 8 kW. The cold flow bypasses the preheater and enters the primary coolers, to reach the preset temperature at the cold inlets. A pressurizer downstream of the preheater damps potential pressure fluctuations (see Fig. 3.1).

Table 3.1 reports essential dimensions and boundary conditions in the HWAT

Table 3.1: Key parameters in the test section of the HWAT loop and in BWRs.

Parameter	HWAT loop	BWR (Tinoco <i>et al.</i> (2009))
Diameters of the hot inlets	7.5 mm	14.6 mm (upper bypass inlets) & 8 mm (lower bypass inlets)
Diameters of the cold inlets	7.5 mm	38 - 43 mm (hydraulic)
Outer diameter of the inner tube	35 mm	65 - 70 mm
Outer diameter of the outer tube	100 mm	~ 140 mm
Number of hot inlets	2	8 (upper bypass inlets) & 4 (lower bypass inlets)
Number of cold inlets	2	1
Water temperature at the hot inlets	549 K	549 K
Water temperature at the cold inlets	333 - 423 K	333 K
Pressure	7.2 MPa	7.2 MPa

loop and in BWRs Oskarshamn-3 and Forsmark-3.

3.1.2 Test-section thermocouples

19 K-type thermocouples sample temperatures at the test-section inner and outer tube. These thermocouples were installed based on Pegonen *et al.* (2014). Here, only six of these thermocouples are considered. They have a diameter of 0.5 mm, sample temperatures at the wet surface of the inner tube, and are termed $H1$, $H2$, $H3$, $H4$, $V1$, and $V4$. They are collectively termed inner-tube thermocouples, while the wet surface of the inner tube is called inner surface. The inner-tube thermocouples can sample inner-surface temperatures because their tips are level with the inner surface. Fig. 3.7 portrays the three thermocouple discs, which hold the inner-tube thermocouples steady. The left and mid discs are set in the inner-tube wall 90° of azimuth from each other. The same holds for the mid and right discs. The caps of the three discs are flush with the inner surface thanks to TIG welding. The center of the mid thermocouple disc, here called \hat{Q} , acts as a reference point for ascertaining the positions of the inner-tube thermocouples – see Table 3.2. If the inner tube were stationary, the inner-tube thermocouples could only sample temperatures in two narrow areas within the mixing region, $\sim 180^\circ$ apart, at approximately the same axial level. Moreover, technical constraints limit

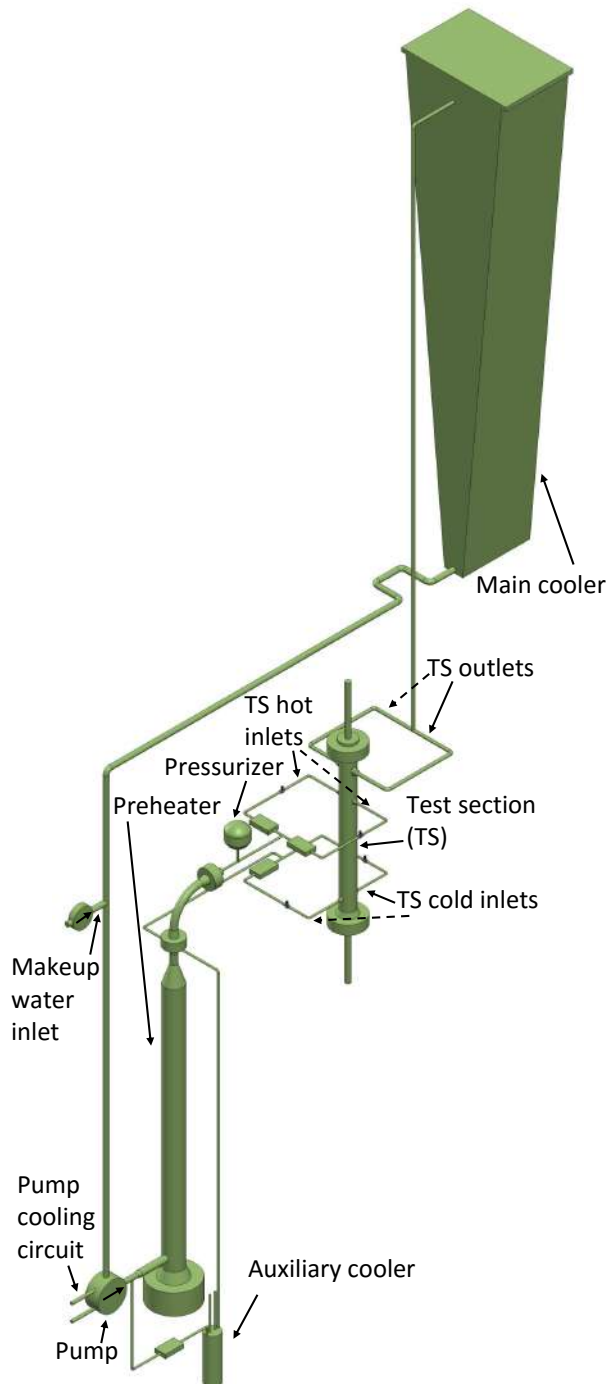


Figure 3.1: Major components of the HWAT loop. Rectangular cuboids represent flowmeters.



Figure 3.2: A picture of the test section.



Figure 3.3: A picture of the motor shaft.



Figure 3.4: A picture of a thermocouple disc.

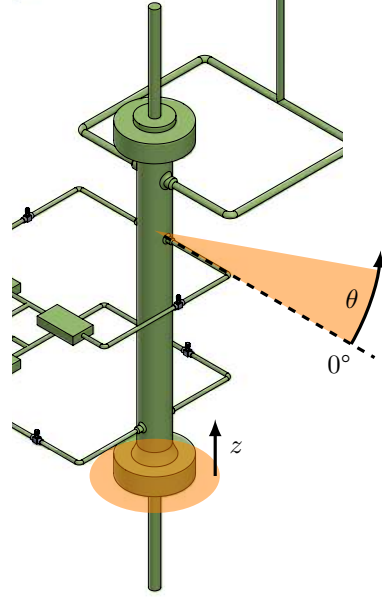


Figure 3.5: Cylindrical coordinate system fixed to the test section.

the number of installable inner-tube thermocouples. To circumvent these issues, the inner tube is rotated about its axis and translated before inner-surface temperatures are measured. This is attained by remotely driving a step motor, whose shaft is attached to the inner-tube base.

Angle $\hat{\gamma}$ in Fig. 3.8 is given as $\hat{\gamma} = \arcsin(r_i \cos(45^\circ)/R_{io})$. It is constant for $H1$, $H2$, $H3$, $H4$, $V1$, and $V4$. r_i indicates the shortest distance between the disc axis and the bottom of a hole through the same disc. The thermocouple placement is detailed in Bergagio and Anglart (2017).

3.1.3 Boundary conditions

Ten experimental cases are examined. Tables 3.3 and 3.4 list their boundary conditions. Overall, each case features different temperatures and mass flow rates at the test-section inlets, while pressure equals $p = 7.2$ MPa. Test-section temperatures are sampled at 1000 Hz for all cases in Table 3.3, and at 100 Hz for all cases in Table 3.4. To test experimental repeatability and the impact of sampling rate on the test-section temperatures measured, the boundary conditions in Cases 1 and 2 match those in Cases 5 and 7, respectively. As in Bergagio and Anglart (2017), adiabatic mixing temperature T_{mix} is calculated from adiabatic mixing enthalpy h_{mix} and pressure p . h_{mix} is given as $h_{mix} = (\dot{m}_C h_C + \dot{m}_H h_H) / (\dot{m}_C + \dot{m}_H)$, where h_H and h_C

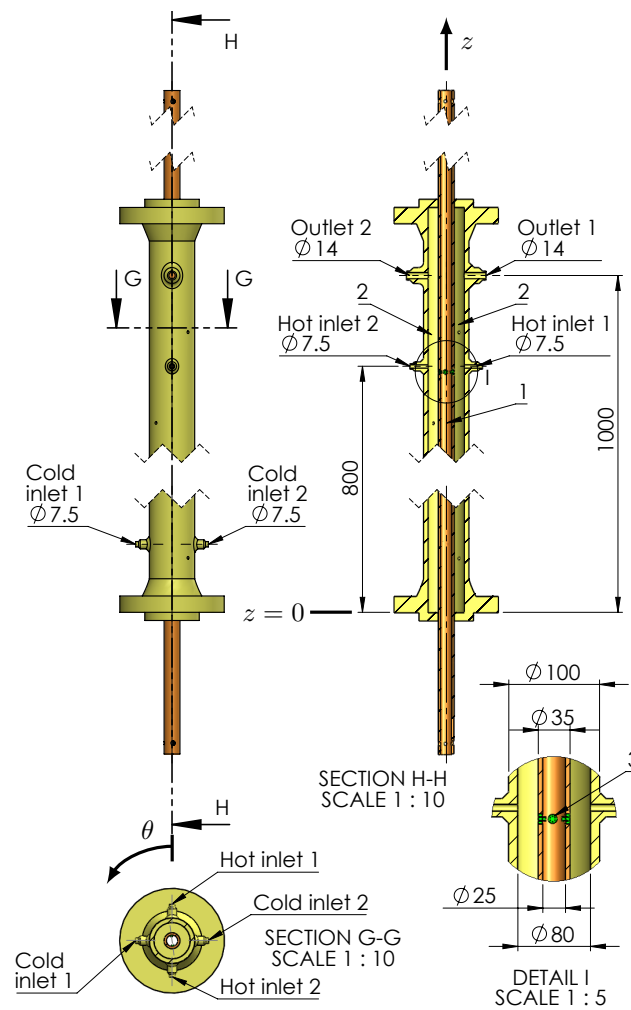


Figure 3.6: Sectional view of the test section. Red (1): inner tube. Gold (2): outer tube. Green (3): thermocouple discs. Axis of hot inlet 1 at $(360^\circ, 800 \text{ mm})$; axis of hot inlet 2 at $(180^\circ, 800 \text{ mm})$; axis of cold inlet 1 at $(90^\circ, 150 \text{ mm})$; axis of cold inlet 2 at $(270^\circ, 150 \text{ mm})$; axis of outlet 1 at $(360^\circ, 1000 \text{ mm})$; and axis of outlet 2 at $(180^\circ, 1000 \text{ mm})$. Dimensions are in mm.

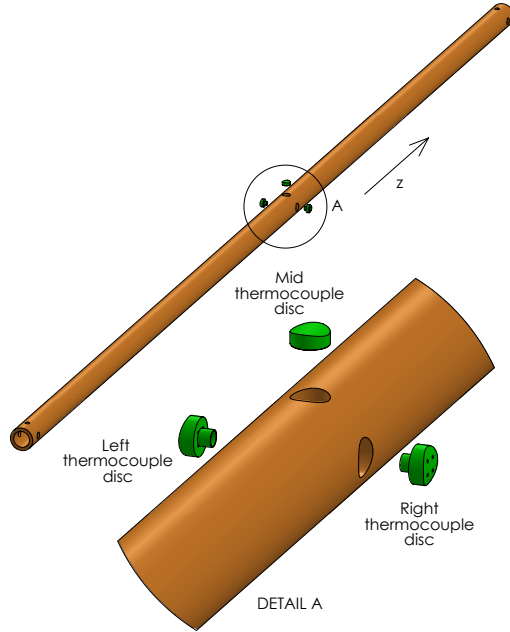


Figure 3.7: Exploded drawing of the inner tube, along with the thermocouple discs welded to it.

Table 3.2: Locations of the inner-tube thermocouple tips. $\Theta_Q[l; m]$ and $Z_Q[l; m]$ are described in Subsection 3.2.2. $H1$, $H2$, $H3$, and $H4$ are secured to the right thermocouple disc, while $V1$ and $V4$ are secured to the left one.

Label	r_f (mm)	z_f (mm)	θ_f ($^\circ$)
$H1$	R_{io}	$Z_Q[l; m] - r_i \sin(45^\circ)$	$\Theta_Q[l; m] + 90^\circ + \hat{\gamma}$
$H2$	R_{io}	$Z_Q[l; m] - r_i \sin(45^\circ)$	$\Theta_Q[l; m] + 90^\circ - \hat{\gamma}$
$H3$	R_{io}	$Z_Q[l; m] + r_i \sin(45^\circ)$	$\Theta_Q[l; m] + 90^\circ + \hat{\gamma}$
$H4$	R_{io}	$Z_Q[l; m] + r_i \sin(45^\circ)$	$\Theta_Q[l; m] + 90^\circ - \hat{\gamma}$
$V1$	R_{io}	$Z_Q[l; m] - r_i \sin(45^\circ)$	$\Theta_Q[l; m] - 90^\circ + \hat{\gamma}$
$V4$	R_{io}	$Z_Q[l; m] + r_i \sin(45^\circ)$	$\Theta_Q[l; m] - 90^\circ - \hat{\gamma}$

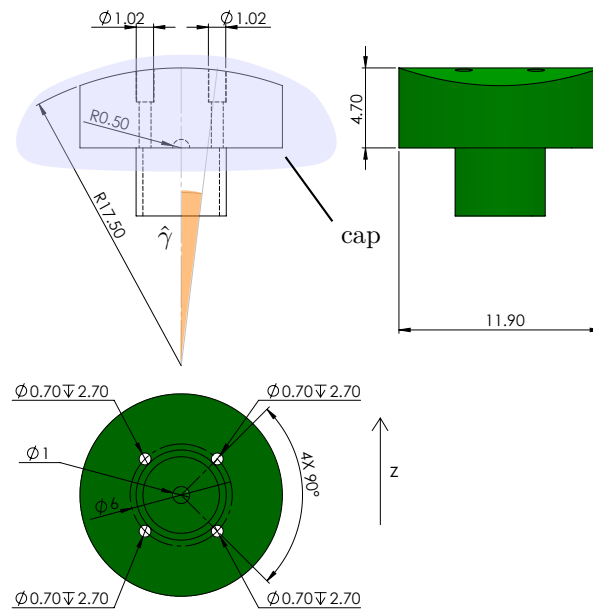


Figure 3.8: Sketch of the left and right thermocouple discs. Dimensions are in mm, if not otherwise indicated. “ $\varnothing 6$ ” designates $2r_i$.

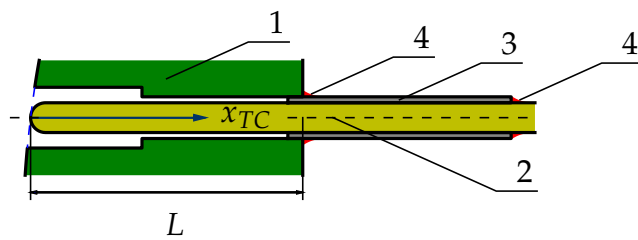


Figure 3.9: Longitudinal section of an inner-tube thermocouple. The cylinder in Fig. 3.8 is omitted for clarity. Green (1): thermocouple disc. Yellow (2): thermocouple. Gray (3): casing. Red (4): solder. $L \approx 4.5$ mm.

Table 3.3: Experimental matrix listing boundary conditions and T_{mix}^* when test-section temperatures are sampled at 1000 Hz.

Case no., or l	T_H (K)	T_C (K)	\dot{m}_H (kg s ⁻¹)	\dot{m}_C (kg s ⁻¹)	T_{mix}^* (-)	Re_H (-)	Re_C (-)
1	549	333	0.8	0.07	0.93	711 367	12 696
2	549	333	0.6	0.07	0.91	533 525	12 696
3	549	423	0.6	0.14	0.83	533 525	32 265
4	549	348	0.6	0.08	0.90	533 525	17 890

Table 3.4: Experimental matrix listing boundary conditions and T_{mix}^* when test-section temperatures are sampled at 100 Hz.

Case no., or l	T_H (K)	T_C (K)	\dot{m}_H (kg s ⁻¹)	\dot{m}_C (kg s ⁻¹)	T_{mix}^* (-)	Re_H (-)	Re_C (-)
5	549	333	0.8	0.07	0.93	711 367	12 696
6	549	423	0.8	0.07	0.93	711 367	32 265
7	549	333	0.6	0.07	0.91	533 525	12 696
8	549	423	0.6	0.07	0.91	533 525	32 265
9	549	333	0.4	0.07	0.87	355 684	12 696
10	549	423	0.4	0.07	0.86	355 684	32 265

denote enthalpies of the hot and cold streams, respectively. Dimensionless mixing temperature T_{mix}^* in Tables 3.3 and 3.4 is defined as $T_{mix}^* = (T_{mix} - T_C)/(T_H - T_C)$. Froude numbers related to these experimental cases are reported in Bergagio and Anglart (2017).

3.2 Data acquisition

For each case in Tables 3.3 and 3.4, steady-state boundary conditions are reached first. When this prerequisite is fulfilled, the inner tube is moved to preset positions, where the inner-tube thermocouples sample inner-surface temperatures.

3.2.1 Data acquisition tasks

The experimental data are saved on two laptops: (1) a laptop ‘‘A’’, setting the inner tube in motion and gathering temperature measurements from the test-section thermocouples; and (2) a laptop ‘‘B’’, collecting pressure, pressure drops, and temperatures from the remainder of the HWAT loop. Table 3.5 highlights that two devices communicate with laptop A: (1) a Measurement Computing (MC) 1608FS device; and (2) a National Instruments (NI) SCXI-1000 chassis. Concerning the former, it allows to determine the position of point Q based on the readings of two

potentiometers. Furthermore, on/off signals are sent to the circuit board on the step motor through this MC device, in order to move the inner tube.

The SCXI-1000 chassis holds a SCXI-1102 thermocouple amplifier module, to which a SCXI-1303 terminal block is connected. The extension wires of the test-section thermocouples are in turn connected to this terminal block. The SCXI-1000 is wired to a DAQ-6024 card, which is inserted into laptop A to connect the SCXI-1000 to this laptop.

Two devices transfer data to laptop B: an Agilent 34980A data logger, which collects temperature readings from thermocouples in other sections of the HWAT loop; and another MC 1608FS device, which acquires pressure readings from the pressure transducer and flowmeters in Fig. 3.1. The Agilent 34980A and MC 1608FS devices are connected to USB ports.

The mass flow rates through the test-section inlets are computed from specific loop temperatures, pressure, and pressure drops using empirical correlations. The GUI on laptop B displays the above mass flow rates, pressure, and loop temperatures of concern, updated at ~ 1 Hz. Throughout every experiment, mass flow rates and temperatures through the test-section inlets, along with pressure, are set off against values from the corresponding row in Table 3.3 or 3.4. When the match is within tolerance, the inner tube is translated and rotated about its axis until point \hat{Q} reaches a goal position. These positions form the inner-tube movement pattern, which is described in Subsection 3.2.2. Once the goal position has been reached, test-section temperatures are sampled and kept in an array of $NS_{0,DAS}$ samples per thermocouple, where $NS_{0,DAS} = 120\,000 \text{ S it}^{-1} \text{ ch}^{-1}$ (first iteration). After data collection and detrending, the variances of the inner-tube temperatures are checked for values higher than a preset threshold. When this occurs, test-section temperatures are sampled again and kept in an array of $NS_{1,DAS}$ samples per thermocouple, with $NS_{1,DAS} > NS_{0,DAS}$ (second iteration). The PyDAQmx module (Cladé (2010)) proves crucial to a straightforward data acquisition.

Two computers are essential to enhance the conformity of the actual boundary conditions with values in Tables 3.3 and 3.4, the accuracy of the inner-tube movement, and the significance of the inner-surface temperature measurements. Service NTP (Network Time Protocol) provides synchronization between laptops A and B. Table 3.5 lists relevant data acquisition parameters. As stressed in Table 3.5, test-section temperatures are recorded at $f_{S,DAS} = 1000 \text{ Hz}$: although temperature oscillations up to 10 Hz could be recorded at 100 Hz to fulfill the Nyquist-Shannon theorem and prevent aliasing (National Instruments (2016)), variances of inverse-filtered inner-surface temperatures sampled at 1000 Hz are confirmed to be more accurate in Section 4.1. Inverse-filtering is justified in Section 3.3.

Notwithstanding, Table 3.4 reports that test-section temperatures are also recorded at $f_{S,DAS}^f = 100 \text{ Hz}$ ($NS_{0,DAS}^f = 12\,000 \text{ S it}^{-1} \text{ ch}^{-1}$) under boundary conditions equaling those in Cases 1 and 2. Accordingly, test-section temperatures are sampled over 120 s it^{-1} in the first iteration at each location in the inner-tube movement pattern. 120 s it^{-1} allows to cover this pattern in a reasonable time and still deliver statistically relevant data.

Table 3.5: Overview of relevant data acquisition parameters. Underlined devices are wired to laptop A. Pressure drops help to calculate mass flow rates.

Device	Data acquired	f_S (Hz)	NC	NS_0 (Sit ⁻¹ ch ⁻¹)
<u>NI SCXI-1000</u>	Test-section temp.s	1,000 or 100	19	120,000 or 12,000
<u>MC 1608FS 1</u>	Position of point \hat{Q}	1,000	2	10
MC 1608FS 2	Pressure drops	100	4	10
MC 1608FS 2	Pressure	10,000	1	3,000
Agilent 34980A	Loop temp.s	48.74	13	10

Temperature arrays storing $NS_{0,DAS}$ inner-tube thermocouple readings (i.e., from the first iteration at each measurement location) are termed $T_{f,DAS}$ and are highly relevant to the current study.

3.2.2 Inner-tube movement pattern

One of the objectives of these experiments is to capture the temperature distribution on the inner surface. As already evidenced, this objective is accomplished by rotating and translating the inner tube, otherwise the measurement area would be too small. As shown in Fig. 3.5, a cylindrical coordinate system is fixed to the outer tube. Thus, point \hat{Q} can be defined by coordinates θ and z , which are provided by two potentiometers, as detailed in Table 3.5. The inner tube is fastened to the shaft of the step motor, so \hat{Q} can be moved between $z = 550$ mm and $z = 937$ mm (up and down), between $\theta = 0^\circ$ and $\theta = 360^\circ$ (clockwise and counterclockwise). The inner tube is typically rotated counterclockwise (when viewed from above) in increments of 45° ; hence, two adjoining measurement locations on the same axial level are 45° from each other. The inner tube is typically rotated clockwise once per axial level, when \hat{Q} is moved from $\theta = 360^\circ$ to $\theta = 0^\circ$. Test-section temperatures start being sampled 60 s after the target position has been reached, to damp temperature perturbations caused by rotation and translation. In each case l , \hat{Q} occupies a sequence of positions, which is termed inner-tube movement pattern ($\Theta_Q[l; 1, \dots, m^*]$, $Z_Q[l; 1, \dots, m^*]$). Fig. 3.10 displays the above pattern for Case 9. Each position ($\Theta_Q[l; m]$, $Z_Q[l; m]$) in a specific pattern yields measurement position $(\hat{\theta}, \hat{z})$ by computing θ_f and z_f from the formulas in Table 3.2, with $\hat{\gamma}$ and $r_i \sin(45^\circ)$ disregarded. Angle $\hat{\theta}$ is calculated by rounding the result. 360° is added or subtracted until $\tilde{\theta} = 45k$, $1 \leq k \leq 8$. It can be proved that the difference between z_f and \hat{z} is no more than $\pm(0.99 \text{ cm} + r_i \sin(45^\circ)) \approx \pm 1.20$ cm, while the difference between θ_f and $\hat{\theta}$ is no more than $\pm(\hat{\gamma} + 1^\circ) \approx \pm 7.96^\circ$ if differences of $\pm 360^\circ$ are disregarded. Overall, the mismatch is so slight that, in Subsection 3.3.1 and Section 4.1, θ_f and z_f replace $\tilde{\theta}$ and \tilde{z} , respectively.

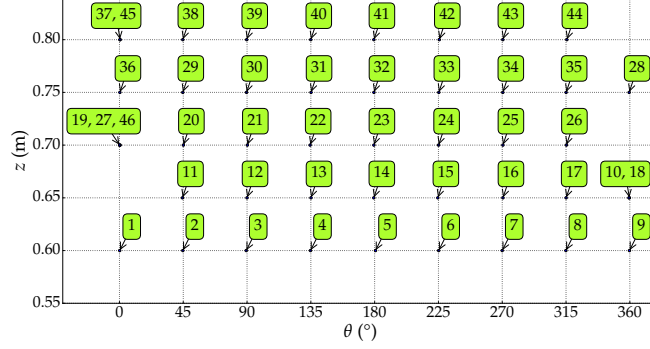


Figure 3.10: Inner-tube movement pattern for Case 9; i.e., $(\Theta_Q[9; 1, \dots, m^*], Z_Q[9; 1, \dots, m^*])$. Numbers in boxes mark the order in which the respective positions are reached; i.e., they indicate m , $1 \leq m \leq 46$.

3.3 Postprocessing

As already mentioned, inner-surface temperature time series from the first measurement iteration at a target position are mainly examined. Temperatures are measured for 120 s at 100 or 1000 Hz, conditioned by the 2 Hz low-pass filter included in the SCXI-1102 module (National Instruments (2004)), and stored on laptop A. Each of the above time series is converted to an array $T_{f, DAS}$, which holds $NS_{0, DAS}$ samples when the sampling rate equals 1000 Hz (as described in Section 3.2). Array $T_{f, DAS}$ is postprocessed in four steps:

1. It is inverse-filtered; hence, array $T_{f, if}$ is created, essentially unaltered by the 2 Hz low-pass filter included in the SCXI-1102 module.
2. $T_{f, if}$ is freed of its high-frequency content by an adequate low-pass filter. The filtered time series is called $T_{f, lf}$ and stores A samples, with $A < NS_{0, DAS}$. $T_{f, lf}$ often shows non-stationary, intermittent temperature oscillations. Sometimes trends can be discerned, possibly because of instabilities in boundary conditions.
3. A trend is determined and eliminated from array $T_{f, lf}$, which is called $T_{f, d}$ after being detrended.
4. $T_{f, d}$ is windowed. The windowed array is called $T_{f, w}$ and Fourier-transformed. Furthermore, $T_{f, d}$ is Hilbert-Huang transformed when it suggests strong, non-uniform mixing. If so, its Hilbert-Huang marginal spectrum is computed.

Data sampled at 100 Hz are similarly postprocessed.

3.3.1 Inverse- and low-pass filtering

In Step 1, each array $T_{f,DAS}$ is discrete Fourier-transformed. The spectrum thus computed is inverse Fourier-transformed after being multiplied by the inverse-filter response function, to recover real temperatures. The filter response is derived up to 10 Hz, based on various experiments. As this work mainly focuses on spectral components at frequencies below 4 Hz, a finite impulse response (FIR) filter is applied to damp out components at $f > 4$ Hz and to minimize ringing effects around 4 Hz. The filter order is termed C . Because of this filtering, C samples are corrupted by initial conditions, so they are removed. Therefore, each low-pass filtered array contained A samples, with $A = NS_{0,DAS} - C$.

To estimate how sampling rates alter inverse-filtered temperatures, a gain parameter G is proposed, along with a differential spread variable Δ . The former is defined as $G = T_2 - T_1 - (T_4 - T_3)$. Out of all the inverse-filtered temperatures at position (θ_f, z_f) for a specific case, T_1 and T_2 denote the lowest and highest values, respectively. Measurement position (θ_f, z_f) is introduced in Subsection 3.2.2. Concerning T_3 , first, each of the inverse-filtered temperatures at position (θ_f, z_f) for a specific case is sliced with a step length of $10 \text{ S it}^{-1} \text{ ch}^{-1}$, which yields ten sub-arrays. The arithmetic mean of the lowest values in these arrays is then added to a set. Processing each inverse-filtered temperature at (θ_f, z_f) for a specific case in an analogous way resizes the set to length L_1 , $6 \leq L_1 \leq 14$. T_3 represents the minimum of this set. T_4 is derived in a comparable way, by substituting maxima for minima.

Variable Δ is expressed as $\Delta = (\sigma_2^2 - \sigma_3^2)/\sigma_2^2$. σ_2^2 represents the mean variance of the inverse-filtered temperature arrays at (θ_f, z_f) for a specific case, whereas σ_3^2 is the mean variance of the ten aforementioned sub-arrays at (θ_f, z_f) for a specific case.

3.3.2 Empirical mode decomposition

Trend estimation and detrending are necessary because boundary conditions reveal instabilities throughout the data acquisition. Trend is a low-frequency signal that affects the spectra of inverse-filtered temperatures, so detrending is essential to better evaluate the thermocouple mounting error (see Section 3.5) and to study Fourier-based and Hilbert-Huang transforms at low frequencies. Keeping trends would affect the estimate of the thermocouple response, which depends on frequencies and amplitudes of water temperature close to the thermocouple (as shown by, e.g., Ould-Lahoucine (2004)).

The detrending method should be adaptive, capture local features of the signal to be detrended, and properly handle non-stationary signals. Many methods, including wavelets, smoothness prior approach (Tarvainen *et al.* (2002)), singular spectrum analysis (Alexandrov *et al.* (2012)), and empirical mode decomposition (EMD), allow to extract trends from one-dimensional time series. EMD can be implemented as follows:

1. Array $T_{f,lf}$ is renamed to r_0 . Index c is set to 1.
2. All local extrema in r_{c-1} are detected.
3. Envelope $e_{max,c-1}$ is created by spline interpolation of all local maxima.
4. Envelope $e_{min,c-1}$ is built from local minima in an analogous way.
5. Mean envelope $e_{mean,c-1}$ is calculated as the arithmetic mean of $e_{max,c-1}$ and $e_{min,c-1}$.
6. Detail d_c is extracted by subtracting $e_{mean,c-1}$ from r_{c-1} .
7. The same procedure is repeated for residual $e_{mean,c-1}$.

Steps 2 to 6, called “sifts”, are repeated with r_{c-1} being replaced by d_c , until d_c can be deemed as zero-mean under certain stopping criteria (Huang *et al.* (2003)). If they are met, d_c is regarded as an intrinsic mode function (IMF) g_c . Residual r_c is calculated as $r_c = r_{c-1} - g_c$. After c is set to 2, the same procedure is repeated for r_1 and all subsequent residuals, until the highest number of IMFs is reached or a monotonic residual is obtained. If either condition is met, Eq. 3.1 holds true:

$$\begin{aligned}
 T_{f,lf} &= g_1 + r_1 \\
 &= g_1 + g_2 + r_2 \\
 &= \dots \\
 &= \sum_{c=1}^G g_c + r_G .
 \end{aligned} \tag{3.1}$$

Here, g_c is the c -th IMF and r_G represents the final residual. The EMD algorithm is detailed in Huang *et al.* (2003), Rilling *et al.* (2003), and Wu and Huang (2009). In the present work, cubic and rational splines are tested in Steps 3 and 4. To determine envelopes interpolating all local extrema, rational splines with end-condition and tension parameters respectively equaling 1 and 5 (Peel *et al.* (2009)) are implemented. Rational splines are selected because they can reduce the under- and overshooting due to cubic spline interpolation. Details are considered IMFs if the number of zero-crossings differs from that of extrema at most by one, and if such numbers do not change for five successive “sifts” (Huang *et al.* (2003)). The highest number of IMFs is set to $K = \lfloor \log_2(A) \rfloor$, in accordance with Wu and Huang (2009) and Song *et al.* (2012). Trend Ξ is determined as

$$\Xi = \sum_{c=c_0}^G g_c + r_G . \tag{3.2}$$

Index c_0 is selected in conformity with Yang *et al.* (2013): the correlation coefficient between the Hilbert-Huang marginal spectrum of g_{i+1} and that of g_i exceeds threshold $\hat{\delta}$ ($0 < \hat{\delta} < 1$) starting from $i = c_0$.

3.3.3 Windowing, DFT, HHT, and Hilbert-Huang marginal spectrum

DFTs, HHTs, and Hilbert-Huang marginal spectra are to be calculated so as to find dominant frequencies at fatigue-prone locations. When thermal mixing is examined, frequency spectra of measurement and simulation data are typically determined using the DFT (see, e.g., Kamide *et al.* (2009) and Pasutto *et al.* (2005)). This method is popular as most researchers strive to show that their data tally with the Kolmogorov law in the inertial subrange – i.e., $E(\kappa) \propto \kappa^{-5/3}$, where κ is the wavenumber and E is the energy spectrum function – and to determine a range of frequencies for the assessment of thermal stresses in the adjoining walls. The former goal was pursued in Ayhan and Sökmen (2012) and Timperi (2014), the latter in Radu *et al.* (2009) and Hannink and Blom (2011). In the latter case, either the inner-surface or the bulk temperature is conjectured to change sinusoidally with time so as to compute stresses in the wall, compatibly with the so-called sinusoidal method (Dahlberg *et al.* (2007)). Consequently, non-periodicity and intermittency in these time series are neglected to focus instead on a range of critical frequencies which could speed up the fatigue growth process. Accordingly, time-frequency representations of non-periodic, intermittent temperature time series are seldom encountered in this kind of research. The Hilbert-Huang transform (HHT) blends the EMD method with the Hilbert spectral analysis, which allows to determine how frequencies and amplitudes in each time series change with time.

The HHT appears in some studies on turbulence, including Meng *et al.* (2011), Huang *et al.* (2013), and Konsoer and Rhoads (2014). In Meng *et al.* (2011), pressure measurements in a Kenics static mixer were analyzed through the HHT under various flow regimes. Huang *et al.* (2013) processed velocities from direct numerical simulations (DNS) of isotropic homogeneous 3D turbulence at $Re_{\lambda_{RM}} = 400$ using the HHT. Here, $Re_{\lambda_{RM}}$ is Re based on Taylor microscale λ_{RM} . More precisely, second-order Hilbert-based statistical moments of the aforementioned velocity time series were calculated from their Hilbert spectra.

In Konsoer and Rhoads (2014), time series of streamwise and spanwise velocity, temperature, and backscatter intensity at the mixing interfaces of two river confluences were studied. As the meeting rivers exhibited different temperatures, the turbulent mixing of non-isothermal flows could be examined. The EMD algorithm decomposed the above time series. The IMFs most responsible for peaks in the Hilbert-Huang marginal spectra of streamwise and spanwise velocity, temperature, and backscatter intensity were recognized, along with dominant frequencies. The correlation between distance from the confluence apex and the above frequencies was also investigated.

Windowing is required to decrease edge discontinuities before Fourier-transforming the detrended data. Windows taken into account are listed in Bergagio *et al.* (2017). The window which minimizes the difference between the variance of windowed array $T_{f,w}$ and that of detrended array $T_{f,d}$ is selected. The window length equals $1 \cdot 2^{15}$ S, or 32.768 s, in cases from Table 3.3, and $1 \cdot 2^{12}$ S, or 40.96 s, in cases

from Table 3.4.

The DFT approach presents some serious drawbacks: it represents non-stationarity by adding fake harmonics and is sensitive to noise. Moreover, Fourier transform-based time-frequency representations of non-stationary time series, including short-time Fourier transforms and wavelets, entail some shortcomings, the most relevant being that these descriptions are not data-driven: they cannot adapt to the signals, so they always require preset basis functions. Additionally, Fourier transform-based descriptions of non-stationary signals are constrained by the Heisenberg-Gabor uncertainty relation, which dictates a balance between time and frequency localizations. For example, in the case of wavelet transforms, the frequency resolution could be low at high frequencies, which increases the time resolution, whereas the reverse could hold at low frequencies (Mohlkamp and Pereyra (2008)).

Owing to the HHT, the non-stationary, intermittent nature of the inner-surface temperature time series under study is highlighted, and the change of IMF amplitudes and frequencies with time is explored. The HHT is a convolution of an IMF, according to Eq. (3.3)

$$\mathcal{H}[g_c[n]] = \frac{j}{\pi n} * g_c[n] \quad \text{for } n = 1, \dots, A, \quad (3.3)$$

where $*$ denotes the convolution symbol, j is the imaginary unit, and $\mathcal{H}[g_c[n]]$ represents the HHT of $g_c[n]$. Analytic signal z_c depends on the IMF and its HHT

$$\begin{aligned} z_c[n] &= g_c[n] + j\mathcal{H}[g_c[n]] \\ &= a_c[n] \exp(-j\theta_c[n]) \quad \text{for } n = 1, \dots, A. \end{aligned} \quad (3.4)$$

Here, amplitude a_c and phase θ_c are defined as

$$a_c[n] = \sqrt{g_c^2[n] + (\mathcal{H}[g_c[n]])^2} \quad (3.5)$$

and

$$\theta_c[n] = \arctan\left(\frac{\mathcal{H}[g_c[n]]}{g_c[n]}\right), \quad (3.6)$$

respectively. Unlike Fourier-based transforms, the frequency resolution does not depend on the time-window width: the instantaneous frequency, which differs from sampling frequency f_S , is given in Eq. (3.7) (Taner *et al.* (1979))

$$\omega_c[n] = \frac{1}{2\pi} \frac{d\theta_c[n]}{dt[n]} = \frac{1}{2\pi} \frac{\frac{d\mathcal{H}[g_c[n]]}{dt[n]} g_c[n] - \frac{dg_c[n]}{dt[n]} \mathcal{H}[g_c[n]]}{g_c^2[n] + (\mathcal{H}[g_c[n]])^2} \quad \text{for } n = 1, \dots, A. \quad (3.7)$$

The Hilbert spectrum is defined as $H_c[\omega_c[n]; n] = a_c[n]$; in other words, amplitudes at times and instantaneous frequencies from all IMFs of a (detrended) signal form its HHT spectrogram.

The instantaneous frequency is then discretized as $k \Delta\omega$, $k \in \mathbb{N}$, for all indices c and n , so that the Hilbert-Huang marginal spectrum can be calculated as

$$h_c[k\Delta\omega] = \sum_n H_c[k\Delta\omega; n]. \quad (3.8)$$

This spectrum appraises the energy density at frequency $k \Delta\omega$. In this work, $k \Delta\omega$ is called ω . Differently from the Fourier spectrum, the Hilbert-Huang marginal spectrum helps to properly interpret non-stationary and nonlinear processes (Huang *et al.* (1998)). Moreover, it solves the energy leakage problem in the Fourier spectrum (Frei and Osorio (2007)), which adds harmonic components to simulate non-stationarity. By doing so, it distributes the energy content of spectral peaks over a broader frequency range. In this research, the Hilbert-Huang transform is selected to study the detrended inner-surface temperatures at the locations most susceptible to fatigue damage and strong mixing inhomogeneity.

The respective Hilbert-Huang marginal spectra are also computed.

Fig. 3.11 portrays Fourier and Hilbert-Huang marginal spectra of an illustrative time series. The Hilbert-Huang marginal spectrum properly identifies all frequencies in the time series under study. Moreover, it outshines the Fourier spectrum at small frequencies ($f < 1$ Hz), because Fig. 3.11 shows the Hilbert-Huang marginal spectrum of the detrended time series. In this case, the Hilbert-Huang marginal spectrum appears affected by modulation of the sine component at 5 Hz more than its Fourier analogue. Notwithstanding, concerning non-periodic, intermittent signals, the strengths of adopting Hilbert-Huang marginal spectra are expected to greatly outweigh potential weaknesses.

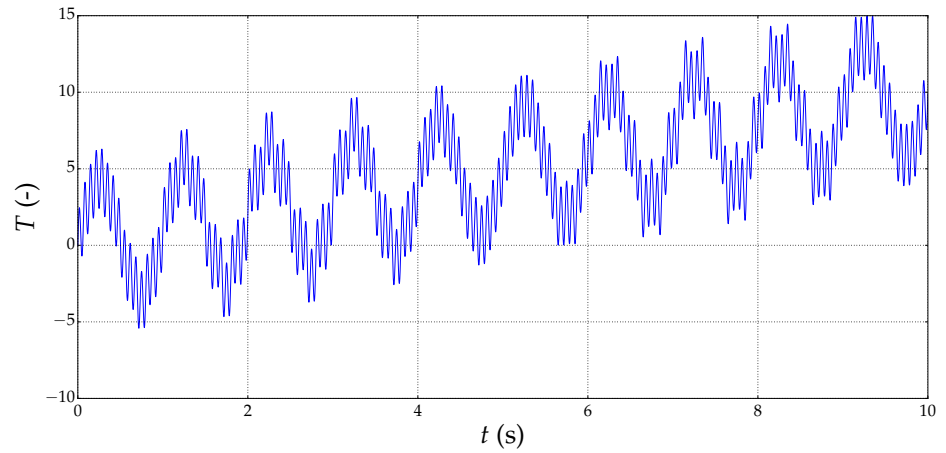
3.4 Mixing intensity

As established in Subsection 2.1.5, assessing mixing intensity and non-uniformity from inner-surface temperatures is one of the primary objectives of this study. A measurement position is here identified by coordinate pair (θ^*, z^*) . As time series at (θ^*, z^*) are well correlated and experimental measurements there seem repeatable (see Sections 4.1 and 4.2), blending all time series at (θ^*, z^*) into a single scalar descriptor of mixing intensity and non-uniformity appears justified. The above scalar should appropriately reflect variance, range (that is, the difference between the highest and lowest values), and frequencies of the inner-surface temperature time series at measurement position (θ^*, z^*) . To this objective, a scalar function is evaluated

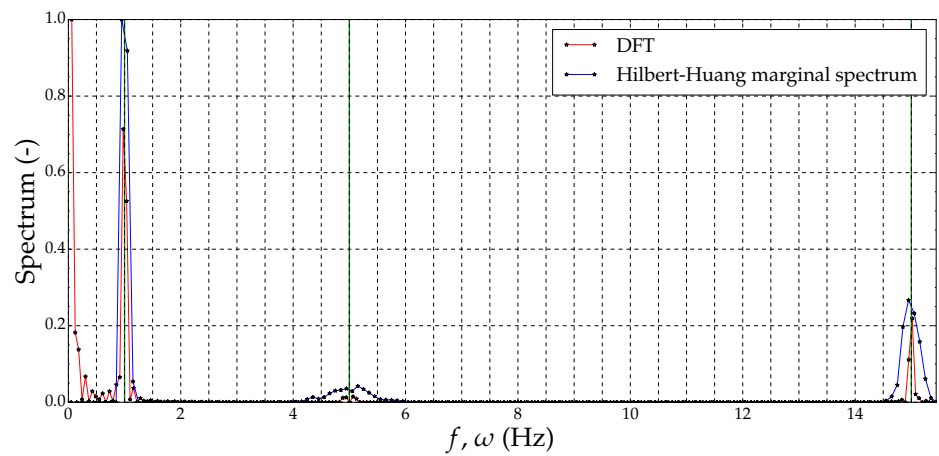
$$\sigma_0 = \sigma(T_{f,d}^*) , \quad (3.9)$$

$T_{f,d}^*$ denoting temperature $T_{f,d}$ from Eq. (3.10)

$$T_{f,d}^* = \frac{T_{f,d} - \tilde{T}_C}{\tilde{T}_H - \tilde{T}_C} \quad (3.10)$$



(a) Temperature time series.



(b) Fourier and Hilbert-Huang marginal spectra of the time series in Fig. 3.11(a). Green vertical lines mark its frequencies.

Figure 3.11: Representative temperature time series $T(t)$ and its spectra. Here, $T(t) = 2 \sin(30 \pi t) + \sin(10 \pi t) \sin(0.2 \pi t) + 4 \sin(2 \pi t) + t$.

after normalization. As the mass flow rates through the cold inlets are slightly dissimilar, \tilde{T}_C is their mean temperature weighted over the respective mass flow rates. \tilde{T}_H is defined in an analogous way. As stated in Subsection 3.2.1, inlet mass flow rates and temperatures are sampled at 1 Hz. \tilde{T}_C and \tilde{T}_H are then interpolated in time to reach the sampling rate of temperature $T_{f,DAS}$.

Henceforth, tensor multi-indices are omitted to ease notation.

Scalar σ_0 is calculated for each array of detrended inner-surface temperatures $T_{f,d}$. Six time series are assigned to measurement position (θ^*, z^*) : four from thermocouples $H1$, $H2$, $H3$, and $H4$ at $(\theta^* + 90^\circ, z^*)$; two from $V1$ and $V4$ at $(\theta^* - 90^\circ, z^*)$. Sometimes eight or even ten time series are assigned to (θ^*, z^*) after a thermocouple has recorded more than one $T_{f,DAS}$, at $(\theta^* - 90^\circ, z^*)$ or $(\theta^* + 90^\circ, z^*)$. All inner-surface temperatures recorded at $(z^* - 1.20 \text{ cm}, z^* + 1.20 \text{ cm})$ and $(\theta^* - 7.96^\circ, \theta^* + 7.96^\circ)$ – these ranges are reported in Subsection 3.2.2 – are ascribed to measurement position (θ^*, z^*) . Accordingly, n^* values of σ_0 , n^* being equal to 6, 8, or 10, are computed at measurement position m_u in case l . In the above description, differences of $\pm 360^\circ$ are neglected for simplicity.

A single mixing descriptor should relate to position m_u , so first the modified Z-score from Iglewicz and Hoaglin (1993) helps to remove \check{n} outliers from the set of scalars σ_0 at m_u , with $\check{n} \in \mathbb{N}^0$. The set comprises \bar{n} scalars after outlier rejection, with $\bar{n} = n^* - \check{n}$. Next, the arithmetic mean of the \bar{n} non-outlier values is calculated and termed $\bar{\sigma}_0$. Last, $\bar{\sigma}_0$ is divided by the highest $\bar{\sigma}_0$ in case l for normalization. Each normalized $\bar{\sigma}_0$ is described in object $\hat{\sigma}$ by two indices, one referring to measurement position m_u , the other to case l .

Henceforth, $\hat{\sigma}$ is called “mixing estimator”. In Bergagio *et al.* (2017), mixing intensity was estimated by pairing $\hat{\sigma}$ with another scalar function.

3.5 Uncertainty analysis

The uncertainty of inner-surface temperature measurement in cases from Table 3.3 is computed from three uncertainty sources:

1. thermocouple intrinsic accuracy (B_{TC}^+ , B_{TC}^- , S_{TC});
2. thermocouple mounting error (B_{mount}^+ , B_{mount}^- , S_{mount}); and
3. absolute accuracy (B_{acq}^+ , B_{acq}^- , S_{acq}) of the data acquisition hardware.

These uncertainty sources are supposed independent of one another.

The intrinsic accuracy is reported by the manufacturer (Bergagio *et al.* (2015)).

The mounting error is assessed from a finite element simulation of a 2D axisymmetric inner-tube thermocouple in the region where mixing is most inhomogeneous. Software FreeFem++ (Hecht (2012)) is employed to this objective. Temperature in the thermocouple is considered independent of azimuth. Around the thermocouple, water is assumed stagnant, at a spatially uniform, time-varying temperature (Bergagio *et al.* (2015)).

The absolute accuracy of the data acquisition hardware includes all connections between each thermocouple and laptop A: the extension cable inserted into the thermocouple connector; the SCXI-1303 32-channel terminal block the extension cable is wired to; the SCXI-1102 amplifier module in the SCXI-1000 chassis; and the DAQ-6024E card. The absolute accuracy is calculated from end-to-end calibration data: evaluating it from system noise, offset, and gain error – all constituting the absolute accuracy reported by the manufacturer (National Instruments (2008), National Instruments (2004)) – would amplify it. Calibration data are obtained as detailed in Bergagio and Anglart (2017). The DC voltage signals used for calibrating are set to $2.9 \text{ mV} + i \text{ mV}$, with $i = 0, \dots, 8$. Room temperature is measured while performing end-to-end calibration, to convert DC voltages into expected temperature readings.

Bias B_{acq}^+ is then computed as

$$B_{acq}^+ = \max(|\overline{err}_{acq} + 2\sigma_{err, acq}|, |\overline{err}_{acq} - 2\sigma_{err, acq}|) . \quad (3.11)$$

Here, \overline{err}_{acq} denotes the mean of the average errors per set point and channel. $\sigma_{err, acq}$ represents the mean standard deviation of the average errors per set point and channel. B_{acq}^- is the opposite of B_{acq}^+ . Random uncertainty S_{acq} is computed as the mean of the highest standard deviations per set point and channel (National Instruments (2004)). Both B_{acq}^+ and S_{acq} are calculated from inverse-filtered temperatures (see Section 3.3).

Total uncertainty U_{95} and its shift ΔU_{95} are defined as

$$U_{95} = 2\sqrt{\frac{(\|\tilde{B}^+\| + \|\tilde{B}^-\|)^2}{16} + \|\tilde{S}\|^2} \quad (3.12)$$

and

$$\Delta U_{95} = 1/2 \left(\|\tilde{B}^+\| - \|\tilde{B}^-\| \right) , \quad (3.13)$$

respectively (Nakos (2004)). Here, $\tilde{B}^\pm = [B_{TC}^\pm, B_{acq}^\pm, B_{mount}^\pm]$, while $\tilde{S} = [S_{TC}, S_{acq}, S_{mount}]$.

3.6 LES, FEA, and fatigue assessment

The following workflow is adopted:

1. An LES of the whole test section is performed using experimental boundary conditions.
2. An FEA of the inner tube is conducted using LES temperature and pressure.
3. CUFs are determined in a region of the inner tube using LES temperature and FEA stresses.

4. A frequency analysis is conducted in the zones with the highest CUFs.

3.6.1 Governing equations

The equations are solved using OpenFOAM 4.1. The transient solver selected is `chtMultiRegionFoam`, which solves the CHT between solid and compressible flow regions.

An LES approach is adopted because previous URANS underpredicted temperature variations (Gallego-Marcos (2013); Haces Manzano (2013)).

The Favre-filtered mass continuity equation is presented below:

$$\frac{\partial \bar{\rho}}{\partial t} + \nabla \cdot (\bar{\rho} \tilde{\mathbf{u}}) = 0. \quad (3.14)$$

Here, $\tilde{\mathbf{u}}$ is the Favre-filtered velocity and $\bar{\rho}$ is the low-pass filtered density.

The Favre-filtered momentum equation is expressed as follows:

$$\frac{\partial (\bar{\rho} \tilde{\mathbf{u}})}{\partial t} + \nabla \cdot (\bar{\rho} \tilde{\mathbf{u}} \otimes \tilde{\mathbf{u}}) = -\nabla p^* + \nabla \cdot \tilde{\boldsymbol{\tau}}_{\text{eff}} + \bar{\rho} \mathbf{g}. \quad (3.15)$$

Here, \mathbf{g} is the gravitational acceleration. Modified pressure p^* is given as $p^* \approx \bar{p} + \frac{1}{3} \text{tr}(\boldsymbol{\tau}_{\text{SGS}})$. \bar{p} is the low-pass filtered pressure.

The effective stress tensor $\tilde{\boldsymbol{\tau}}_{\text{eff}}$ is expressed as follows:

$$\tilde{\boldsymbol{\tau}}_{\text{eff}} = 2 \mu_{\text{eff}} \left(\tilde{\mathbf{S}} - \frac{1}{3} (\nabla \cdot \tilde{\mathbf{u}}) \mathbf{I} \right). \quad (3.16)$$

The rate-of-strain tensor $\tilde{\mathbf{S}}$ is the symmetric part of the velocity gradient:

$$\tilde{\mathbf{S}}(\tilde{\mathbf{u}}) = \frac{1}{2} \left(\nabla \tilde{\mathbf{u}} + (\nabla \tilde{\mathbf{u}})^T \right). \quad (3.17)$$

The Favre-filtered energy equation is presented below:

$$\frac{\partial (\bar{\rho} \tilde{h})}{\partial t} + \nabla \cdot (\bar{\rho} \tilde{\mathbf{u}} \tilde{h}) + \frac{\partial (\bar{\rho} \tilde{K})}{\partial t} + \nabla \cdot (\bar{\rho} \tilde{\mathbf{u}} \tilde{K}) = -\nabla \cdot \tilde{\mathbf{q}}_{\text{eff}} + \bar{\rho} \tilde{\mathbf{u}} \cdot \mathbf{g}. \quad (3.18)$$

Here, \tilde{h} is the Favre-filtered enthalpy, while \tilde{K} is the resolved kinetic energy per unit mass; i.e., $\tilde{K} = |\tilde{\mathbf{u}}|^2/2$. Derivative $\partial \bar{p}/\partial t$ is omitted to ensure convergence when density varies with temperature. Mechanical source $\nabla \cdot (\boldsymbol{\tau} \cdot \mathbf{u})$, which denotes the work rate done by the viscous force on the fluid, is also omitted. Heat flux $\tilde{\mathbf{q}}_{\text{eff}}$ is given below:

$$\tilde{\mathbf{q}}_{\text{eff}} = -\alpha_{\text{eff}} \nabla \tilde{h}. \quad (3.19)$$

Eq. (3.18) reduces to

$$\frac{\partial (\rho_S h_S)}{\partial t} = -\nabla \cdot \mathbf{q}_S \quad (3.20)$$

in the solid regions. Here, \mathbf{q}_S is given as follows:

$$\mathbf{q}_S = -\alpha_S \nabla h_S, \quad (3.21)$$

where $h_S := h_S(T_S)$ and $\alpha_S = \lambda_S(T_S)/c_S(T_S)$. Wall temperature $T_{f,d}$ is estimated by coupling the heat fluxes from Eqs. (3.19) and (3.21) after linear approximation:

$$\frac{\lambda(\tilde{T}_1)}{\delta_1} (\tilde{T}_1 - T_{f,d}) \approx \frac{\lambda_S(T_2)}{\delta_2} (T_{f,d} - T_2), \quad (3.22)$$

where δ denotes the distance from the wall, while indices 1 and 2 represent the first cell centers from the wall in the fluid and solid zones, respectively. Several methods allow to estimate $T_{f,d}$. In some cases (e.g., supercritical fluids), Eq. (3.22) is not accurate. However, in this case, it can be proved that $T_{f,d}$ from Eq. (3.22) agrees with that from Tuominen (2015).

3.6.2 SGS model

Through filtering an SGS eddy viscosity μ_{SGS}

$$\mu_{\text{eff}} = \mu(\tilde{T}) + \mu_{SGS} \quad (3.23)$$

and an SGS thermal diffusivity α_{SGS}

$$\alpha_{\text{eff}} = \frac{\lambda(\tilde{T})}{c_p(\tilde{T})} + \alpha_{SGS} \quad (3.24)$$

are obtained from Eqs. (3.15) and (3.18), respectively. If the Reynolds analogy is invoked, α_{SGS} is taken to be proportional to μ_{SGS} :

$$\alpha_{SGS} = \frac{\mu_{SGS}}{Pr_{SGS}}. \quad (3.25)$$

Here, the turbulent Prandtl number, Pr_{SGS} , equals 0.85. μ_{SGS} in Eqs. (3.23) and (3.25) is computed via the WALE model (Nicoud and Ducros (1999)), which reproduces the δ^3 scaling of μ_{SGS} near the wall. It also ensures zero μ_{SGS} in isotropic contractions/expansions and pure shear regions, without dynamic procedures or damping functions (Nicoud *et al.* (2011)). The WALE model is the simplest approach that intrinsically guarantees zero μ_{SGS} in laminar shear flows, which is crucial when modeling transitional flows (Menter (2015)). Additionally, compared to the WALE model, the Smagorinsky one is more affected by the model constant (STAR-CCM+ (2018)). In the WALE model, μ_{SGS} is computed as follows:

$$\mu_{SGS} = C_k \bar{\rho} \Delta \sqrt{k_{SGS}}. \quad (3.26)$$

SGS kinetic energy k_{SGS} is given by Eq. (3.27):

$$k_{SGS} = \left(C_w^2 \frac{\Delta}{C_k} \right)^2 \frac{(\tilde{\mathbf{S}}^d : \tilde{\mathbf{S}}^d)^3}{\left((\tilde{\mathbf{S}} : \tilde{\mathbf{S}})^{5/2} + (\tilde{\mathbf{S}}^d : \tilde{\mathbf{S}}^d)^{5/4} \right)^2}. \quad (3.27)$$

Hence, k_{SGS} is computed from the rate-of-strain tensor $\tilde{\mathbf{S}}$ and from the deviatoric symmetric part of the velocity gradient squared $\tilde{\mathbf{S}}^d$

$$\tilde{\mathbf{S}}^d = \mathbf{B} - \frac{1}{3} \text{tr}(\mathbf{B}) \mathbf{I}. \quad (3.28)$$

Here, $\mathbf{B} = 1/2 (\mathbf{A} + \mathbf{A}^T)$, with $\mathbf{A} = \nabla \tilde{\mathbf{u}} \cdot \nabla \tilde{\mathbf{u}}$.

Model constants C_k and C_w in Eq. (3.27) are set to 0.094 and 0.5, respectively. Filter width Δ is expressed as $\Delta = V^{1/3}$, V being the cell volume. This Δ is adequate for isotropic hexahedral meshes.

3.6.3 Numerical methods

Pressure and velocity are coupled using the PIMPLE (merged PISO-SIMPLE) algorithm (OpenFOAM (2017)). PIMPLE allows time steps to exceed the Courant-Friedrichs-Lewy limit, while still keeping numerical stability: here, $Co \rightarrow 2^-$, so $\Delta t = 8 \times 10^{-6}$ s. A Crank-Nicolson time integration scheme and limited linear divergence schemes are selected. The latter conform to the total variation diminishing (TVD) criterion: Sweby filters are applied to linear (that is, central differencing) schemes (Sweby (1984)). Unlimited central differencing yields oscillations in the solutions to convective-diffusion problems if cell $Pe > 2$ (Patankar (1980)); furthermore, unlimited central differencing triggers unphysical velocity fluctuations at the inlets of a mixing tee meshed using hexahedral cells (Timperi (2014)). Gradient terms are computed by linear interpolation; their components are identically bounded to improve stability. The discretization of surface-normal gradient terms is enhanced using an explicit non-orthogonal correction.

A preconditioned conjugate gradient (PCG) linear solver is selected for the pressure equation. A diagonal incomplete-Cholesky (DIC) preconditioner is specified. The final residual at each time is fixed at 1×10^{-9} . A stabilized preconditioned bi-conjugate gradient (PBiCGStab) solver is selected for the remaining scalar equations and for the momentum equation. In this case, a diagonal incomplete-LU (DILU) preconditioner is specified. The final residuals at each time are fixed at 1×10^{-11} .

3.6.4 Properties

Density ρ , viscosity μ , conductivities λ and λ_S , and specific heat capacities c_p and c_S vary with temperature. Water properties are polynomials fit to the IAPWS-IF97 data (Wagner *et al.* (2000)), while 316LN stainless steel properties λ_S and c_S

are polynomials supplied with the MPDB software (Software Inc. (2015)). ρ_S is reasonably constant with temperature.

3.6.5 Space domain and mesh

The meshed regions – namely, water, inner tube, and outer tube – are depicted in Fig. 3.13. The geometry is described in Subsection 3.1.1. The modeled inlets and outlets are 30 mm long. The cell size in the LES mesh is computed from Taylor microscale λ_{RM} and from integral length scale L_{RM} (Addad *et al.* (2008)):

$$\Delta = \max\left(\lambda_{RM}, \frac{L_{RM}}{10}\right). \quad (3.29)$$

λ_{RM} and L_{RM} are computed from a precursor RANS according to Eqs. (3.30)

$$\lambda_{RM} = \sqrt{15 \frac{\mu k_{RM}}{\rho \varepsilon_{RM}}} \quad (3.30)$$

and (3.31)

$$L_{RM} = \frac{k_{RM}^{3/2}}{\varepsilon_{RM}}, \quad (3.31)$$

respectively (Addad *et al.* (2008)). k_{RM} and ε_{RM} are the turbulence kinetic energy and its rate of dissipation, respectively. A multi-block structured mesh is built from Eq. (3.29) using ICEM CFD 18.0. The mesh near the hot inlets is shown in Fig. 3.14. Water cells smaller than $1 \times 10^{-11} \text{ m}^3$ are mainly found near inlets, outlets, and inner tube.

The water region comprises 17.32×10^6 cells, while the inner tube and the outer tube comprise 2.61×10^6 and 4.70×10^6 cells, respectively. O-grids at the inlets and outlets allow to decompose both the water region in these pipes and the intersections between these pipes and the outer tube into high-quality hexahedral cells, as detailed in Table 3.6. The mesh is conformal between the water and steel regions. No wall functions are introduced.

In the mixing region, the first cell off the inner tube is $3.46 \times 10^{-5} \text{ m}$ thick; hence, $y^+ \approx 5$ on the inner surface. Fig. 3.12 highlights that the time-averaged y^+ varies from 0.09 to 9.40 at $0.60 \text{ m} \leq z \leq 0.73 \text{ m}$. These axial levels are examined because computational and experimental temperatures are compared at $0.63 \text{ m} \leq z \leq 0.72 \text{ m}$.

In the mixing region, the first cell off the outer tube is $6.92 \times 10^{-5} \text{ m}$ thick; hence, $y^+ \approx 6$ on the outer surface (i.e., on the water-outer tube interface).

The cell thickness smoothly increases in the water layer next to the wall. In both cases, a growth rate of 1.15 is set for the first two cells.

In the mixing region, the axial resolution equals 0.8 mm. It is 5.3 times smaller than the axial distance between thermocouple tips on the left thermocouple disc.

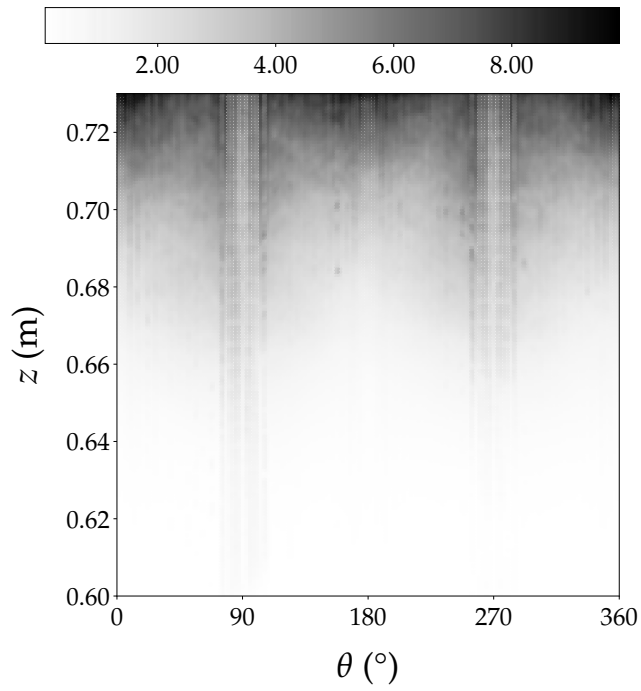


Figure 3.12: Time-averaged y^+ , at $0.60 \text{ m} \leq z \leq 0.73 \text{ m}$. Inner surface. Start time $t_0 = 19.2 \text{ s}$. Optimal mesh.

Table 3.6: Key mesh quality parameters.

Region	Maximum aspect ratio	Mean non-orthogonality ($^\circ$)	Maximum non-orthogonality ($^\circ$)	Maximum skewness
Inner tube	25.63	9.03	57.73	2.43
Outer tube	18.16	5.39	46.08	1.02
Water	30.63	6.28	57.12	0.93

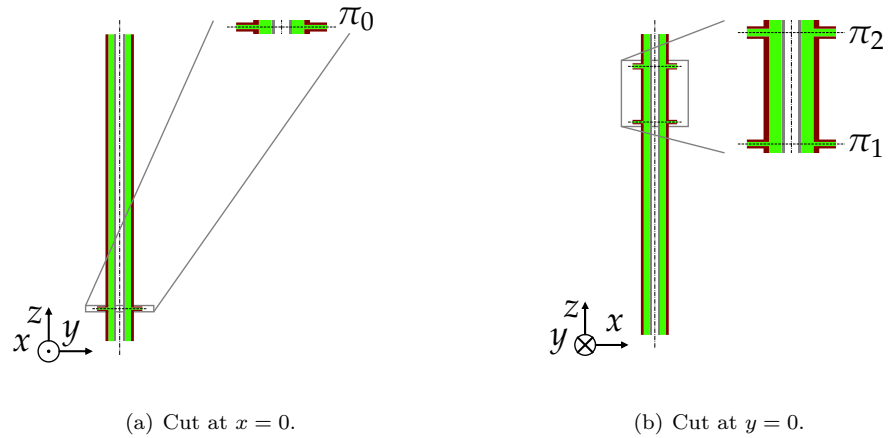


Figure 3.13: Meshed regions. LES. Green: water. Gray: inner tube. Red: outer tube. The outer tube is 1.08 m long. It goes from $z = 0.036$ m to $z = 1.116$ m. The xy -midplane of the cold inlets π_0 is at $z = 0.15$ m. The xy -midplane of the hot inlets π_1 is at $z = 0.8$ m. The xy -midplane of the outlets π_2 is at $z = 1$ m. $R_{ii} = 12.5$ mm. $R_{io} = 17.5$ mm. $R_{oi} = 40$ mm. $R_{oo} = 50$ mm.

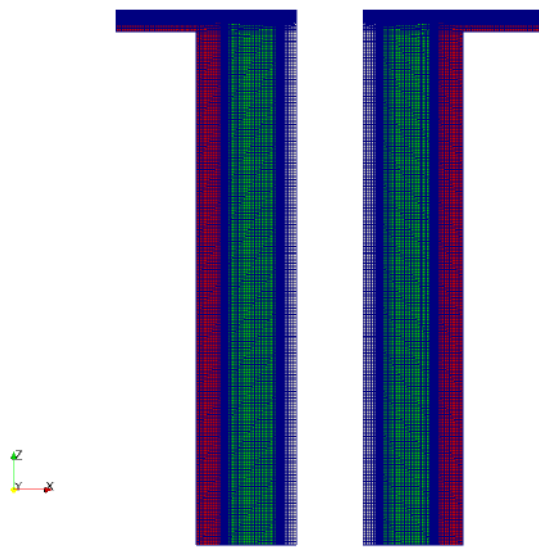
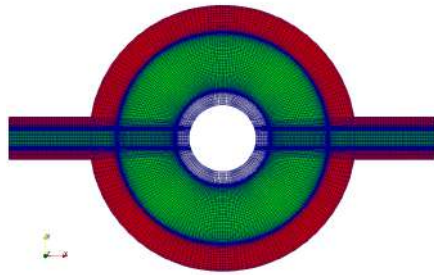
(a) Cut at $y = 0$. $0.6\text{m} \leq z \leq 0.8\text{m}$.(b) Cut at $z = 0.8\text{m}$.

Figure 3.14: Optimal LES mesh. Green: water. Gray: inner tube. Red: outer tube.

Table 3.7: Inlet boundary conditions. Optimal LES mesh. \tilde{T}^* and $\tilde{\mathbf{u}}^*$ represent temperature and velocity averaged over each inlet cross section, respectively. The coordinate system is defined in Fig. 3.13. Nominal values are reported in Bergaglio *et al.* (2018a).

Inlet	$\tilde{\mathbf{u}}^*$ (kg s^{-1})	\tilde{T}^* (K)	Re (-)	Pr (-)
Hot inlet at $x = -0.08$ m	(12.21, 0, 0)	549.74	728 687	0.85
Hot inlet at $x = 0.08$ m	(-12.33, 0, 0)	549.47	735 550	0.85
Cold inlet at $y = -0.08$ m	(0, 0.83, 0)	334.16	13 263	2.93
Cold inlet at $y = 0.08$ m	(0, -0.80, 0)	334.15	12 892	2.93

3.6.6 Boundary and initial conditions

The LES boundary conditions are taken from Case 1 (see Table 3.3). Theoretically, 0.4 kg s^{-1} of water at 549 K and 0.035 kg s^{-1} of water at 333 K flow through each hot and cold inlet, respectively. Notwithstanding, the measured boundary conditions, which are listed in Table 3.7, deviate from such nominal values. The experimental boundary conditions in the above table are time-averaged. Applying measured boundary conditions weakens the azimuthal symmetry in the simulation results.

The velocity inlet boundary condition should be selected carefully because it can impact on the accuracy of the LES results. Following Tabor and Baba-Ahmadi (2010) and Dhamankar *et al.* (2015), (1) the ideal inlet velocity is self-similar (fully developed flow); (2) it is independent of spatial discretization and grid type; (3) it matches a realistic power spectrum; (4) it does not introduce fictitious periodicities or other unphysical features; and (5) it is calculated with minimal computational overhead. In the current research, inflow data are generated using internal mapping: velocity is taken from a plane downstream of the inlet, scaled to match the target inlet velocity in Table 3.7 as a mean, and mapped back to the inlet. The sampling plane is situated 25.5 mm downstream of the inlet; in other terms, at $L_p/D_p = 3.4$, where D_p is the pipe diameter and L_p is the distance between sampling plane and inlet. Internal mapping creates high-quality turbulence with minimal computational overhead (Tabor and Baba-Ahmadi (2010); Dhamankar *et al.* (2015)). Westin *et al.* (2008), Odemark *et al.* (2009), and Kuczaj and Komen (2010) stress that turbulence is mainly created by flow mixing; consequently, analogously to Gauder *et al.* (2016) and Selvam *et al.* (2017), in the current research no (random) flow perturbations are imposed at the inlets.

A no-slip boundary condition is prescribed at water-steel interfaces, bottom, and top. A zero velocity gradient is assumed at the outlets. A user-selected velocity value is imposed if reverse flow is encountered.

Thermal fatigue due to cyclic change in fluid temperature is essentially a CHT problem: temperature fluctuations are affected by different solid-fluid combinations (Tinoco (2013)). CHT is computed at water-steel interfaces using Eq. (3.22). The

innermost and outermost walls, top, and bottom are taken to be adiabatic. The outlets are also adiabatic, but a user-selected temperature value is imposed if reverse flow is encountered.

Pressure is set to 7.2 MPa at the outlets. At the inlets, water-steel interfaces, top, and bottom, the pressure gradient is made consistent with the velocity boundary condition. By doing so, buoyancy is taken into account.

Concerning initial conditions, first, the precursor $k - \varepsilon$ simulation from Subsection 3.6.3 is carried out on a coarse mesh, to determine the optimal mesh size. Second, an LES is conducted on a mildly refined mesh (Thiele (2015); Bergaglio *et al.* (2017)). Velocities and temperature are initialized from the results of the $k - \varepsilon$ simulation. Finally, the LES under study is performed on the optimal mesh. Velocities and temperature are initialized from the results of the LES on a mildly refined mesh. Temperatures in the mixing region are initialized from spatial interpolation of time-averaged experimental temperatures.

3.6.7 Linear elastic analysis and fatigue damage assessment

After completion of the LES on the optimal mesh, an elastic finite element analysis of the inner tube is conducted to compute stresses caused by cyclic changes in water temperature and to assess fatigue damage. To this end, the Cauchy momentum equation is solved:

$$\rho_S \frac{\partial^2 \mathbf{s}}{\partial t^2} = \nabla \cdot \boldsymbol{\sigma} + \rho_S \mathbf{g}, \quad (3.32)$$

Here, $\partial^2 \mathbf{s} / \partial t^2 \approx (\mathbf{s} - 2\mathbf{s}^0 + \mathbf{s}^{00}) / (\Delta t)^2$. Linear elasticity is invoked; correspondingly, stresses are calculated from Eq. (3.33):

$$\boldsymbol{\sigma} = \tilde{\lambda}_S (\nabla \cdot \mathbf{s}) \mathbf{I} + 2\tilde{\mu}_S \tilde{\mathbf{S}}(\mathbf{s}) - (3\tilde{\lambda}_S + 2\tilde{\mu}_S) \tilde{\alpha}_S (T_S - T_{\text{ref}}) \mathbf{I}. \quad (3.33)$$

Here, $\tilde{\lambda}_S$ and $\tilde{\mu}_S$ are the first and second Lamé parameters, while $\tilde{\alpha}_S$ denotes the mean thermal expansion coefficient between temperatures T_{ref} and T_S . Consistently with Subsection 3.6.3, 316LN stainless steel properties are temperature polynomials supplied with the MPDB software (Software Inc. (2015)). No displacement is allowed at the bottom surface (that is, $\mathbf{s} = \mathbf{0}$), while the top surface is constrained in the axial direction (that is, $s_z = 0$). LES temperatures replace T_S in Eq. (3.33). LES pressure is applied as boundary condition on the inner surface. No displacement is set as initial condition; i.e., $\mathbf{s}^0 = \mathbf{s}^{00} = \mathbf{0}$ at start time t_0 . Eq. (3.32) is solved using the finite-element library FEniCS (Logg *et al.* (2012); Alnæs *et al.* (2015)), version 2017.2. The FEA mesh is coarser than the mesh in Fig. 3.14: one of the major goals of this research is to establish a methodology for assessing high-cycle fatigue damage from LES results, so the FEA mesh will conform to the LES one in future work.

After computation of the elastic stresses, a rainflow cycle-counting technique (Energy (2016)) decomposes each nodal stress time series in the mixing region into

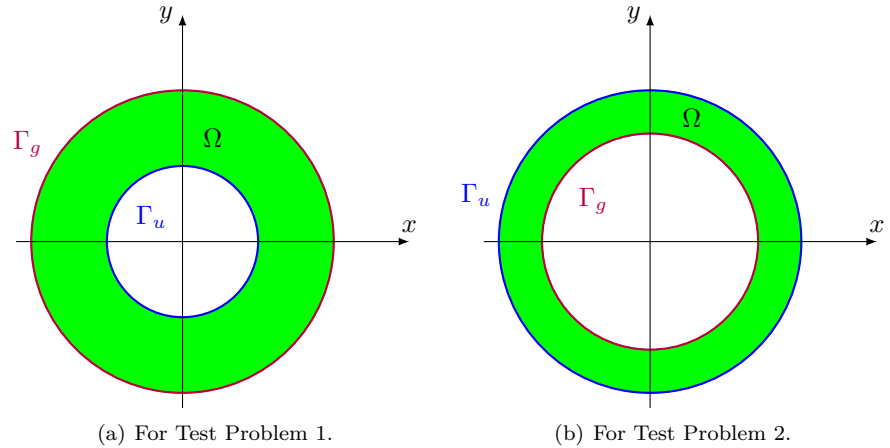


Figure 3.15: IHCP domains.

a sequence of load reversals (peaks and troughs). This technique returns the number of load cycles and their respective amplitudes. When picking relative extreme stress conditions (ASME (2015b)), an approach based on signed stress intensity (Green and Ferrari (2016)) can overcome some limitations of the approach based on stress intensity from the ASME Code; for example, it allows to discern whether compression or tension prevails at a given extremum, without adding fake extrema, and yet it conforms to ASME (2015b); hence, it stems from the maximum shear stress principle. A uniaxial S - N curve (Wöhler curve, or fatigue curve) for austenitic steel in air (ASME (2015a)) allows to compute the number of cycles to failure. Analogously to Wilson *et al.* (2016), Miner's rule (linear cumulative fatigue damage) is applied to compute a CUF for each node in the mixing region. Damage at stress amplitudes below the fatigue limit is estimated by extrapolating the fatigue curve (Schijve (2009)).

A time-step independence study is conducted. The calculated stresses and reduced stress history are verified by comparison with results from Radu *et al.* (2008) and Green and Ferrari (2016), respectively.

3.7 IHCP

Two cases are examined: Test Problems 1 and 2. Their space domains are shown in Fig. 3.15. The respective inverse problems are solved by setting redundant boundary conditions on Γ_g : in the inverse problem, temperatures at time $t = 0$, temperatures on Γ_g , and heat fluxes on Γ_g (that is, $q_g(\mathbf{x}, t)$) are supposed to be known, while temperatures on Γ_u and heat fluxes on Γ_u (that is, $q_u(\mathbf{x}, t)$) are supposed to be unknown. The inverse problem is equivalent to the minimization of

the objective function in Eq. (3.34):

$$\mathcal{J}(q_{u,k}) = \underbrace{\frac{1}{2} \int_0^{t_f} \int_{\Gamma_g} (T_k - Y^\xi)^2 d\Gamma dt}_{\mathcal{J}_A} + \underbrace{\frac{\gamma_k}{2} \int_0^{t_f} \int_{\Gamma_u} (q_{u,k})^2 d\Gamma dt}_{\mathcal{J}_B}. \quad (3.34)$$

Term \mathcal{J}_A is a conventional least-squares objective function, whereas term \mathcal{J}_B is a zeroth-order stabilizing functional. Constant γ_k is a regularization parameter. Temperature $Y(\mathbf{x}, t)$ is found from a forward problem:

$$\begin{cases} \rho c(Y) \frac{\partial Y}{\partial t} = \nabla \cdot (\lambda(Y) \nabla Y) & (\mathbf{x}, t) \in (\Omega, \mathcal{T}) & (3.35a) \\ Y(\mathbf{x}, 0) = \tilde{Y} & \mathbf{x} \in \Omega & (3.35b) \\ \lambda \nabla Y \cdot \mathbf{n} = -\hat{h}(\theta) (Y - Y_\infty) & (\mathbf{x}, t) \in (\Gamma_g, \mathcal{T}) & (3.35c) \\ Y = Y_u & (\mathbf{x}, t) \in (\Gamma_u, \mathcal{T}). & (3.35d) \end{cases}$$

t is such that $0 \leq t \leq t_{\max}$, where $t_{\max} > t_f$. Gaussian noise is added to Y ; hence, $Y^\xi = Y + \xi X$, X being a normally distributed variable with mean $\hat{\mu}$ and standard deviation $\hat{\sigma}$. $\hat{\mu} = 0\text{K}$ and $\hat{\sigma} = 1\text{K}$ in both test problems (see Subsections 4.6.1 and 4.6.2). Multiplier ξ represents the standard deviation of the Gaussian noise. This test parameter is examined in Subsection 4.6.1. Different formulas for \mathcal{J}_B can be found in literature, such as first-order Tikhonov regularization (Bozzoli *et al.* (2014); Frackowiak *et al.* (2015)), second-order Tikhonov regularization (Dennis and Dulikravich (2012)), and penalization with a weighted l^ψ -norm of the coefficients of T with respect to a specific orthonormal basis in a Hilbert space, where $1 \leq \psi \leq 2$ (Daubechies *et al.* (2004)).

$T_k := T(\mathbf{x}, t; q_{u,k})$ from Eq. (3.34) solves the primal problem in Eqs. (3.36a)-(3.36d) at iteration k (with subscript k omitted):

$$\begin{cases} \rho c(T) \frac{\partial T}{\partial t} = \nabla \cdot (\lambda(T) \nabla T) & (\mathbf{x}, t) \in (\Omega, \mathcal{T}) & (3.36a) \\ T(\mathbf{x}, 0) = \tilde{Y}^\xi & \mathbf{x} \in \Omega & (3.36b) \\ \lambda(T) \nabla T \cdot \mathbf{n} = q_g(\mathbf{x}, t) & (\mathbf{x}, t) \in (\Gamma_g, \mathcal{T}) & (3.36c) \\ \lambda(T) \nabla T \cdot \mathbf{n} = q_u(\mathbf{x}, t) & (\mathbf{x}, t) \in (\Gamma_u, \mathcal{T}). & (3.36d) \end{cases}$$

The gradient of $\mathcal{J}(q_{u,k})$ is given by

$$\mathcal{J}'(q_{u,k}) = \phi_k + \gamma_k q_{u,k}, \quad (3.37)$$

where $\phi_k := \phi(\mathbf{x}, t; q_{u,k})$ solves the dual problem in Eqs. (3.38a)-(3.38d) at iteration k (with subscript k omitted):

$$\begin{cases} \rho c(T) \frac{\partial \phi}{\partial t} = -\lambda(T) \nabla^2 \phi & (\mathbf{x}, t) \in (\Omega, \mathcal{T}) & (3.38a) \\ \phi(\mathbf{x}, t_{\max}) = 0 & \mathbf{x} \in \Omega & (3.38b) \\ \lambda(T) \nabla \phi \cdot \mathbf{n} = T(\mathbf{x}, t; q_u) - Y^\xi & (\mathbf{x}, t) \in (\Gamma_g, \mathcal{T}) & (3.38c) \\ \lambda(T) \nabla \phi \cdot \mathbf{n} = 0 & (\mathbf{x}, t) \in (\Gamma_u, \mathcal{T}). & (3.38d) \end{cases}$$

Here, $Y^\xi := Y^\xi(\mathbf{x}, t)$. The dual problem under study is linear (as, for example, highlighted by Abou Khachfe and Jarny (2000)); moreover, it is adjoint to the sensitivity problem in Eqs. (3.42a)-(3.42c). $\mathcal{J}(q_u)$ is minimized by applying the extensively used CGM.

Conjugation coefficient β_k is expressed as

$$\beta_k = \begin{cases} 0 & \text{if } k = 0 \\ \max(0, \beta^{PR}) & \text{otherwise,} \end{cases} \quad (3.39a)$$

$$(3.39b)$$

β^{PR} being the conjugation coefficient from the Polak-Ribière variant of the CGM

$$\beta^{PR} = \frac{\int_0^{t_f} \int_{\Gamma_u} \mathcal{J}'(q_{u,k}) (\mathcal{J}'(q_{u,k}) - \mathcal{J}'(q_{u,k-1})) \, d\Gamma \, dt}{\int_0^{t_f} \int_{\Gamma_u} (\mathcal{J}'(q_{u,k-1}))^2 \, d\Gamma \, dt}. \quad (3.40)$$

The optimal step length or size $\hat{\alpha}_k$ is expressed as

$$\hat{\alpha}_k = - \frac{\int_0^{t_f} \int_{\Gamma_g} (T_k - Y^\xi) \hat{\theta}_k \, d\Gamma \, dt + \gamma_{k+1} \int_0^{t_f} \int_{\Gamma_u} \hat{p}_k q_{u,k} \, d\Gamma \, dt}{\int_0^{t_f} \int_{\Gamma_g} \hat{\theta}_k^2 \, d\Gamma \, dt + \gamma_{k+1} \int_0^{t_f} \int_{\Gamma_u} \hat{p}_k^2 \, d\Gamma \, dt}, \quad (3.41)$$

where $\hat{\theta}_k := \hat{\theta}(\mathbf{x}, t; q_{u,k}, \hat{p}_k)$ solves the sensitivity problem in Eqs. (3.42a)-(3.42d) at iteration k (with subscript k omitted):

$$\begin{cases} \rho \frac{\partial (c(T) \hat{\theta})}{\partial t} = \nabla^2 (\lambda(T) \hat{\theta}) & (\mathbf{x}, t) \in (\Omega, \mathcal{T}) & (3.42a) \end{cases}$$

$$\begin{cases} \hat{\theta}(\mathbf{x}, 0; q_u, \hat{p}) = 0 & \mathbf{x} \in \Omega & (3.42b) \end{cases}$$

$$\begin{cases} \nabla (\lambda(T) \hat{\theta}) \cdot \mathbf{n} = 0 & (\mathbf{x}, t) \in (\Gamma_g, \mathcal{T}) & (3.42c) \end{cases}$$

$$\begin{cases} \nabla (\lambda(T) \hat{\theta}) \cdot \mathbf{n} = \hat{p}(\mathbf{x}, t) & (\mathbf{x}, t) \in (\Gamma_u, \mathcal{T}). & (3.42d) \end{cases}$$

Consequently, the sensitivity problem is linear, as, for example, highlighted by Abou Khachfe and Jarny (2000). Δq_u in Eq. (3.42d) is renamed to \hat{p} . Eq. (3.41) is derived in Appendix B of Bergagio *et al.* (2018b).

Several conjugation coefficients and conjugate search direction (descent direction) methods can be adopted; their efficiencies are compared, for example, in

Belmiloudi and Mahé (2014) and Nocedal and Wright (2006). Eq. (3.41) holds exactly for a quadratic model of the objective function. In nonlinear IHCPs, convergence is guaranteed by computing optimal step size $\hat{\alpha}_k$ in other ways, such as Fibonacci search, golden section search, and limited-memory quasi-Newton methods (Nocedal and Wright (2006)).

Conjugate search direction \hat{p}_k in Eq. (3.41) is given as follows:

$$\hat{p}_k = \begin{cases} -\mathcal{J}'(q_{u,k}) & \text{if } k = 0 \\ -\mathcal{J}'(q_{u,k}) + \beta_k \hat{p}_{k-1} & \text{otherwise.} \end{cases} \quad (3.43a)$$

$$(3.43b)$$

The forward, primal, dual, and sensitivity problems are solved using the open-source finite-element library FEniCS (Logg *et al.* (2012); Alnæs *et al.* (2015)). Versions 2016.2 (tetrahedral cells) and 2017.2 (hexahedral cells) of this package have been tested; however, results from the latter version are not reported here. Given that the forward and primal problems are nonlinear, the Picard iteration scheme is applied to solve them. The time discretization follows the Crank-Nicolson scheme. In order to increase numerical accuracy, the time step is computed as a fraction of \tilde{h}_{\min}^2/a , comparably to critical time steps of conditionally stable time integrators (Zienkiewicz *et al.* (2005)). Here, a denotes the mean thermal diffusivity $\lambda/\rho c$ at $t = 0$, while \tilde{h}_{\min} is the minimum cell size. If high frequencies are to be studied, their periods should be considered when evaluating proper time steps. Notwithstanding, both time-step and mesh independence studies ought to be performed, particularly in highly nonlinear problems. For example, a mesh independence study is performed in Subsection 4.6.2.

Regularization parameter γ compromises between filtering out the undesired noise ξ and matching the noise-perturbed data Y^ξ , in an effort to reach the solution to a perturbation-free IHCP: a large γ , or oversmoothing, reduces the calculation time and the fluctuations of solution T , at the expense of its accuracy, whereas a small γ , or undersmoothing, provides appropriate data fitting, but cannot mitigate the sensitivity of solution T to noise. Here, γ is determined using the fixed-point technique (Viloché Bazán (2008)) abridged by Bozzoli *et al.* (2014):

$$\gamma_{k+1} = \frac{\int_0^{t_f} \int_{\Gamma_g} (T_k - Y^\xi)^2 d\Gamma dt}{\int_0^{t_f} \int_{\Gamma_u} (q_{u,k})^2 d\Gamma dt}. \quad (3.44)$$

Alternative heuristic algorithms performing the same task are detailed in Hansen and O'Leary (1993) (L-curve method), Heng *et al.* (2010) (modified L-curve method), Krawczyk-Stańdo and Rudnicki (2007) (U-curve method), and Niknam Shahrak *et al.* (2013) (modified U-curve method).

Algorithm 1 combines the equations in this section. The stopping criterion in Algorithm 1 is examined in Section 4.6.1.

Algorithm 1: Final algorithm.

- 1 Solve the forward problem in Eqs. (3.35a) - (3.35d) to find Y and q_g ;
 - 2 add Gaussian noise to Y and \tilde{Y} to find Y^ξ and \tilde{Y}^ξ , respectively;
 - 3 calculate q_g as $q_g = \lambda (Y^\xi) \nabla Y^\xi \cdot \mathbf{n}$;
 - 4 guess $q_{u,0}(\mathbf{x}, t)$; i.e., the heat flux on Γ_u at iteration $k = 0$;
 - 5 guess γ_0 ;
 - 6 **do**
 - 7 solve the primal problem in Eqs. (3.36a) - (3.36d) forward in time to find T_k ;
 - 8 solve the dual problem in Eqs. (3.38a) - (3.38d) backward in time to find ϕ_k ;
 - 9 compute $\mathcal{J}'(q_{u,k})$ from Eq. (3.37);
 - 10 compute β_k from Eqs. (3.39a) - (3.39b);
 - 11 compute \hat{p}_k from Eqs. (3.43a) - (3.43b);
 - 12 solve the sensitivity problem in Eqs. (3.42a) - (3.42c) forward in time to find $\hat{\theta}_k$;
 - 13 compute γ_{k+1} from Eq. (3.44);
 - 14 compute $\hat{\alpha}_k$ from Eq. (3.41);
 - 15 compute $q_{u,k+1}$ as

$$q_{u,k+1} = q_{u,k} + \hat{\alpha}_k \hat{p}_k; \quad (3.45)$$
 - 16 increase k by 1;
 - while** $\int_0^{t_{\max}} \int_{\Gamma_u} (\hat{\alpha}_k \hat{p}_k)^2 d\Gamma dt$ is greater than a specified tolerance; i.e., the stopping criterion is not satisfied;
-

Chapter 4

Results

4.1 Inverse- and low-pass filtering

Here, low-pass filtered inner-surface temperatures are illustrated by three examples:

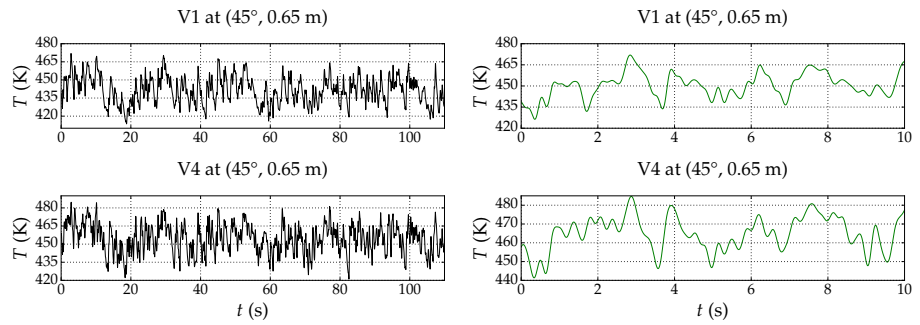
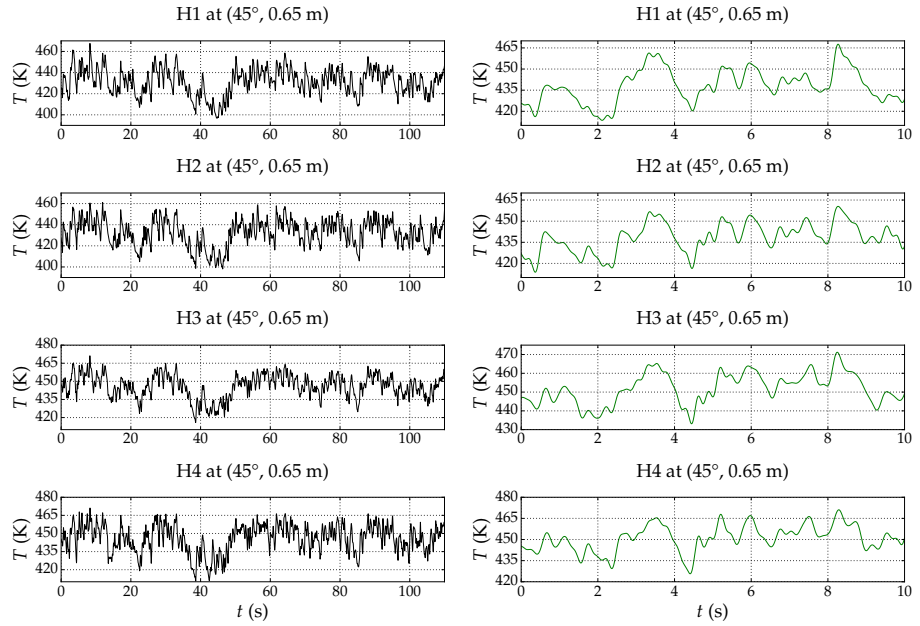
1. same level z_f and angle θ_f , with tolerances of 1.20 cm and 7.96° , respectively (as shown in Fig. 4.1);
2. same channel and z_f (as shown in Fig. 4.2); and
3. same channel and θ_f (as shown in Fig. 4.3).

Only Case 1 is examined (see Table 3.3). The connection between velocities at the hot inlets and low-pass filtered inner-surface temperatures from thermocouple $H2$ at a representative (θ_f, z_f) is described in Bergagio and Anglart (2017).

Gains G and differential spread variables Δ from Subsection 3.3.1 are presented in Table 4.1.

Inner-surface temperatures from the right and left thermocouple disc are respectively shown in Figs. 4.1(a) and 4.1(b), for the same case and (θ_f, z_f) . Time series in Fig. 4.1(a) were sampled approximately simultaneously. The normalized cross-correlations between the inner-surface temperatures in Fig. 4.1(a) vary from 0.90 to 0.95, which reveals good correlation. The normalized cross-correlation between the inner-surface temperatures in Fig. 4.1(b) equals 0.86, which is deemed acceptable. Moreover, the time series in Figs. 4.1(a) and 4.1(b) correlate in terms of ranges (between 55.33 and 70.89 K), standard deviations (between 9.64 and 12.34 K), mean values (between 431.61 and 454.52 K), and frequencies – see Figs. 4.13 and 4.14. Thus, temperatures from the same (θ_f, z_f) can be unified in one parameter, expressive of mixing intensity. Furthermore, the above consistency underpins experimental repeatability.

Fig. 4.2 highlights some discrepancy between temperatures at 180° and those at 360° , in terms of standard deviation (3.24 against 12.20 K), mean (356.04 against 419.09 K), and frequencies. Concerning range, temperatures at 180° , 225° , and 270°

Figure 4.1: Inner-surface temperatures in Case 1 at $(45^\circ, 0.65 \text{ m})$.

cover less than 30 K (19.02, 29.33, and 24.16 K, respectively), whereas temperatures at 360°, 45°, and 90° span more than 60 K (65.22, 62.93, and 70.32 K, respectively). Concerning frequencies, the time series at 180°, 225°, and 270° show sudden temperature spikes, whereas the time series at 360°, 45°, and 90° exhibit more periodic peaks and troughs. In terms of mean, standard deviation, and prominent frequencies, the time series at 135° and 315° transition from incipient mixing (at 180°, 225°, and 270°) to more extensive mixing (at 360°, 45°, and 90°). The mismatch between phenomena occurring 180° apart is commented upon later.

In Fig. 4.3, temperatures at 0.63 m exhibit unexpected peaks, similar to those from set (180°, 225°, 270°) – see Fig. 4.2. Their range, mean value, and standard deviation, which equal 27.63 K, 344.61 K, and 2.77 K, respectively, are analogous to those from the above set. Standard deviation appears higher at 0.65 m than at 0.67 m, 0.70 m, and 0.72 m. Ranges follow a similar pattern. Moreover, although fast oscillations appear predominant above 0.65 m, it is clear that mixing can be better studied through spectral analysis. This analysis ought to handle nonlinear, non-stationary time series, and to process intermittent signals, such as those exemplifying incipient mixing.

Figures exemplifying inner-surface temperatures in Cases 6, 8, and 10 are described in Bergagio and Anglart (2017). In essence, thermal stratification is expected to reduce mixing in Case 1 more than in Case 6, as it hampers the downward penetration of the hot streams into the annular region. By contrast, mixing seems more intense in Case 1 than in Case 8 since, in the former, higher mass fluxes of the hot streams, which strengthen mixing farther down in the annulus, counteract stratification.

The highest gains G and highest, lowest, and mean differential spreads Δ for inner-surface temperatures sampled at $f_{S,DAS} = 1000$ Hz are listed in Table 4.1. G expresses the difference between ranges at 1000 Hz and at 100 Hz, whereas Δ quantifies the difference between variances at 1000 Hz and at 100 Hz. In contrast to the highest gains, differential spreads appear very sensitive to changes in sampling rate: variances are sensibly higher at 100 Hz than at 1000 Hz. This incongruity happens to broaden with increasing difference between Reynolds numbers Re_H and Re_C ; in other terms, in Cases 1 and 2. Hence, sampling test-section temperatures at 1000 Hz in Cases 1 and 2 seems justified.

4.2 Mixing intensity

Figs. 4.4 depicts the highest, mean, and lowest normalized inner-surface temperatures $T_{f,d}^*$ (see Eq. (3.10)) with respect to ζ , a normalized z -coordinate defined by $\zeta = (z_H - z^*)/D_{hyd}$. The hot inlets are located at axial level z_H , while $D_{hyd} = 2(R_{oi} - R_{io}) = 45$ mm is the hydraulic diameter of the annular region. Thus, $\zeta = 2.22$ if $z^* = 0.70$ m, whereas $\zeta = 3.33$ if $z^* = 0.65$ m. Measurement position (θ^*, z^*) from Section 3.4 includes z^* .

Mixing estimator $\bar{\sigma}$ (see Section 3.4) is given in Figs. 4.5, 4.6, 4.7, and 4.8. In

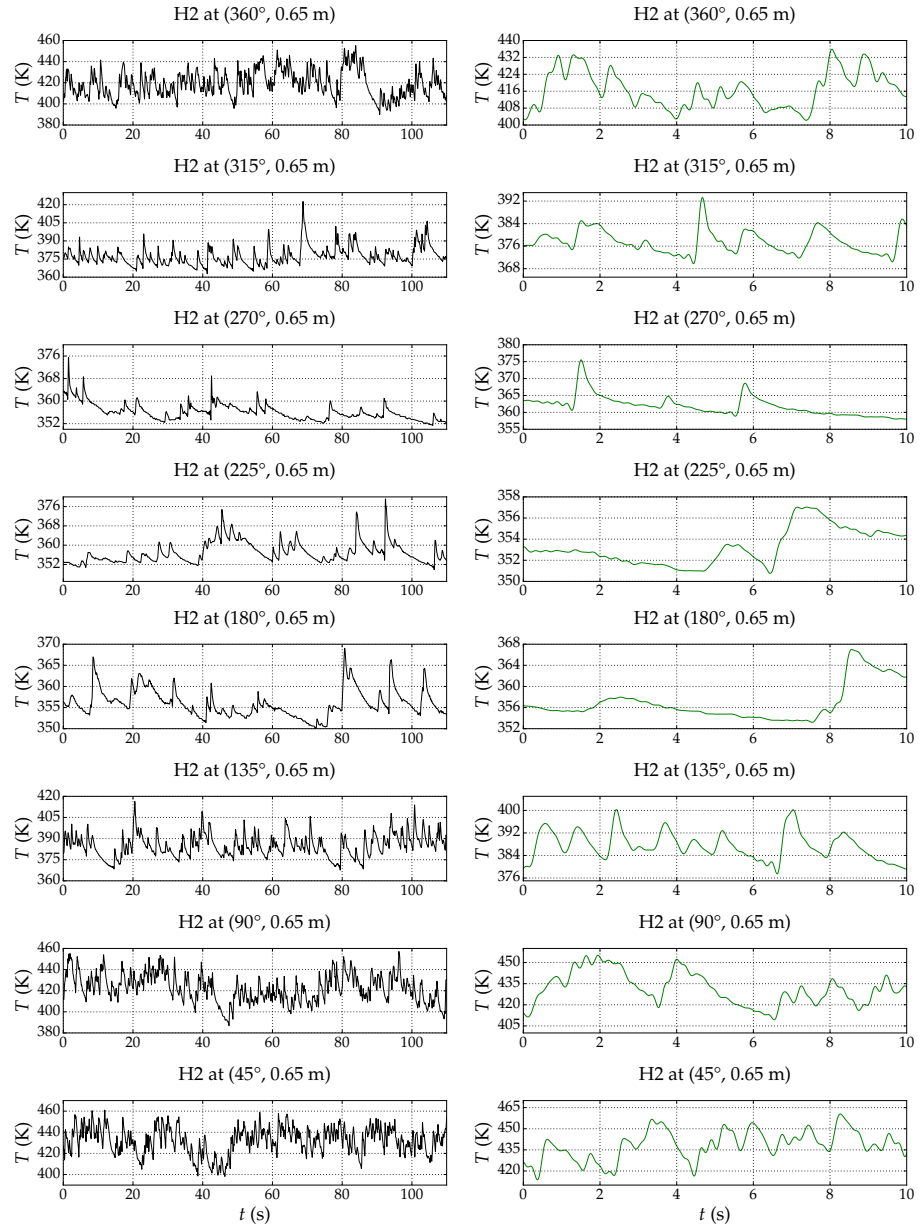
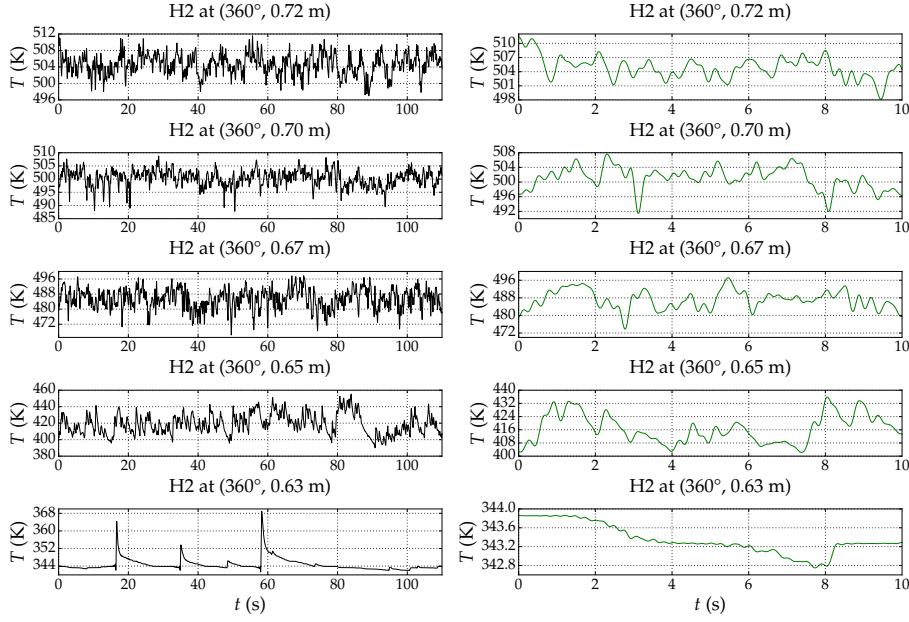


Figure 4.2: Inner-surface temperatures at 0.65 m in Case 1, from thermocouple $H2$.

Figure 4.3: Inner-surface temperatures at 360° in Case 1, from thermocouple $H2$.Table 4.1: Highest gains G and lowest, highest, and mean differential spreads Δ at a sampling rate of 1000 Hz.

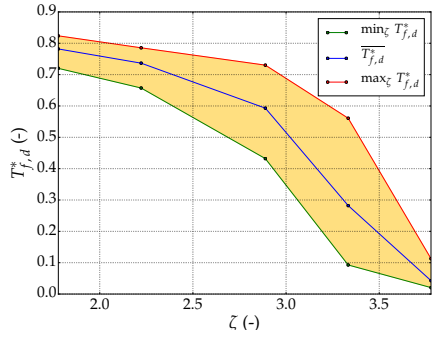
Case no., or l	$\max_l G$ (K)	$\min_l \Delta$ (-)	$\max_l \Delta$ (-)	$\bar{\Delta}$ (-)
1	0.86	-44.73%	7.70%	-6.81%
2	0.79	-40.13%	20.25%	-9.58%
3	0.91	-16.83%	5.85%	-3.11%
4	0.88	-18.62%	4.32%	-1.94%

these figures, for ease of notation, θ and z replace θ^* and z^* , respectively. Here, two regions are highlighted: $R_1 = \{(\theta, z) : 135^\circ \leq \theta \leq 225^\circ\}$ and $R_2 = \{(\theta, z) : (315^\circ \leq \theta \leq 360^\circ) \cup (0^\circ < \theta \leq 45^\circ)\}$; therefore, R_1 and R_2 incorporate the hot inlets and the neighbor measurement positions in the azimuthal direction. The cold inlets are ignored because much less water flows through them than through the hot inlets, and because they are believed not to affect mixing, which happens high above their axis ($z_C = 0.15$ m): Fig. 4.4 shows that temperature oscillations become noticeable at $\zeta = 4.44$, or $z = 0.60$ m, as stated in Section 4.1. Moreover, Fig. 4.4 suggests that, at the z -coordinate with the widest range of normalized inner-surface temperatures, the normalized adiabatic mixing temperature T_{mix}^* in Tables 3.3 and 3.4 is always higher than $\max_{\zeta} T_{f,d}^*$: at that z -coordinate, $\max T_{f,d}^*$ reaches 0.81 in Case 8 and falls even lower in the other cases. The z -coordinate at which the range of normalized inner-surface temperatures is widest often equals the z -coordinate at which the mixing estimator is highest (see Figs. 4.5-4.8). Consequently, T_{mix}^* characterizes zones of low variance, greatly above those exhibiting highly non-uniform, strong mixing.

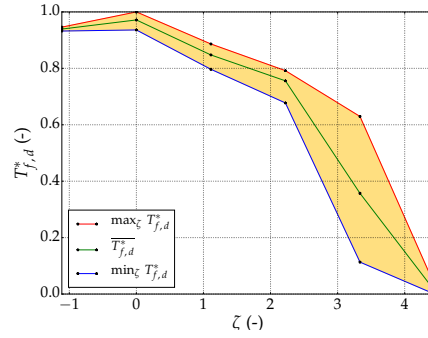
Data in Figs. 4.4(a) (Case 1) and 4.4(b) (Case 5) can be combined, since Cases 1 and 5 share the same boundary conditions and the highest, mean, and lowest normalized inner-surface temperatures at $\zeta = 2.22$ (i.e., $z = 0.70$ m) and $\zeta = 3.33$ (i.e., $z = 0.65$ m) for Case 1 echo those at the same ζ -coordinates for Case 5. In detail, the range of normalized inner-surface temperatures equals 0.11 at $\zeta = 2.22$ and 0.52 at $\zeta = 3.33$ in Case 5; similarly, it equals 0.13 at $\zeta = 2.22$ and 0.47 at $\zeta = 3.33$ in Case 1. The above ranges suggest good experimental repeatability.

Concerning the mixing estimator in Cases 1 and 5, Figs. 4.5 and 4.6 report highly non-uniform mixing at $z = 0.65$ m in region R_2 (namely, at $(360^\circ, 0.65$ m) and $(45^\circ, 0.65$ m)), in contrast to more uniform mixing at the same z -coordinate in region R_1 . In Case 5, mixing estimator is also low at the nearest neighbors of point $(180^\circ, 0.65$ m) (i.e., between 135° and 225° , at $z = 0.60$ m and $z = 0.70$ m); therefore, it seems that mixing strength in region R_1 does not mirror that in R_2 . This might be due to the large axial distance between neighbor measurement positions in Case 5. In Case 1, this gap is reduced, which partially reinstates the expected symmetry in mixing strength between R_1 and R_2 , as relevant temperature oscillations also appear at $(225^\circ, 0.67$ m) – see Fig. 4.5. This slight shift towards higher axial measurement positions could be ascribed to many factors, including (1) asymmetries in the unheated test section; (2) deformation of the test section, from uneven insulation or heating; and (3) dissimilar flow rates and temperatures at each inlet pair. These factors may also explain the mismatch between phenomena happening 180° apart (see Section 4.1).

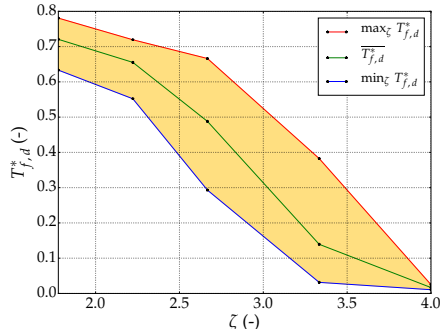
In order to assess how flow rates through the hot inlets change mixing, Cases 2 and 9 are examined, because all their boundary conditions but flow rates through the hot inlets are taken from Cases 1 and 5. Figs. 4.4(c) and 4.4(d) show that the ranges of normalized inner-surface temperatures are widest at $z = 0.68$ m in Case 2 and at $z = 0.70$ m in Case 9. In accordance with these remarks, Figs. 4.7 and 4.8



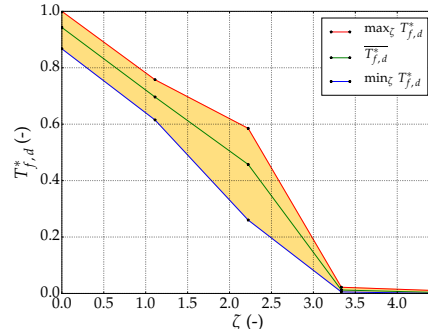
(a) In Case 1. Here, $T_C = 333$ K, $T_H = 549$ K, $\dot{m}_C = 0.07$ kg s $^{-1}$, and $\dot{m}_H = 0.8$ kg s $^{-1}$.



(b) In Case 5. Same boundary conditions as in Case 1.



(c) In Case 2. Here, $T_C = 333$ K, $T_H = 549$ K, $\dot{m}_C = 0.07$ kg s $^{-1}$, and $\dot{m}_H = 0.6$ kg s $^{-1}$.



(d) In Case 9. Here, $T_C = 333$ K, $T_H = 549$ K, $\dot{m}_C = 0.07$ kg s $^{-1}$, and $\dot{m}_H = 0.4$ kg s $^{-1}$.

Figure 4.4: Axial distribution of the highest, mean, and lowest values of the normalized detrended inner-surface temperatures $T_{f,d}^*$. Amber: area enclosed by the lower and upper envelopes. Here, $\overline{T_{f,d}^*}$ represents $T_{f,d}^*$ averaged over time and angles.

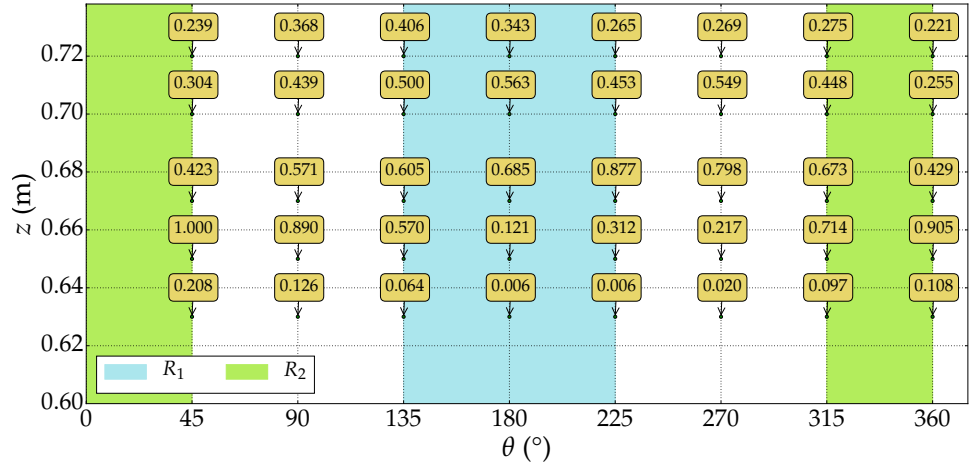


Figure 4.5: Mixing estimator in Case 1. It is calculated as the mean standard deviation of the normalized detrended inner-surface temperatures $T_{f,d}^*$ after outlier removal, for each measurement position. Values are normalized to the highest mixing estimator.

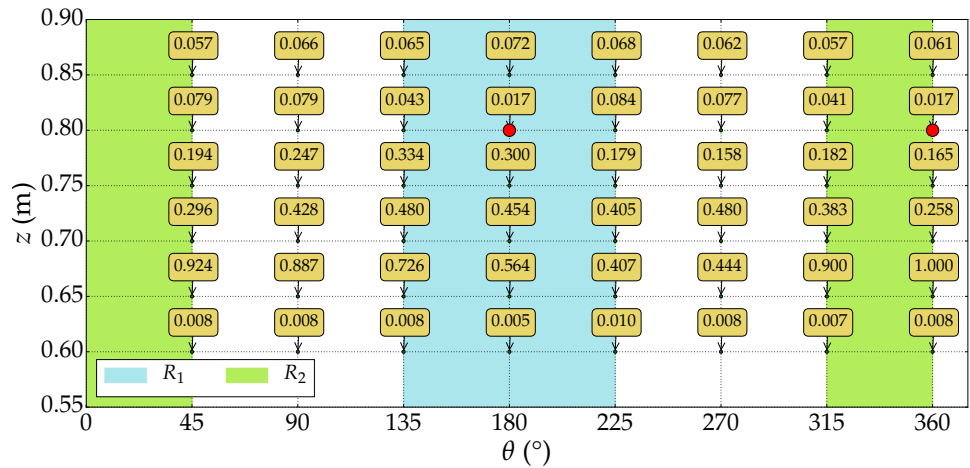


Figure 4.6: Mixing estimator in Case 5. Red dots mark the axes of the hot inlets.

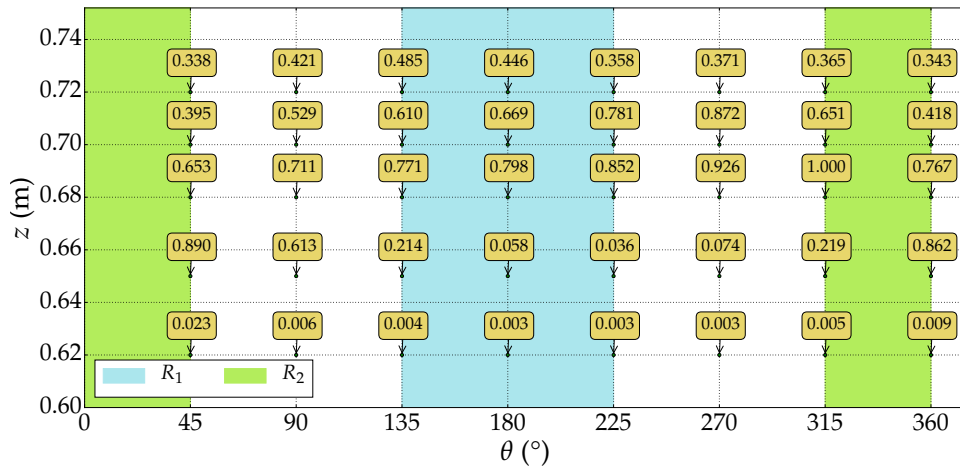


Figure 4.7: Mixing estimator in Case 2.

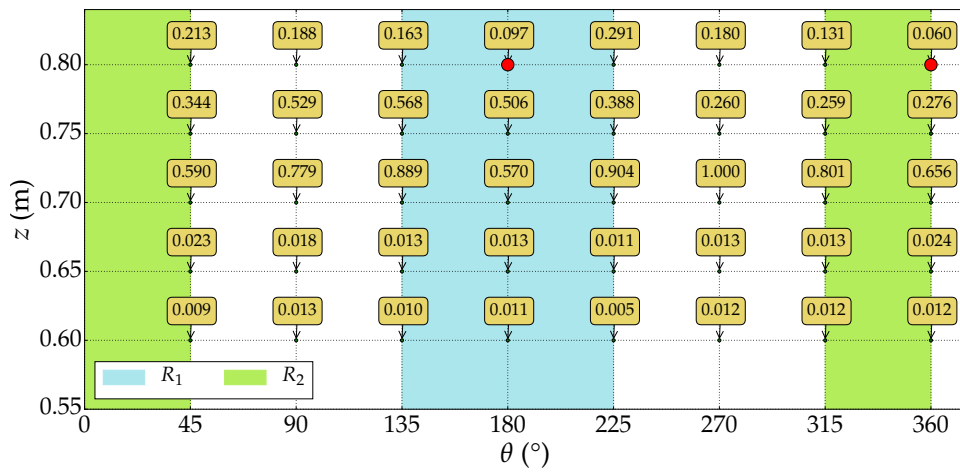


Figure 4.8: Mixing estimator in Case 9. Red dots mark the axes of the hot inlets.

Table 4.2: Maximum mixing estimator in each experimental case. Inner-surface temperatures were recorded at 1000 Hz in underlined cases.

l , or case number	$\max_l \bar{\delta}$ (K)	l , or case number	$\max_l \bar{\delta}$ (K)
<u>1</u>	13.92	6	7.61
<u>2</u>	12.43	7	12.56
<u>3</u>	5.63	8	7.97
<u>4</u>	10.41	9	7.77
5	13.51	10	6.15

indicate that, within R_1 and R_2 , the mixing estimator is highest at $(225^\circ, 0.68 \text{ m})$ and $(315^\circ, 0.68 \text{ m})$ in Case 2 and at $(225^\circ, 0.70 \text{ m})$ and $(315^\circ, 0.70 \text{ m})$ in Case 9. Consequently, the z -coordinate where mixing is most non-uniform increases if the mass flow rates through the hot inlets reduce, probably because the decreased mass fluxes hinder the hot water streams from reaching far down the annular region. In addition, with decreasing mass flow rates through the hot inlets, mixing intensity seems to benefit less from the hot stream at 360° , to the extent that one critical zone, stretching from 225° to 315° , can be detected in Case 9 – see Fig. 4.8. Moreover, Fig. 4.7 shows that mixing intensity is high at $(360^\circ, 0.65 \text{ m})$ and $(45^\circ, 0.65 \text{ m})$ in Case 2, comparably to Case 1. The range of normalized inner-surface temperatures at 0.65 m in Case 2 also confirms noteworthy fluctuations there. These findings hint that mixing in Case 2 is highly inhomogeneous at a range of axial levels, unlike Case 9, which exhibits abrupt transitions – see Fig. 4.8. Neighbor measurement positions are axially farther from one another in Case 9 than in Case 2, which might explain these sudden changes. A comparable issue stems from Table 4.2: here, the highest mixing estimator drops from 13.92 K in Case 1 and 12.43 K in Case 2 (matching the values for Cases 5 and 7, respectively) to 7.77 K in Case 9. Nevertheless, mass flow rates through the hot inlets steadily reduce with increasing case number in Cases 1 (or 5), 2 (or 7), and 9; correspondingly, the highest mixing estimator is expected to gradually decrease. As this expectation is not confirmed by values in Table 4.2, it can be argued that probing more z -coordinates in Case 9 may have a major impact on the mixing estimator there.

Cases 6, 8, and 10 are covered in Bergagio *et al.* (2017). In these cases, as already discussed in Cases 1, 2, 5, 7, and 9, the strongest temperature oscillations are detected and mixing is most inhomogeneous at lower z -coordinates if mass flow rates through the hot inlets increase. Moreover, as already observed in Cases 1, 2, 5, 7, and 9, the strongest temperature oscillations in region R_2 seem to emerge either at the same z -coordinates as in R_1 or at lower axial levels. This imperfect match could be once again related to asymmetries in the test-section geometry, under hot or cold conditions, or to discrepancies between flow rates through the hot inlets. Furthermore, analogously to Case 9, with decreasing mass flow rates through the

hot inlets, mixing inhomogeneity seems to profit less from the hot stream at 360° , to the point that only one critical zone, stretching from 225° to 315° , can be found in Case 10 (see Bergagio *et al.* (2017)).

Concerning thermal stratification, it can be studied through cases sharing all the boundary conditions but temperature T_C : decreasing T_C strengthens the vertical temperature gradient and thermal stratification. It can be demonstrated that stratification amplifies the highest mixing estimator, by contrasting $\max_l \bar{\delta}$ in Cases 1 and 5 ($T_C = 333$ K) with that in Case 6 ($T_C = 423$ K), $\max_l \bar{\delta}$ in Cases 2 and 7 ($T_C = 333$ K) with that in Case 8 ($T_C = 423$ K), and $\max_l \bar{\delta}$ in Case 9 ($T_C = 333$ K) with that in Case 10 ($T_C = 423$ K) – refer to Table 4.2. Nevertheless, when mass flow rates through the hot inlets are sufficiently low, thermal stratification reduces the range of normalized inner-surface temperatures at the z -coordinate where this range is highest. Comparing Case 2 with Case 8 and Case 9 with Case 10 confirms this statement, as detailed in Bergagio *et al.* (2017). Here, it is also shown that the highest mixing estimator increases with increased thermal stratification, presumably because more non-uniform, less progressed mixing thrives. Moreover, if thermal stratification strengthens, the range of normalized inner-surface temperatures at the z -coordinate where this range is widest often decreases, most likely because more non-uniform mixing is scattered over many axial levels. However, this range decreases less sharply when the mass flow rates through the hot inlets are sufficiently high; that is, when the mass fluxes of the hot streams balance thermal stratification. The decreased range could also stem from lack of measurement resolution in the axial direction. However, further evidence must back up these statements.

Mixing estimator $\bar{\delta}$ cannot clearly identify whether the hot streams rotate clockwise or counterclockwise around the vertical axis of the annulus, so this rotation is disregarded here.

4.3 Frequency analysis

Low frequencies are examined here because they are thought to cause fatigue, as highlighted in Subsection 2.1.3. The DFT of the low-pass filtered inner-surface temperatures helps to identify low-frequency fluctuations. Here, the DFT is performed on temperature records at measurement positions with the highest mixing estimator $\bar{\delta}$. As previously demonstrated, the range of normalized inner-surface temperatures is often widest at the z -coordinates of the above positions. Moreover, mixing descriptors derived from the integral of the DFT spectrum over low frequencies peak at the above positions or nearby (Bergagio *et al.* (2017)); therefore, these correlations plausibly support the choice of such measurement positions, even though the non-stationary, highly sporadic temperature time series recorded there are often unsatisfactorily processed using the DFT method. This shortcoming is addressed by processing these time series in Cases 1 and 2 using the HHT method. In addition, their Hilbert-Huang marginal spectra are shown.

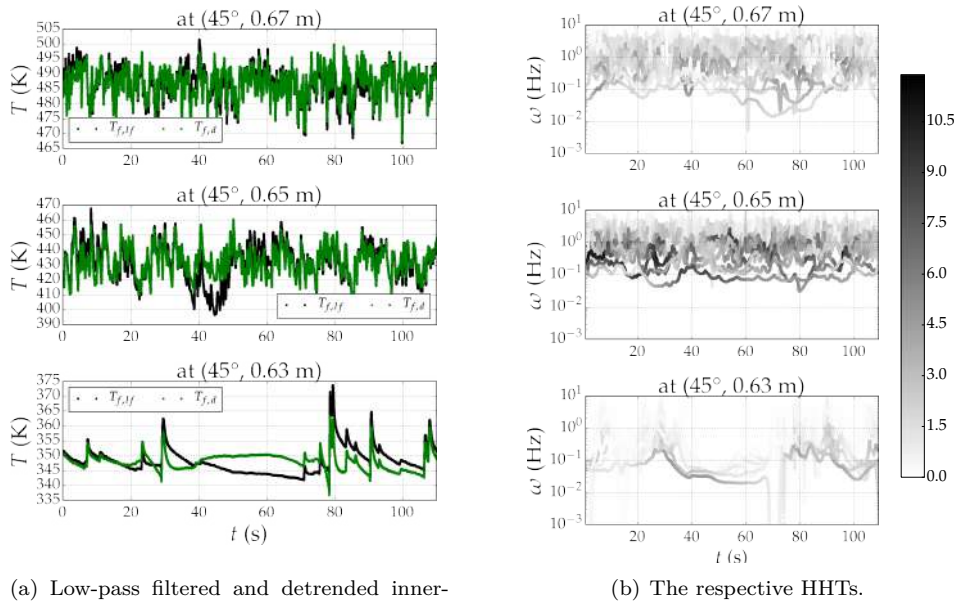
Figs. 4.9(a), 4.10(a), and 4.11(a) exemplify detrended inner-surface temperatures, while Figs. 4.9(b), 4.10(b), and 4.11(b) show the respective HHTs. The labels of all thermocouples recording these temperatures are left out, aside from $H1$ – this is justified later. Three inner-surface temperature time series are presented in each of Figs. 4.9(a), 4.10(a), and 4.11(a), before and after being detrended: one at the measurement position, from region R_1 or R_2 , with the highest mixing estimator in a specific case; and one at each of its nearest axial neighbors. The inner-surface temperature time series in a given figure are measured at distinct acquisition times. On the whole, detrending seems to preserve the dispersion of each time series around its mean, identify realistic trends, and minimize the overshoot and undershoot commonly troubling upper and lower envelopes when extrema are interpolated via cubic splines. However, incipient mixing – such as at $(45^\circ, 0.63\text{ m})$ in Case 1, as displayed in Fig. 4.9(a) –, along with sudden peaks and valleys where mixing inhomogeneity is strongest – such as at $(45^\circ, 0.65\text{ m})$ in Case 1, as displayed in Fig. 4.9(a) –, might need further tuning.

Each of Figs. 4.9(b), 4.10(b), and 4.11(b) depicts the HHTs of the detrended time series to its left. Here, ω denotes the instantaneous frequency in Subsection 3.3.3. Colors indicate amplitudes: the brighter the color, the lower the amplitude, as elucidated by the color bar on the right side of every figure. To clarify this, note that frequencies between 0.01 Hz and 0.2 Hz contain most of the signal energy at $(225^\circ, 0.65\text{ m})$ in Case 1, as shown in Fig. 4.10(b).

The Hilbert-Huang spectra in the aforesaid figures – mainly those in Figs. 4.9(b) and 4.11(b) – highlight that the largest amplitudes appear at frequencies lower than or comparable to 0.1 Hz at the measurement positions where mixing is seen most inhomogeneous. There, lower, more sporadic amplitudes arise from the HHTs at frequencies higher than 1 Hz. High amplitudes at low frequencies could suggest larger vortices, whereas secondary, unsteady amplitudes at higher frequencies could hint at smaller vortices.

To thoroughly compare DFTs with Hilbert-Huang marginal spectra, the DFTs of the detrended inner-surface temperatures from Figs. 4.9(a), 4.10(a), and 4.11(a) are depicted in Figs. 4.12, 4.15, and 4.17, respectively, whereas their respective Hilbert-Huang marginal spectra are portrayed in Figs. 4.13, 4.16, and 4.18. As stated before, the DFT method was applied after windowing these temperatures. In order to elucidate the key features of Hilbert-Huang marginal spectra, they are only shown at the measurement positions with the highest mixing inhomogeneity, in region R_1 or R_2 , for a specific case. Additionally, Figs. 4.13, 4.16, and 4.18 represent the Hilbert-Huang marginal spectra of the IMFs evolving on the longest time scales. Subset $S = \{g_{c_0-4}, \dots, g_{c_0-1}\}$ comprises these IMFs.

Generally speaking, DFTs confirm the effectiveness of the mixing estimator from Figs. 4.5, 4.6, and 4.7: DFTs evidence noticeable peaks in the range 0.03-0.2 Hz, at the measurement positions with the highest mixing inhomogeneity, in region R_1 or R_2 , for a given case. These peaks appear higher than those in the DFT spectra of their nearest axial neighbors. This relation applies to the 36 time series in Figs. 4.19(a) and 4.19(c), thus underpinning the assessment of mixing intensity and non-



(a) Low-pass filtered and detrended inner-surface temperatures (that is, $T_{f,lf}$ and $T_{f,d}$, respectively).

(b) The respective HHTs.

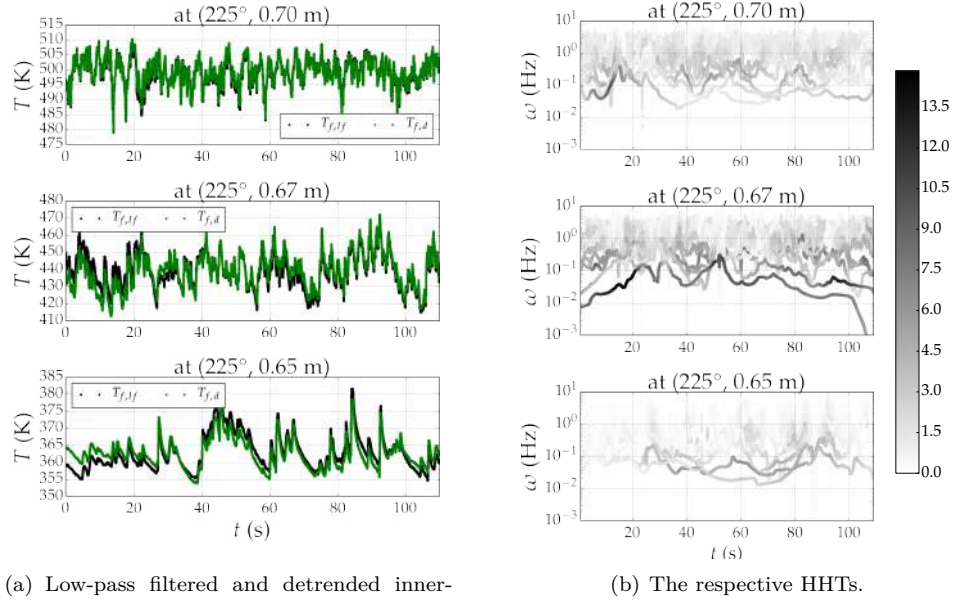
Figure 4.9: Selection of low-pass filtered and detrended inner-surface temperatures in Case 1 at 45° . The respective HHTs are shown as well. Data from thermocouple $H1$.

uniformity through estimator $\bar{\delta}$. Moreover, if the aforesaid 36 time series and their nearest axial neighbors are ranked by peak amplitude, the resulting rank matches that derived from $\bar{\delta}$.

Concerning Hilbert-Huang marginal spectra, Fig. 4.13 essentially corresponds to Fig. 4.12, since they show the highest peaks at $(45^\circ, 0.65 \text{ m})$ – four in the DFT, three in the Hilbert-Huang marginal spectrum – in the same frequency range. The most prominent peak in the Hilbert-Huang marginal spectrum appears to arise from g_{c_0-1} , whereas the second and third most prominent seem to originate from g_{c_0-2} . The highest peaks in Fig. 4.13 emerge at 0.07 Hz; comparably, those in Fig. 4.14 occur at 0.05 Hz. This similarity bolsters the hypothesis that one scalar quantity can concisely represent time series at the same measurement position, even though recorded at disparate measurement times, given that such time series exhibit analogous frequencies.

Moreover, Figs. 4.15 and 4.16 show compatible frequencies for the highest peaks at $(225^\circ, 0.67 \text{ m})$ in Case 1. Here, similarly to Fig. 4.13, subset S comprises the IMF producing the highest spectral peak.

By contrast, while Fig. 4.18 reveals peaks at 0.07 Hz and ~ 0.1 Hz, Fig. 4.17



(a) Low-pass filtered and detrended inner-surface temperatures (that is, $T_{f,lf}$ and $T_{f,d}$, respectively).

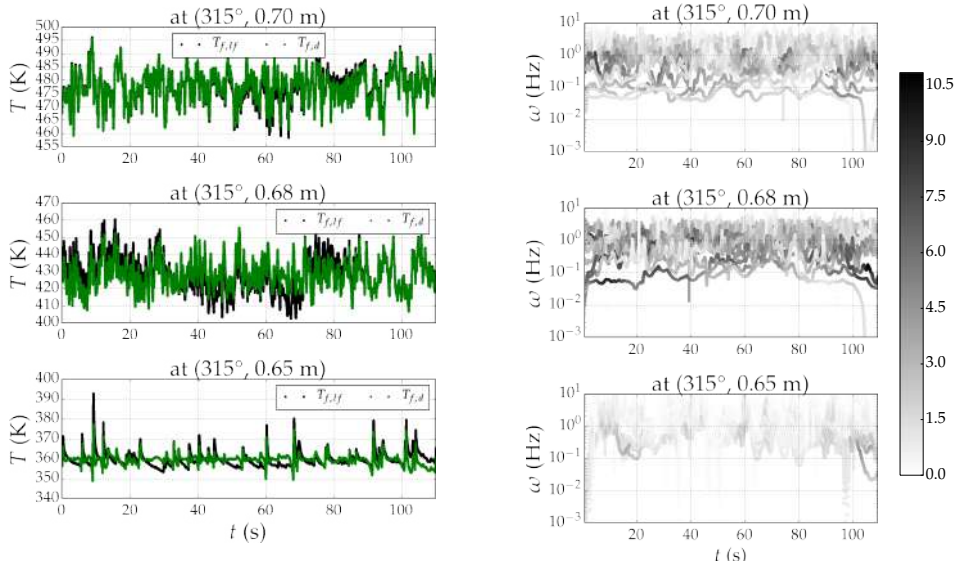
(b) The respective HHTs.

Figure 4.10: Selection of low-pass filtered and detrended inner-surface temperatures in Case 1 at 225° . The respective HHTs are shown as well.

hints that the DFT adds spurious harmonics to reproduce non-stationarity, thus scattering the signal energy over a broader band of frequencies, around 0.3 Hz, 0.5 Hz, and 0.7 Hz. Fig. 4.18 suggests that modes g_{c_0-3} and g_{c_0-1} produce the aforesaid spectral peaks.

Figs. 4.19(a) and 4.19(c) present frequencies at the two highest peaks in the Hilbert-Huang marginal spectra of 36 inner-surface temperature time series from the measurement positions with the highest mixing inhomogeneity, in R_1 and R_2 , for Cases 1 and 2; specifically, 18 detrended time series are examined in each case. These figures attest that inner-surface temperatures from the most significant zone of the mixing region reveal conspicuous spectral peaks, from 0.03 to 0.10 Hz, in Cases 1 and 2. The above figures also indicate that this frequency range widens if mass flow rates through the hot inlets increase: the peaks in the Hilbert-Huang marginal spectra of the time series from Case 1 ($\dot{m}_H = 0.8 \text{ kg s}^{-1}$) spread between 0.03 and 0.06 Hz, whereas those from Case 2 ($\dot{m}_H = 0.6 \text{ kg s}^{-1}$) seem to approach 0.04 Hz.

According to Figs. 4.19(b) and 4.19(d), the IMFs generating the most prominent spectral peaks in Cases 1 and 2 are near the upper bound of subset S ; in other



(a) Low-pass filtered and detrended inner-surface temperatures (that is, $T_{f,lf}$ and $T_{f,d}$, respectively).

(b) The respective HHTs.

Figure 4.11: Selection of low-pass filtered and detrended inner-surface temperatures in Case 2 at 315° . The respective HHTs are shown as well.

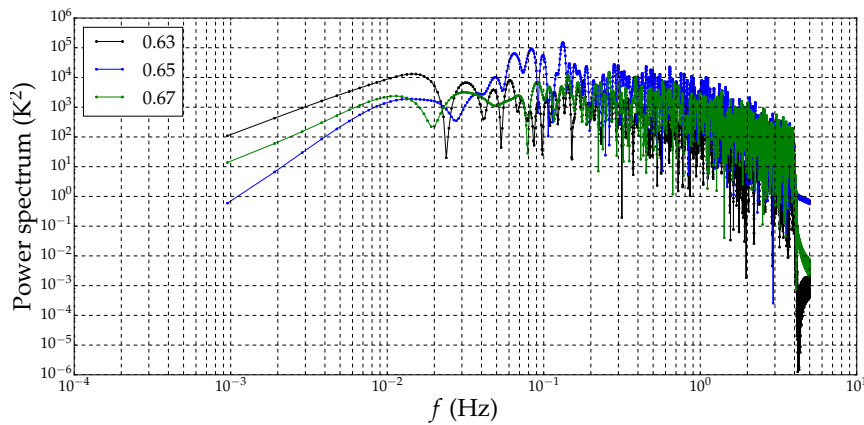


Figure 4.12: DFTs in Case 1 at 45° . Data from thermocouple $H1$. The legend lists z -coordinates in m.

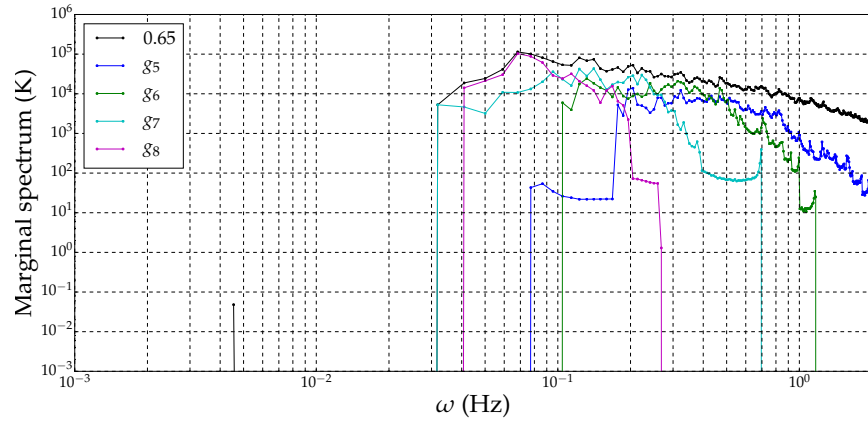


Figure 4.13: Hilbert-Huang marginal spectrum in Case 1, at $(45^\circ, 0.65 \text{ m})$. The spectra of the IMFs evolving on the longest time scales are also shown. Data from thermocouple *H1*.

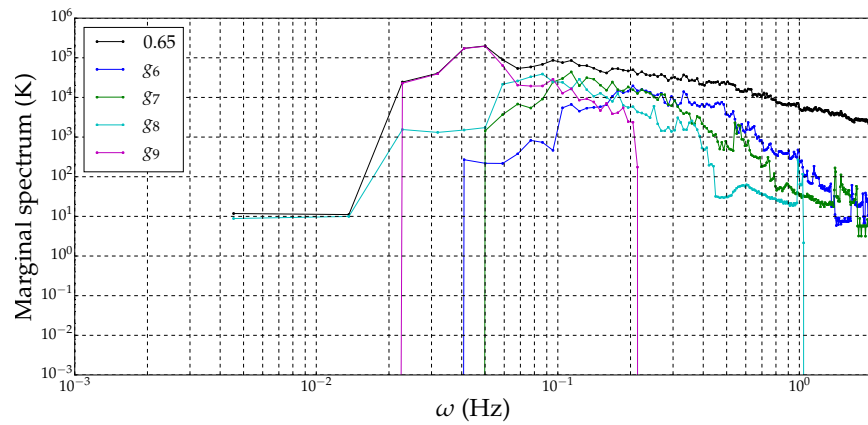


Figure 4.14: Hilbert-Huang marginal spectrum in Case 1, at $(45^\circ, 0.65 \text{ m})$. The spectra of the IMFs evolving on the longest time scales are also shown. Data from thermocouple *V1*.

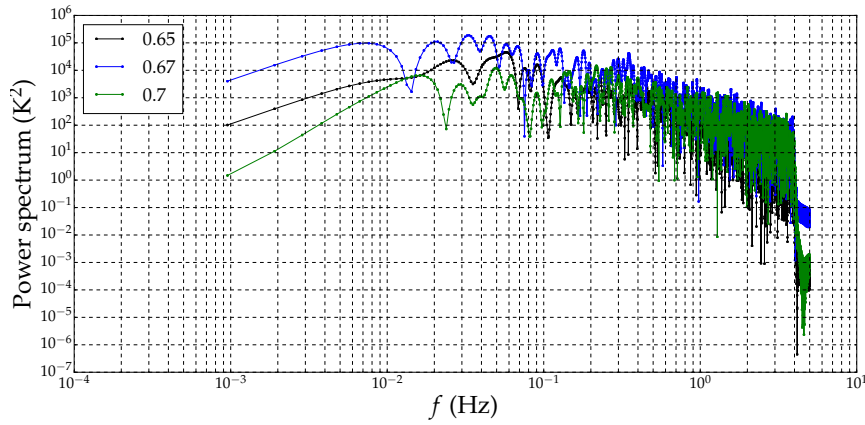


Figure 4.15: DFTs in Case 1 at 225°. The legend lists z -coordinates in m.

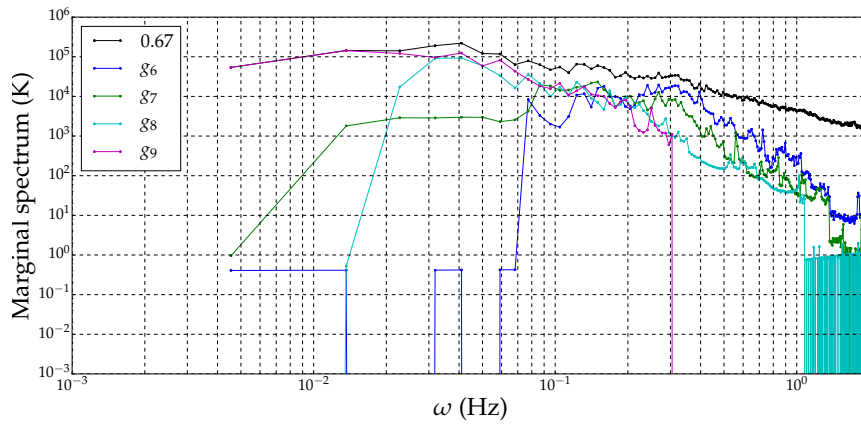


Figure 4.16: Hilbert-Huang marginal spectrum in Case 1, at (225°, 0.67 m). The spectra of the IMFs evolving on the longest time scales are also shown.

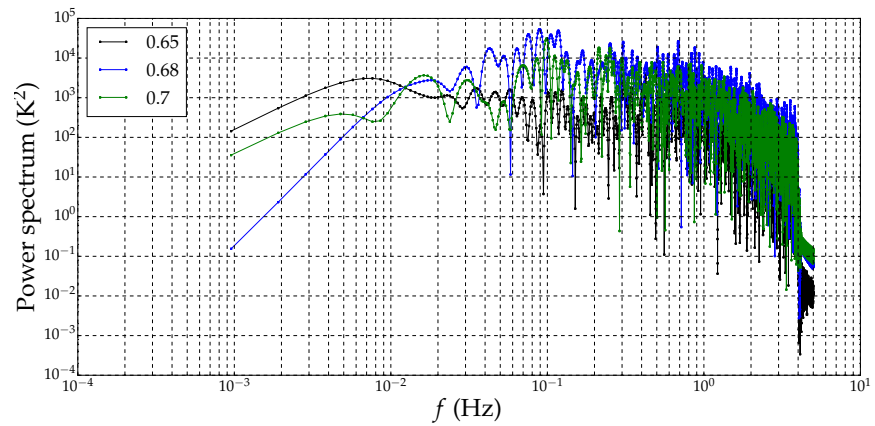


Figure 4.17: DFTs in Case 2 at 315° . The legend lists z -coordinates in m.

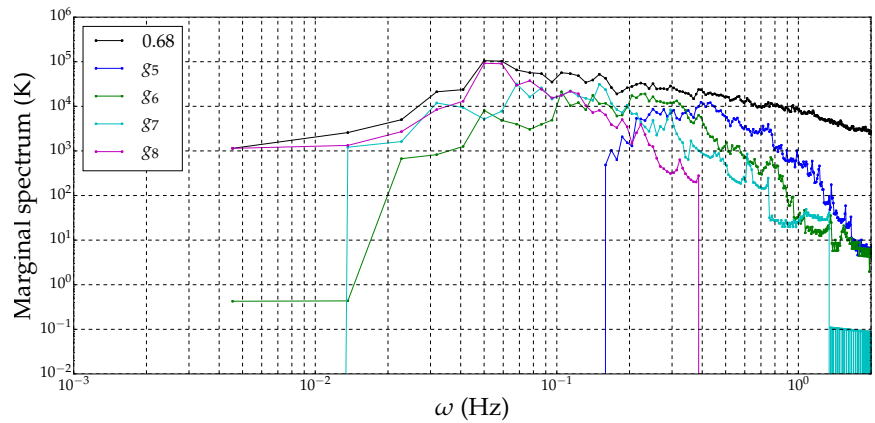


Figure 4.18: Hilbert-Huang marginal spectrum in Case 2, at $(315^\circ, 0.68 \text{ m})$. The spectra of the IMFs evolving on the longest time scales are also shown.

words, they evolve on the longest time scales. Thus, constant $\hat{\delta}$, which helps to distinguish which IMFs belong to the trend (refer to Subsection 3.3.2), plays a key role in finding the frequency range associated with the most conspicuous spectral peaks.

Mode mixing occurs when spectral components with analogous instantaneous frequencies surface in the HHTs of distinct IMFs or when spectral components of appreciably different frequencies arise in the HHT of a particular IMF. This drawback, which could mar the accuracy of Figs. 4.9(b), 4.10(b), 4.11(b), 4.13, 4.14, 4.16, 4.18, and 4.19, is commonly overcome by, e.g., applying the EEMD (Ensemble EMD) (see Wu and Huang (2009)), Complementary EEMD (see Yeh *et al.* (2010)), and Complete EEMD (see Torres *et al.* (2011)). Even though these methods are not treated here, it is worth mentioning that the EEMD applies the EMD to the time series after adding independent, identically distributed white noise to the signal: the EMD works as a dyadic filter bank if applied to white (or fractional Gaussian) noise, so it often loses this property if applied to intermittent signals. Complementary and Complete EEMD address issues arising from the connection between white noise added to the time series and number of modes as well as from the residual white noise in the EEMD.

4.4 Uncertainty analysis

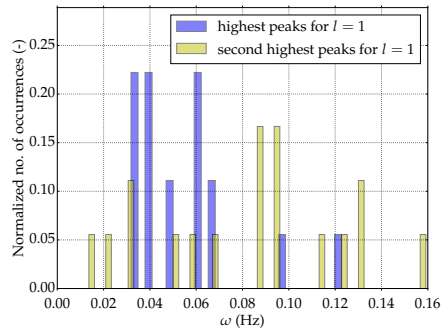
Table 4.3 lists all elements in arrays \tilde{B}^+ , \tilde{B}^- , and \tilde{S} .

Table 4.3: Elements in arrays \tilde{B}^+ , \tilde{B}^- , and \tilde{S} . Temperatures sampled at 1000 Hz. End-to-end calibration data were accessible here.

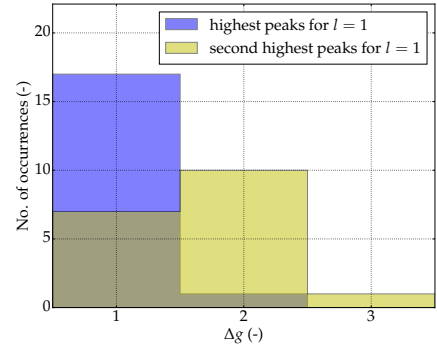
Component _{<i>i</i>}	$\tilde{B}^+[i]$ (K)	$\tilde{B}^- [i]$ (K)	$\tilde{S}[i]$ (K)
K-type thermocouple	1.50	-1.50	0
Thermocouple mounting	0.31	-0.31	0
Data acquisition equipment	0.37	-0.37	0.07

Values in Table 4.3 allow to compute the total uncertainty, which equals $U_{95} = 1.58$ K, while shift ΔU_{95} is zero.

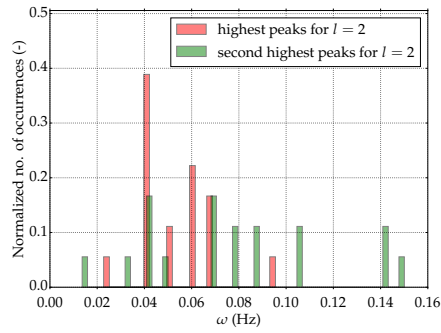
Systematic uncertainties from system noise, offset, and gain error – all constituting the absolute accuracy – are listed in Table 4.4. These values, all supplied by the manufacturer, would raise the total uncertainty $U_{95, bc}$ to 3.87 K, while shift $\Delta U_{95, bc}$ would equal 0.02 K. Accordingly, positive-side and negative-side uncertainties would reach $U_{95, bc}^+ = U_{95, bc} - \Delta U_{95, bc} = 3.85$ K and $U_{95, bc}^- = -U_{95, bc} - \Delta U_{95, bc} = -3.89$ K, respectively.



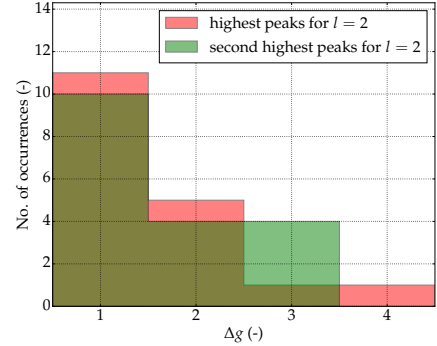
(a) Frequencies at the two highest peaks in each of the 18 spectra from Case 1. Occurrences are normalized to total 1.



(b) Δg associated with the two highest peaks in each of the 18 spectra from Case 1. Δg is the number of IMFs in a time series after subtracting the index of the IMF that contributes the most to a specific peak.



(c) Frequencies at the two highest peaks in each of the 18 spectra from Case 2.



(d) Δg associated with the two highest peaks in each of the 18 spectra from Case 2.

Figure 4.19: Peaks in the Hilbert-Huang marginal spectra of the inner-surface temperatures with the highest mixing estimator.

Table 4.4: Elements in arrays \tilde{B}^+ , \tilde{B}^- , and \tilde{S} . Temperatures sampled at 100 Hz. End-to-end calibration data were not accessible here.

Component _{<i>i</i>}	$\tilde{B}^+[i]$ (K)	$\tilde{B}^-[i]$ (K)	$\tilde{S}[i]$ (K)
K-type thermocouple	1.50	-1.50	0
Thermocouple mounting	0.09	-0.09	0
DAQ-6024E card (National Instruments (2008))	3.39	-3.37	0
SCXI-1102 module (National Instruments (2004))	1.16	-1.13	0

4.5 LES, FEA, and fatigue assessment

The simulation time is ~ 13 s. Start time t_0 and end time t_{end} equal 16.3 s and 29.2 s, respectively. LES results from the first 2.9 s are typically not postprocessed; hence, start time $t_0 = 19.2$ s is usually selected. The simulation took 130 days of computational time on an academic supercomputing system. In this section, LES results are presented and related to data from Case 1 of the experimental matrix (see Table 3.3).

LES temperatures are sampled at the locations in Fig. 4.20. Experimental inner-surface temperatures were sampled at the same angles (see Fig. 3.10). For ease of notation, as in Section 4.2, θ and z replace θ^* and z^* respectively.

Streamwise velocity profiles at the inlet pipes are presented in Bergagio *et al.* (2018a). It is thus proved that internal mapping creates self-similar (fully developed) velocity profiles. Furthermore, these profiles are deemed reasonable after comparing them with analytical and empirical profiles.

Fig. 4.21 illustrates LES temperatures in the water region at $z = 0.67$ m (see Fig. 3.13) and eight times. A snapshot is saved every ~ 1.4 s. During these ~ 10 s temperatures there change considerably, frequently cycling from 400 K to 500 K. Large, irregular, unstable hot structures reach this cross section at different locations and times; for example, at 24.98 s, a large hot structure touches the cross section at $\sim 135^\circ$, but colder water takes its place 1.45 s later, when hot structures rim the inner tube from 180° to 270° . Overall, inner-surface temperatures at 360° are lower than at 90° , although the hot inlets are situated at 180° and 360° . This discrepancy is explored later. Folder U_and_T (Bergagio (2018a)) contains full-size snapshots.

Fig. 4.22 illustrates the LES velocity magnitude at the same times and z as in Fig. 4.21. Folder U_and_T (Bergagio (2018a)) contains full-size snapshots. In Fig. 4.22, the velocity magnitude is higher for the hot structures, particularly if water is

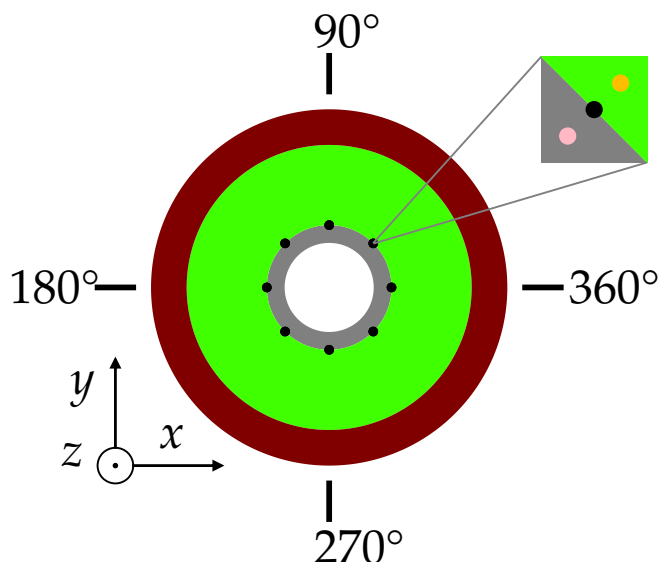


Figure 4.20: Locations at which LES temperatures are sampled. Green: water. Gray: inner tube. Red: outer tube. Orange dot (WB): at $\delta = 0.035$ mm from the inner surface, in the water region. Black dot: at R_{io} ; i.e., on the inner surface. Pink dot (TB): at $\delta = 0.035$ mm from the inner surface, in the inner tube.

poorly or not mixed. Consistently, analogously to Fig. 4.21, the velocity magnitude is lower at 180° and 360° than at 90° and 270° . In-plane velocity components are usually larger in the shear layer between cold and hot structures. Even when mixing is weak, at $z = 0.67$ m the maximum velocity magnitude of the hot structures is considerably reduced, to roughly 10% the velocity magnitude at the hot inlets ($z = 0.80$ m). Notwithstanding, velocity redistribution appears sparingly, because the hot structures traveling downwards are faster and lighter than the cold stream flowing upwards, and because the density difference between hot structures and cold stream is large. Vortices are portrayed in Figs. 4.22 and 4.23. Despite their chaotic nature and range of sizes, most vortices seem to initiate or intensify mixing: Figs. 4.21 and 4.22 hint that vortices are usually absent in areas of extreme temperatures.

As stated above, mean inner-surface and WB temperatures at 180° and 360° are lower than at 90° and 270° . As proved by Fig. 4.23 and figures in folder **Q_and_Uz** (Bergagio (2018a)), this discrepancy could stem from two sources: (1) vortices descending at 90° and 270° into the near-wall layer are hotter and reach farther down than vortices at 180° and 360° ; (2) colder, typically upright vortices at 90°

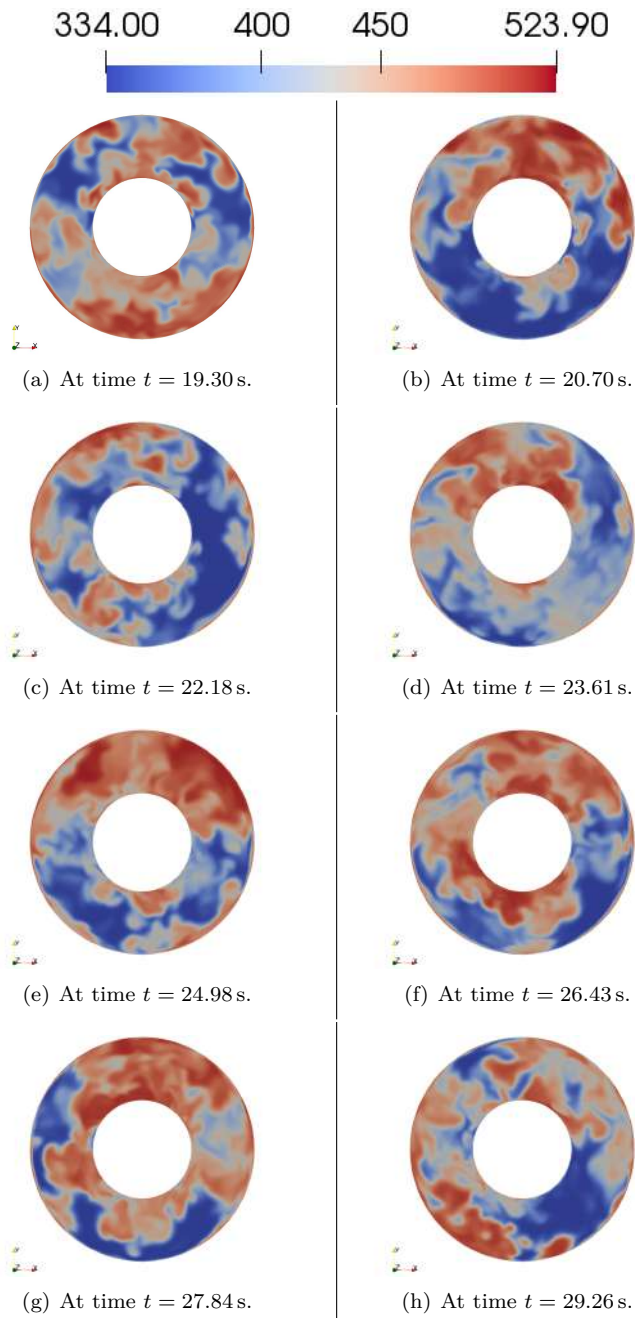


Figure 4.21: Temperature in K at eight times. Water region. $z = 0.67$ m.

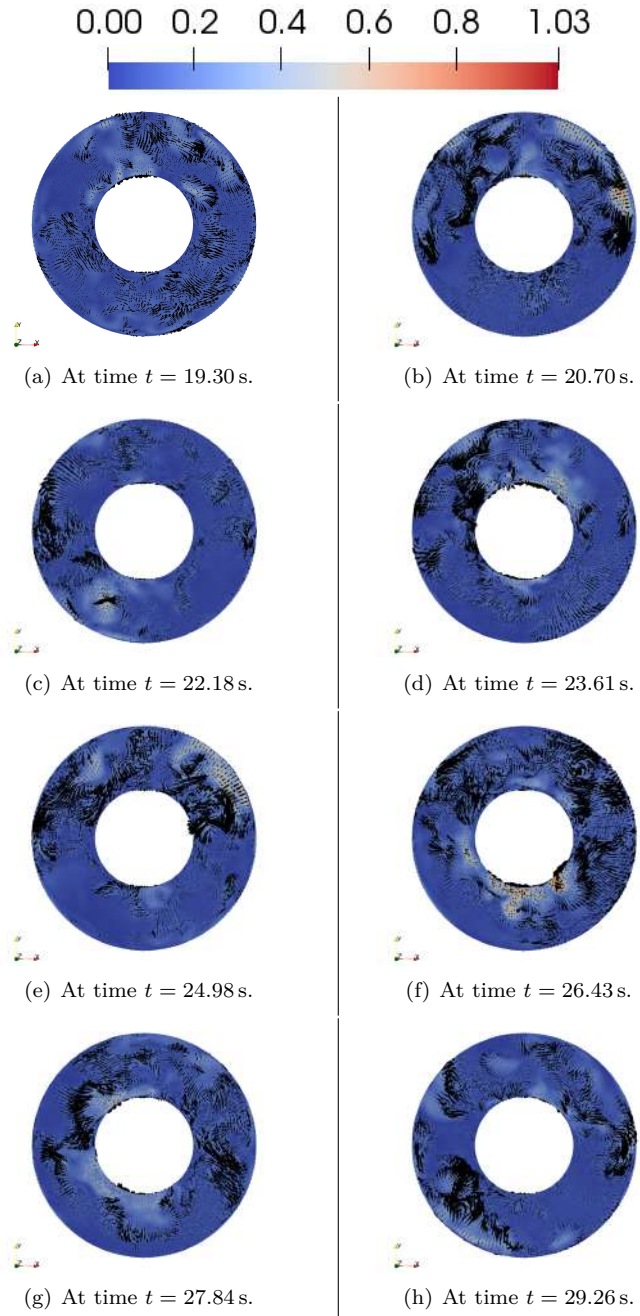


Figure 4.22: Velocity magnitude in ms^{-1} with in-plane velocity vectors at eight times. $z = 0.67$ m.

and 270° rise from as low as 0.60 m. These elongated vortices cause more dissipation of kinetic energy into heat than the 2D structures emerging from the flow at 180° and 360° near 0.60 m. Hence, smoother, less abrupt mixing occurs at 180° and 360°, with axial velocity alternating between positive and negative values at about 0.70 m. In Fig. 4.23, vortices are depicted by isocontours of $Q = 0.5 \text{ s}^{-2}$. Q is defined as the second invariant of the velocity gradient (OpenFOAM (2017)) or, interchangeably, as follows:

$$Q = \frac{1}{2} \left((\nabla \cdot \tilde{\mathbf{u}})^2 + \tilde{\mathbf{\Omega}} : \tilde{\mathbf{\Omega}} - \tilde{\mathbf{S}} : \tilde{\mathbf{S}} \right). \quad (4.1)$$

Here, the vorticity tensor is computed as $\tilde{\mathbf{\Omega}}(\tilde{\mathbf{u}}) = \frac{1}{2}(\nabla\tilde{\mathbf{u}} - (\nabla\tilde{\mathbf{u}})^T)$, while the rate-of-strain tensor $\tilde{\mathbf{S}}$ is calculated from Eq. (3.17). In incompressible flows, a positive Q evidences that the vorticity magnitude overcomes the rate-of-strain magnitude (see Eq. (4.1)). The map of y^+ on the inner surface in Fig. 3.12 also suggests more turbulence at 90° and 270°.

Fig. 4.24 represents temperatures at two positions in the mixing region. Fig. 4.24 proves that the inner tube acts as a low-pass filter, since it attenuates high-frequency temperature oscillations owing to its thermal inertia: in Fig. 4.24(a), temperature ranges on the inner surface (7 K) and in the inner tube (6 K) are less than half that in the near-wall water layer (22 K). In Fig. 4.24(b), an analogous behavior is evidenced, but here ranges are appreciably higher: temperatures in the inner tube, on the inner surface, and in the near-wall water layer cover about 37 K, 35 K, and 80 K, respectively. The increased ranges suggest that the temperature range changes considerably with axial level and measurement region (be it WB, inner surface, or TB). Fig. 4.24 also attests that the radial heat flux changes sign intermittently, when water is colder than the inner tube. Thus, frequency analysis methods ought to tackle intermittent time series.

Fig. 4.25 stresses that temperature ranges and frequencies vary with azimuthal coordinate. Here, LES and experimental inner-surface temperatures are shown at four angles, at 0.67 m. Means and ranges of LES temperatures match their experimental counterparts at (90°, 0.67 m) (here, mean ~ 488 K) and (180°, 0.67 m) (here, mean ~ 427 K), but they do not at (270°, 0.67 m) and (360°, 0.67 m): LES means equal 472 K at the former location and 434 K at the latter, whereas experimental means equal 432 K at the former location and 487 K at the latter; in other terms, their means appear roughly swapped. Further evidence – see, e.g., Figs. `mean(dimensionless T)_exp.pdf` and `mean(dimensionless T)_LES.pdf` (Bergagio (2018a)) – suggests that mean LES and experimental temperatures can be compared at the axial, not azimuthal, measurement locations. Experimental temperatures at (90°, 0.67 m) correlate less with those at (270°, 0.67 m) than with those at (360°, 0.67 m), thus breaking azimuthal symmetry. This inconsistency could arise from several factors (see Section 4.2). It is worth noting that inlet temperatures and velocities in Table 3.7 were measured in the HWAT loop when inner-surface temperatures were recorded at 0.65 m.

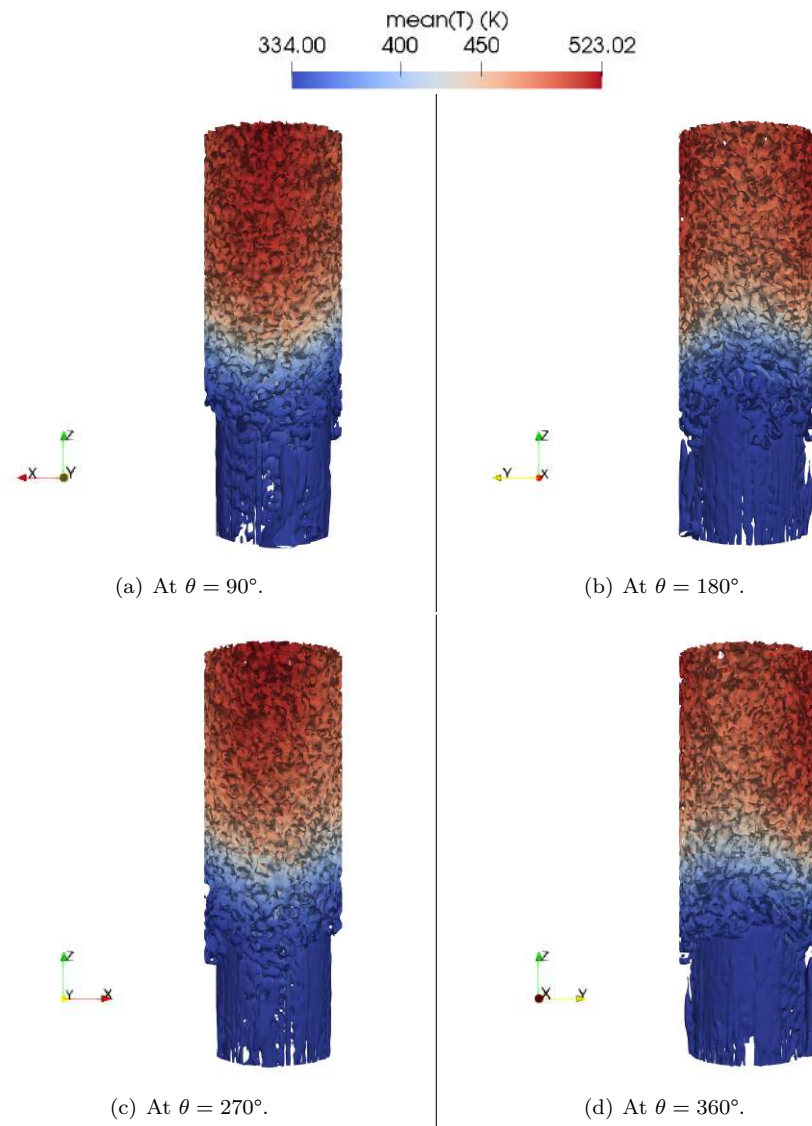


Figure 4.23: 3D views of time-averaged Q isocontours colored by time-averaged temperature. $17.5 \times 10^{-3} \text{ m} \leq r \leq 22.5 \times 10^{-3} \text{ m}$. $0.60 \text{ m} \leq z \leq 0.73 \text{ m}$. Start time $t_0 = 19.2 \text{ s}$. $Q = 0.5 \text{ s}^{-2}$.

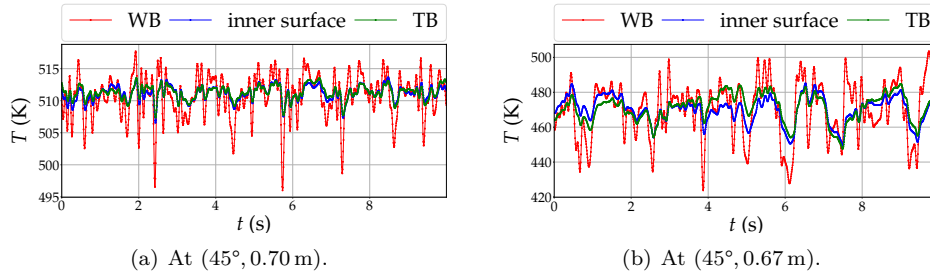


Figure 4.24: LES temperatures at WB, on the inner surface, and at TB.

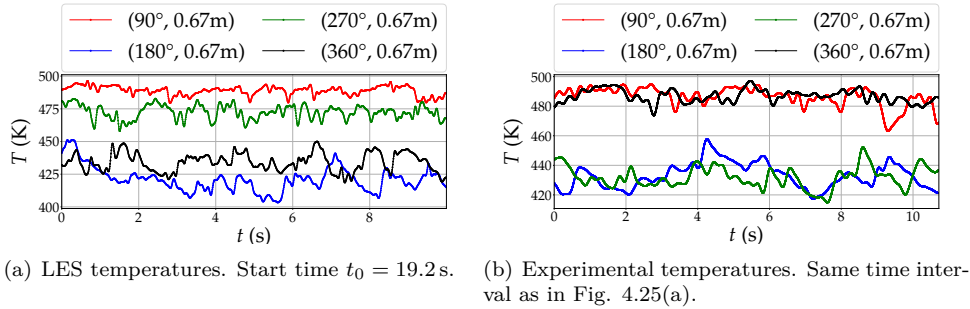
Figure 4.25: LES and experimental inner-surface temperatures, at four angles and $z = 0.67 \text{ m}$.

Fig. 4.26 shows lowest, mean, and highest LES inner-surface temperatures along z , in the mixing region. Here, LES temperatures are normalized according to Eq. (3.10); consequently, Figs. 4.26 and 4.4(a) can be compared with each other. LES temperatures are not filtered or detrended, unlike experimental temperatures. Similarly to Fig. 4.4(a), above $\zeta = 1.78$ ($z = 0.72 \text{ m}$) and below $\zeta = 3.78$ ($z = 0.63 \text{ m}$), the small deviation from mean temperatures suggests minor mixing inhomogeneity there. On average, the lowest, mean, and highest experimental temperatures tally with their LES analogues. Nevertheless, at $\zeta = 3.33$ ($z = 0.65 \text{ m}$), experimental temperatures deviate more from the mean, as could be expected: the inner-tube thermocouples, whose tips are flush with the inner surface, monitor these temperatures in the water domain.

The mixing estimator in Section 3.4 is also computed from LES inner-surface temperatures. Its values are reported in Fig. 4.27. Fig. 4.5 shows the mixing estimator calculated from experimental inner-surface temperatures. Regions R_1 and R_2 are defined in Section 4.2. Mixing inhomogeneity tops 0.75 at $(90^\circ, 0.65 \text{ m})$, $(180^\circ, 0.67 \text{ m})$, $(45^\circ, 0.67 \text{ m})$, and $(225^\circ, 0.67 \text{ m})$ in Fig. 4.27 (LES values) and

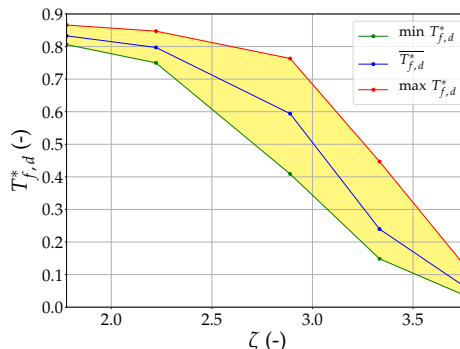


Figure 4.26: Axial distribution of the highest, mean, and lowest values of the normalized LES inner-surface temperatures $T_{f,d}^*$. Yellow: area enclosed by the lower and upper envelopes. Start time $t_0 = 19.2$ s. Here, $\overline{T_{f,d}^*}$ represents $T_{f,d}^*$ averaged over time and angles.

at $(45^\circ, 0.65 \text{ m})$, $(360^\circ, 0.65 \text{ m})$, $(90^\circ, 0.65 \text{ m})$, $(225^\circ, 0.67 \text{ m})$, and $(270^\circ, 0.67 \text{ m})$ in Fig. 4.5 (experimental values). Thus, mixing inhomogeneity appears stronger farther down in the experiment, particularly in region R_2 . Furthermore, LES peaks of mixing inhomogeneity are less commensurate to one another than their experimental equivalents. Numerical schemes and WALE model are relatively dissipative, which might explain these discrepancies. Moreover, at a given z , the experimental mixing inhomogeneity strengthens in R_2 , whereas LES results restore some correspondence between mixing non-uniformity values in R_1 and R_2 . Nevertheless, in both LES and experiment, velocities and temperatures at the hot inlets do not match, so azimuthal symmetry is lost: mixing inhomogeneity at θ deviates from that at $\theta + 180^\circ$, with $0^\circ < \theta \leq 180^\circ$.

In both Figs. 4.5 and 4.27, mixing is marginally inhomogeneous at 0.63 m, 0.70 m, and 0.72 m.

Altogether, Figs. 4.26 and 4.27 indicate that LES can capture some relevant features of the experimental data.

Fig. 4.28 depicts time-averaged stresses close to the interface between water and inner tube from the elastic model of the inner tube. High mixing inhomogeneity appears to trigger radial stresses of considerable magnitude, which, however, is typically lower than those of hoop and axial stresses at the same locations. Appreciable hoop stress gradients surface between 0.63 m and 0.68 m, mostly along z ; there, as shown in Fig. 4.28(b), hoop stresses alternate between tensile and compressive. By contrast, compressive hoop stresses of relatively small magnitude emerge in zones where the cold flow is unmixed ($z < 0.63 \text{ m}$), the hot inlet jets strike the inner surface ($z \sim 0.80 \text{ m}$), or mixing is highly homogeneous ($0.70 \text{ m} \leq z \leq 0.72 \text{ m}$). Fig. 4.28(c) highlights that time-averaged axial stresses

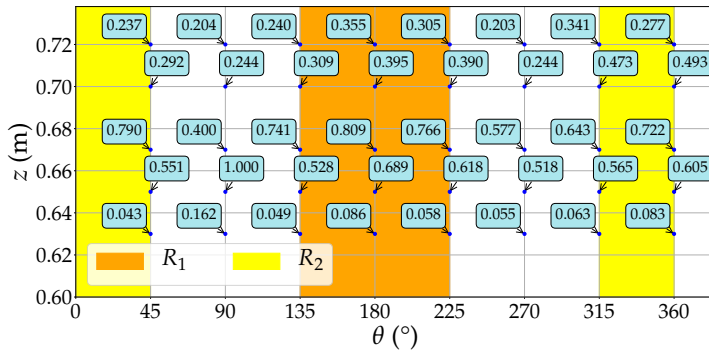


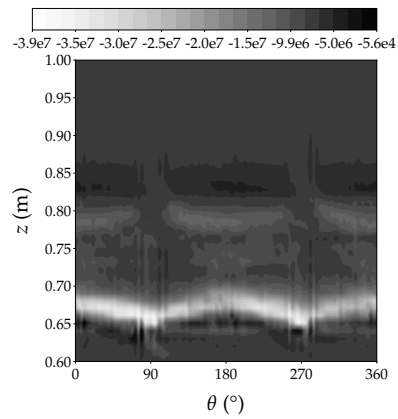
Figure 4.27: Mixing estimator. It is calculated as the mean standard deviation of the normalized LES inner-surface temperatures $T_{f,d}^*$ after outlier removal, for each measurement position. Values are normalized to the highest mixing estimator. Start time $t_0 = 19.2$ s.

are about ten times larger than time-averaged hoop stresses, probably because the “stripe constraint” (Miyoshi *et al.* (2014); Kamaya and Miyoshi (2017)) overcomes the “circumferential constraint”. Both constraints restrict the deformation due to mixing inhomogeneity; however, the circumferential constraint increases hoop stresses by acting azimuthally, whereas the stripe constraint enhances axial stresses by acting axially. Fig. 4.28(c) also reveals that the distribution of the time-averaged axial stresses mirrors the farther penetration of hot vortices into the annulus at 90° and 270° (see Figs. 4.23 and 4.25(a)). If Fig. 4.28(d) is compared to Fig. 4.27, axial stress ranges are remarkable at locations where mixing inhomogeneity is significant; that is, where inner-surface temperatures exhibit considerable variances. Kamaya and Nakamura (2011) and Costa Garrido *et al.* (2015) noted the same for T-junctions.

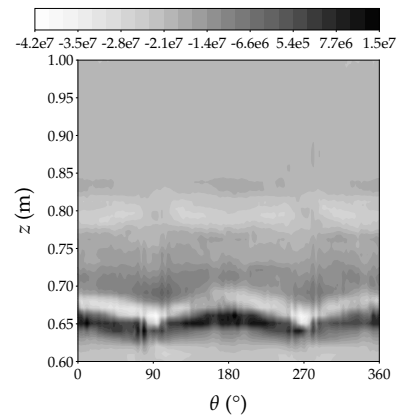
Estimating fatigue damage is crucial to determine dominant frequencies in inner-surface temperature time series from fatigue-prone areas. Fig. 4.29 evidences that the highest CUFs on the inner surface are reached in the interval $0.65\text{--}0.67$ m, between 45° and 135° as well as between 225° and 315° . These maxima are found in localized spots; hence, the inner tube should be finely meshed to catch them. If the LES load cycles are repeated until failure occurs (i.e., $D = 1$), cracking is expected to initiate after 97 h.

Data in Fig. 4.30 come from inner-surface CUFs at $0.60\text{ m} \leq z \leq 1.00\text{ m}$. Results of a time-step independence study are presented in Fig. 4.30(a), which evidences that CUFs computed using distinct time steps Δt and the same t_0 appear to converge if the current Δt is smaller than 0.10 s.

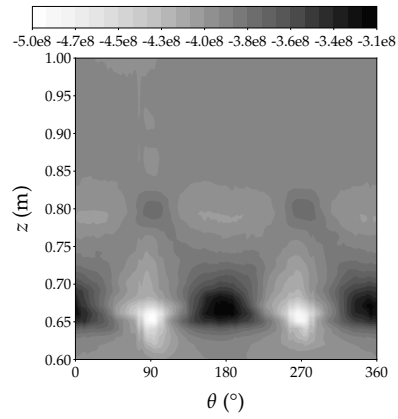
Fig. 4.30(b) evidences that CUFs computed using distinct start times t_0 and the same Δt appear to converge if t_0 increases. Notwithstanding, the optimal t_0



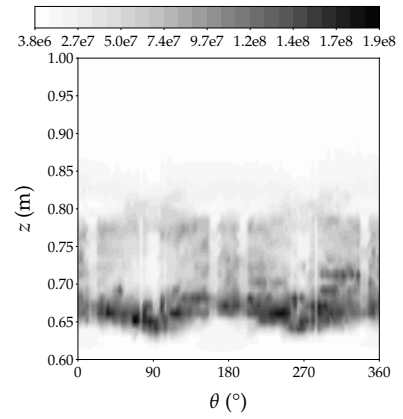
(a) Time-averaged radial stresses.



(b) Time-averaged hoop stresses.



(c) Time-averaged axial stresses.



(d) Axial stress range.

Figure 4.28: Stresses in Pa close to the inner surface, at $0.993 R_{i\sigma}$. Start time $t_0 = 19.2$ s.

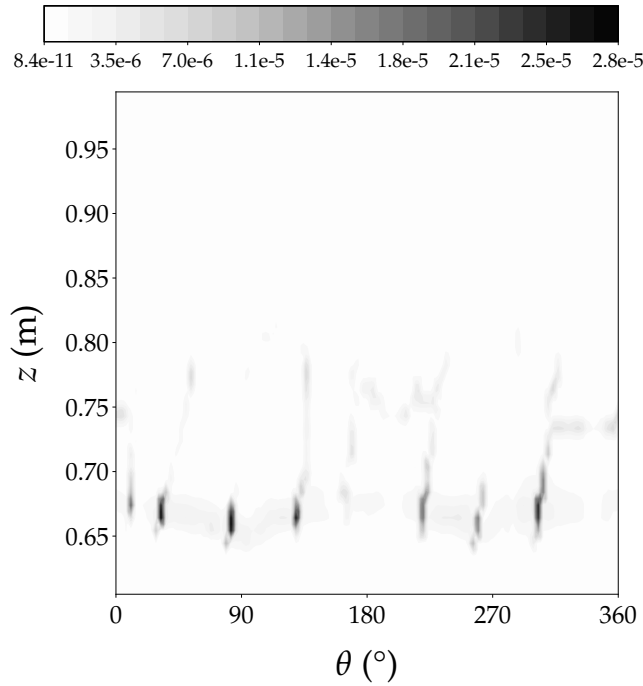
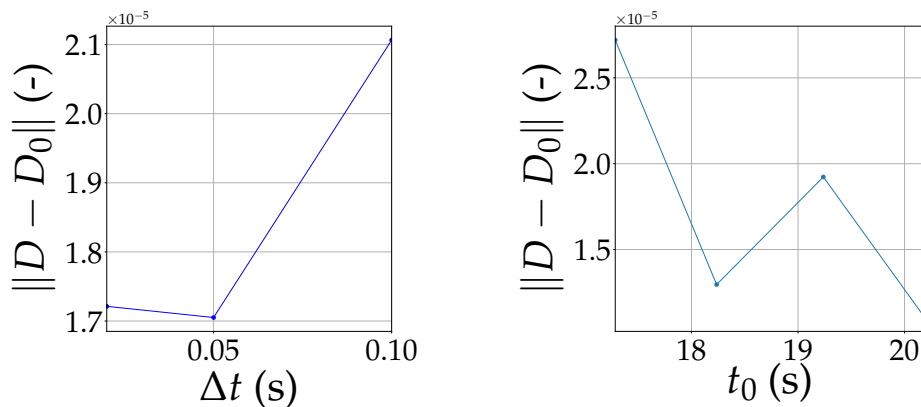


Figure 4.29: Inner-surface CUF. Start time $t_0 = 19.2$ s.

cannot be selected solely based on convergence: more cycles from the nodal stress time series are neglected if t_0 increases.

The measurement positions neighboring spots where the CUF is no less than 0.7 times the highest CUF are analyzed to find dominant frequencies in inner-surface temperature time series from fatigue-prone areas. When sorted by CUF, these positions are $(45^\circ, 0.67 \text{ m})$, $(90^\circ, 0.65 \text{ m})$, $(90^\circ, 0.67 \text{ m})$, $(135^\circ, 0.67 \text{ m})$, and $(315^\circ, 0.67 \text{ m})$ – see Fig. 4.29. The highest and third highest mixing estimators from LES data are observed at $(90^\circ, 0.65 \text{ m})$ and $(45^\circ, 0.67 \text{ m})$, respectively, which suggests that the CUF may correlate with mixing estimator $\bar{\sigma}$.

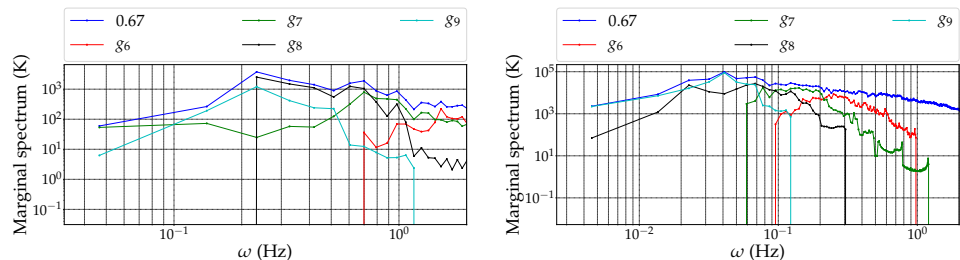
Hilbert-Huang transform and marginal spectrum, IMFs, instantaneous frequency, and index c_0 are detailed in Subsections 3.3.2 and 3.3.3. In this section, the Hilbert-Huang marginal spectra of both inner-surface temperature time series from fatigue-prone areas and their IMFs in subset $S = \{g_{c_0-4}, \dots, g_{c_0-1}\}$ (see Section 4.3) are shown. Fig. 4.31(a) illustrates the Hilbert-Huang marginal spectrum of the LES inner-surface temperature time series at the coordinate where the CUF in Fig. 4.29 is maximum. As the simulation time (~ 10 s) is less than the experiment time (120 s), analogies between the LES marginal spectrum and the experimental one



(a) New and old CUFs are calculated using the present and previous (that is, larger) Δt , respectively. The oldest CUF is related to $\Delta t = 0.15$ s. Start time $t_0 \approx 19.2$ s.

(b) New and old CUFs are calculated using the present and previous (that is, smaller) t_0 , respectively. The oldest CUF is related to $t_0 = 16.3$ s. $\Delta t = 0.05$ s.

Figure 4.30: ℓ^2 -norm of the difference between old and new CUFs.

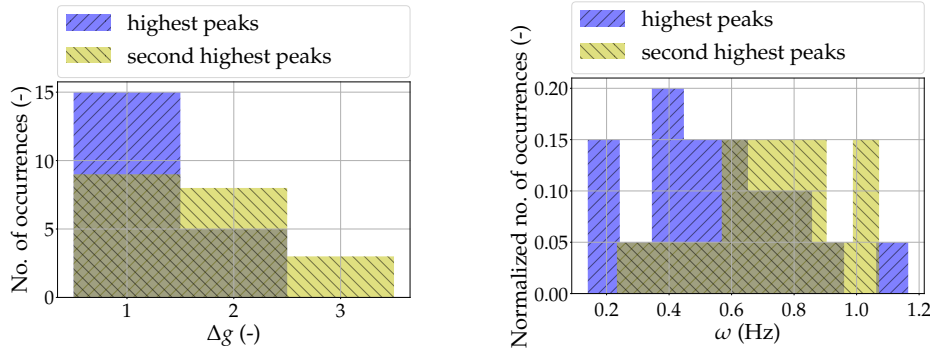


(a) LES spectra. Start time $t_0 = 19.2$ s.

(b) Experimental spectra. Full experiment time after low-pass filtering at 4 Hz.

Figure 4.31: Hilbert-Huang marginal spectra of LES and experimental inner-surface temperature time series at $(45^\circ, 0.67$ m).

in Fig. 4.31(b) are hardly drawn: for example, the highest peaks in the LES and experimental marginal spectra occur at 0.23 Hz and 0.04 Hz, respectively; hence, shorter timescales dominate the LES spectrum. However, the highest peaks in both marginal spectra stem from IMFs containing long timescales, next to the underlying trends: IMF g_8 contributes the most to the two highest peaks in the LES spectrum, while g_9 and g_8 contribute the most to the highest and second highest peaks in the experimental spectrum, respectively. In both cases, $c_0 = 10$.



(a) Δg associated with the two highest peaks in each spectrum. Δg is the number of IMFs in a time series after subtracting the index of the IMF that contributes the most to a specific peak.

(b) Frequencies at the two highest peaks in each spectrum. Occurrences are normalized to total 1.

Figure 4.32: Peaks in the Hilbert-Huang marginal spectra of 20 LES inner-surface temperatures from fatigue-prone areas. Start time $t_0 = 19.2$ s.

The Hilbert-Huang marginal spectra of the inner-surface temperature time series at the coordinate where the CUF in Fig. 4.29 is second highest are shown in Bergagio *et al.* (2018a). In essence, similarly to Fig. 4.31, the main contributors to the highest spectral peaks are long timescales, and the LES spectrum reveals sharper peaks than the experimental one, which instead exhibits smoother transitions between neighbor peaks. Once again, the dissimilarity may arise from the short simulation time.

The histograms in Fig. 4.32(a) show which IMFs contribute the most to the two highest spectral peaks in LES inner-surface temperature spectra from fatigue-prone areas. Here, 20 temperature time series are considered. Analogously to experimental inner-surface temperature spectra from locations with strong mixing inhomogeneity (see Fig. 4.19(b)), the IMFs generating the most prominent spectral peaks are near the upper bound of subset S ; in other terms, they evolve on the longest time scales, next to the underlying trend.

Fig. 4.32(b) reveals that the highest peaks in LES inner-surface temperature spectra from fatigue-prone areas surface between 0.2 and 0.6 Hz, while the second highest peaks in the aforesaid spectra lie between 0.6 and 1 Hz. However, considering the limited simulation time, it may reasonable to infer that dominant frequencies in LES inner-surface temperature spectra from fatigue-prone areas are 2-4 times the inverse of the simulation time. Correspondingly, dominant frequencies in experimental inner-surface temperature spectra from locations with strong mixing inhomogeneity are 3-7 times the inverse of the experiment time in Fig. 4.1(a) (left) – that is, 109.96 s.

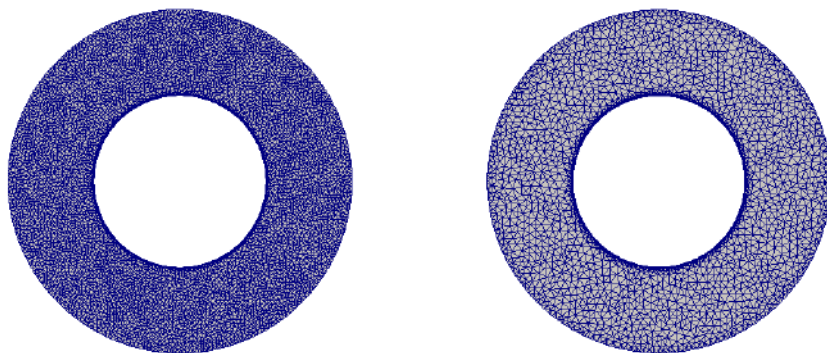


Figure 4.33: Meshes. Left: for the forward problem. Right: for the inverse problem (Cases 1.1 and 1.2).

4.6 IHCP

4.6.1 Test Problem 1

The spatial domain for Test Problem 1 is an annulus, whose inner and outer radii are 8×10^{-3} m and 16×10^{-3} m, respectively. λ in $\text{W m}^{-1} \text{K}^{-1}$ is determined from Eq. (4.2), with Y in K:

$$\lambda(Y) = 3 + 0.001(Y - 273) - 5 \times 10^{-6}(Y - 273)^2. \quad (4.2)$$

c in $\text{J kg}^{-1} \text{K}^{-1}$ is determined from Eq. (4.3), with Y in K:

$$c(Y) = 262.2 - 0.004(Y - 273) - 1 \times 10^{-4}(Y - 273)^2. \quad (4.3)$$

Concerning the forward problem in Eqs. (3.35a) - (3.35d), similarly to Reinhardt *et al.* (2007), heat transfer coefficient \hat{h} is given in $\text{W m}^{-2} \text{K}^{-1}$ as

$$\hat{h}(\theta) = \begin{cases} 10 & \text{if } 0^\circ \leq \theta < 40^\circ & (4.4a) \\ 4.8\theta - 182 & \text{if } 40^\circ \leq \theta < 90^\circ & (4.4b) \\ 682 - 4.8\theta & \text{if } 90^\circ \leq \theta < 140^\circ & (4.4c) \\ 10 & \text{if } 140^\circ \leq \theta \leq 180^\circ. & (4.4d) \end{cases}$$

Here, θ is given in degrees. \hat{h} is symmetric about the x -axis. Moreover, $Y_\infty = 313$ K, $\tilde{Y} = Y_u = 273$ K, and $\rho = 10\,000$ kg m^{-3} .

The meshes for the forward and inverse problems are shown in Fig. 4.33. The average cell size amounts to 9.65×10^{-8} m^2 , while time step Δt equals 8.86×10^{-3} s. Standard deviation ξ (see Section 3.7) is 1.0 in Case 1.1 and 0.1 in Case 1.2. Similarly to Lu *et al.* (2012), the inverse problem is solved on a coarser mesh to avoid

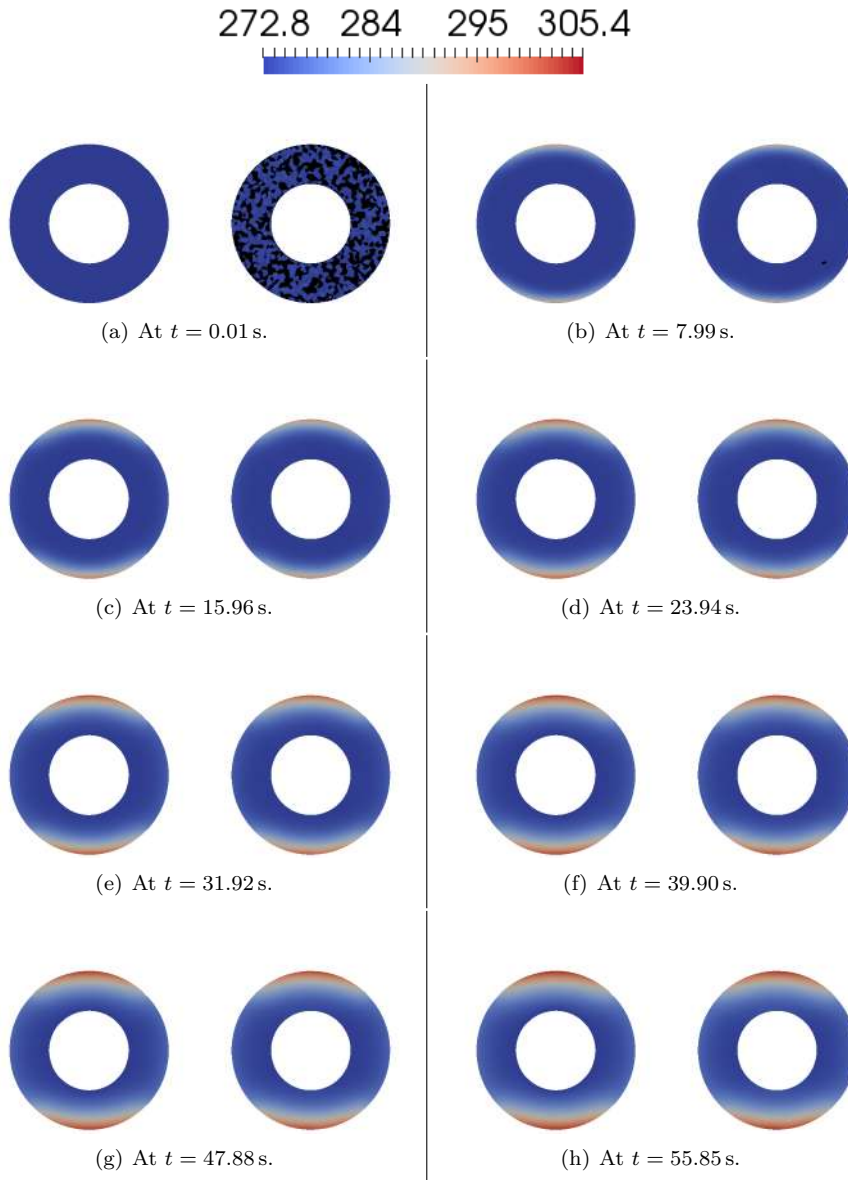


Figure 4.34: Temperature distributions. Left of each subfigure: for the forward problem; that is, Y . Right of each subfigure: for the inverse problem (Case 1.1); specifically, T at $k = 11$. Temperatures are in K. $T < \min_{(\mathbf{x},t) \in (\Omega, \mathcal{T})} Y$ in the black zones. $t_{\max} = 80$ s. T at $t \geq 64$ s is ignored.

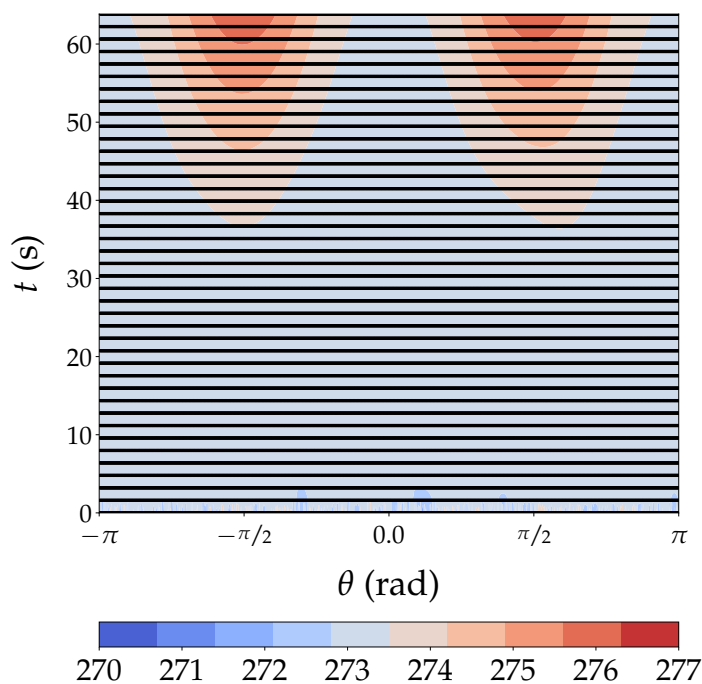


Figure 4.35: Temperature T_u (Case 1.1) at $k = 11$. Temperatures are in K. $t_{\max} = 80$ s. T at $t \geq 64$ s is ignored.

committing inverse crimes (Kaipio and Somersalo (2005)), which can appear if the same discretization and numerical model are adopted for the direct and inverse problems. Consequently, the inverse problem becomes less ill-posed than it actually is. Perturbing Y and \tilde{Y} with Gaussian noise helps to mitigate inverse crimes.

Case 1.1 is analyzed here. The while loop in Algorithm 1 stops when $k = 11$. Fig. 4.34 presents temperature Y from the direct problem and temperature T_{11} from the inverse problem side by side, at illustrative times. The heated zones from the IHCP and those from the DHCP show analogous sizes and shapes even when t reaches t_f , with $t_f = 64$ s. Furthermore, Fig. 4.34 hints that Y qualitatively agrees with T_{11} , at all times examined. Notwithstanding, the black zones are characterized by $T < \min_t Y$, given that Gaussian noise is added to the initial condition. These black zones quickly vanish, paving the way for a fairly even temperature distribution – see Fig. 4.34(c) and video `Case_1.1/Case_1.1_vid.mp4` (Bergagio (2018b)).

Fig. 4.35 shows temperature T_{11} on Γ_u , where the heat flux is unknown. T_{11} , which should equal $\tilde{Y} = Y_u = 273$ K, is saved at 1000 polar angles and 41 times. In Fig. 4.35, all sampling times are indicated by black lines. As previously stressed,

adding Gaussian noise (in this case, $\xi = 1.0$) to initial and boundary conditions creates small areas where $T_{u,11} < 273$ K; in other terms, it barely alters temperatures on Γ_u at $t \rightarrow 0$. The approach suggested here seems to correctly predict T_u up to $t \approx 40$ s. At later times, errors increase near $\theta = \pm\pi/2$, where most heating of boundary Γ_g occurs. In any case, error $\max |Y_u - T_{u,11}|$ over all polar angles, for times smaller than t_f , barely exceeds 3 K (that is, 8.5% of the temperature range).

The instantaneous error at time t and iteration k

$$\varepsilon_k = \sqrt{\frac{\int_{\Omega} (T_k - Y)^2 d\Omega}{\int_{\Omega} Y^2 d\Omega}} \quad (4.5)$$

together with the time-integrated error at iteration k

$$\eta_k = \sqrt{\frac{\int_0^{t_f} \int_{\Omega} (T_k - Y)^2 d\Omega dt}{\int_0^{t_f} \int_{\Omega} Y^2 d\Omega dt}}. \quad (4.6)$$

can help to clarify inconsistencies between temperatures T and Y . Fig. 4.36 illustrates the variation of the instantaneous error from Eq. (4.5) over time t at $k = 2, 7,$ and 11 . This error appears to reduce if k increases. The maximum error at $k = 11$ is 0.2%, which is reasonable. Fig. 4.36 also shows that, in Test Problem 1, γ grows with k . Regularization appears to improve temperature at $k = 11$; therefore, Eq. (3.44) seems to give suitable regularization parameters. Furthermore, if $\xi = 1.0$ and γ is omitted, η_{11} from Case 1.1 would be reached after more than 25 iterations; consequently, the regularization parameter from Eq. (3.44) seems to speed up convergence. The existing literature – see, e.g., Reinhardt *et al.* (2007) – emphasizes that a blend of Eq. (3.38b) and the initial guess $q_{u,0}$ leads to error growth at $t \rightarrow t_{\max}$. Figs. 4.35 and 4.36 indicate that the choice of t_f could appreciably impact on error estimators.

Fig. 4.37 shows how the difference between volume-averaged temperatures in Cases 1.1 ($\xi = 1.0$) and 1.2 ($\xi = 0.1$) changes over time t . This difference appears to be small, at any time. Fig. 4.37 seems to confirm that regularization decreases the noise in the initial and boundary conditions. Thus, it proves the strength of this approach to noise. The caption highlights that temperatures at $k = 11$ are considered in both cases, although $k = 12$ should be preferred in Case 1.2 because here the last iteration is $k = 12$, not $k = 11$ as in Case 1.1. Despite that, the choice falls on $k = 11$, since $\eta_{11} < \eta_{12}$, η being given by Eq. (4.6); namely, $\eta_{11} = 1.701 \times 10^{-3}$, whereas $\eta_{12} = 1.704 \times 10^{-3}$. This disagreement between η and stopping criterion suggests that either the former should be calculated differently – perhaps using the H^1 -norm – or the latter requires some amendment.

4.6.2 Test Problem 2

In this problem, Case 1 from Table 3.3 is considered. Here, concerning thermal properties of 316L stainless steel, $\rho = 7900$ kg m⁻³, while λ and c are taken from

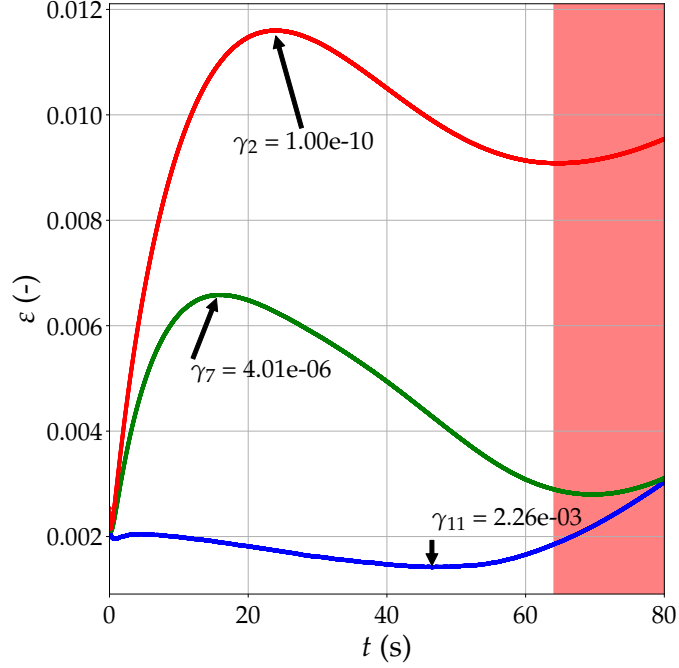


Figure 4.36: Instantaneous error with respect to iteration number and time. γ is in $\text{K}^2 \text{m}^4 \text{W}^{-2}$. Case 1.1. Errors in the red region ($t_f \leq t \leq t_{\max}$) are ignored.

database MPDB (Software Inc. (2015)).

In the DHCP (i.e., Eqs. (3.35a) - (3.35d)), $\hat{h} = 0$ (adiabaticity), while temperatures \tilde{Y} and Y_u are read from an LES on a mildly refined mesh – see Section 3.6.6.

They are sampled at $z = 0.65 \text{ m}$; i.e., on the xy -plane in Fig. 3.13(c). Test Problem 2 is solved on the gray cross section. \tilde{Y} and Y_u are sampled in the inner tube and at the interface between water and inner tube, respectively. Both of them are sampled from $t = 0$ to $t = t_{\max}$, with t_{\max} reaching 10 s. The sampling frequency approaches 4.16 Hz for $t \rightarrow t_{\max}$. Temperature changes rapidly during this transient, which makes it suitable for testing the performance of the algorithm implemented here.

As Fig. 3.15(b) implies, solving the IHCP allows to approximate temperatures on Γ_u ; i.e., on the interface between water and inner tube. Γ_u is longer than Γ_g , which complicates the problem under study even further, since the subtle details of the reconstructed temperature distribution on Γ_u are inevitably lost. However, solving Test Problem 2 is of paramount importance in nuclear applications, where

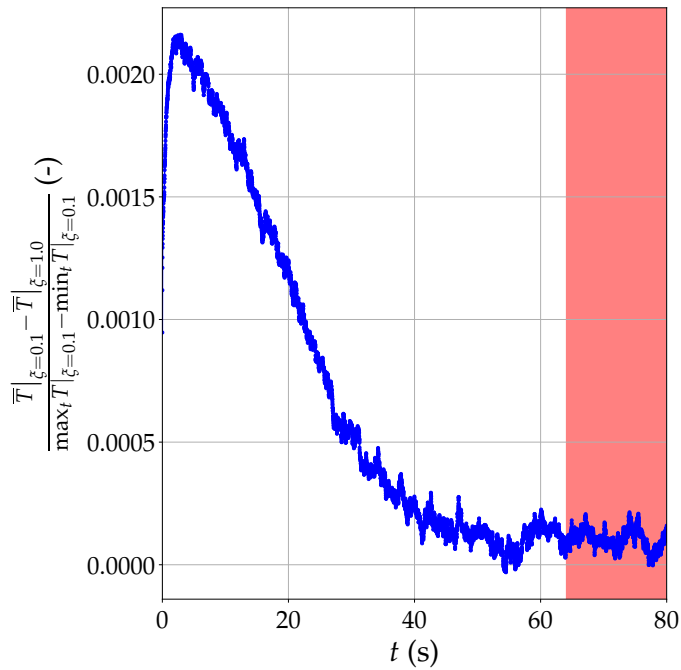


Figure 4.37: Difference between non-dimensional volume-averaged temperatures in Cases 1.1 ($\xi = 1.0$) and 1.2 ($\xi = 0.1$). $k = 11$ in both cases. Differences in the red region ($t_f \leq t \leq t_{\max}$) are ignored.

Table 4.5: Key parameters in the cases considered. Test Problem 2.

Case no.	Mesh size	Average cell size (m ²)	Segments on Γ_g	Segments on Γ_u	Δt (s)
2.1	Fine	9.43×10^{-8}	1000	400	8.9×10^{-4}
2.2	Medium	1.08×10^{-7}	900	360	1.1×10^{-3}
2.3	Coarse	1.27×10^{-7}	800	320	1.4×10^{-3}

drilling into the walls of structures subjected to high internal pressure to determine the inner-surface temperature is forbidden. Three cases are examined; namely, 2.1 (fine mesh), 2.2 (medium mesh), and 2.3 (coarse mesh). In these three cases, $t_f = 8$ s and $\xi = 0.1$. Key mesh parameters and time steps are summarized in Table 4.5.

Case 2.1 is analyzed here. The while loop in Algorithm 1 stops when $k = 3$, so Test Problem 1 required more iterations to converge. Fig. 4.38 presents temperature Y from the direct problem and temperature T_3 from the inverse problem side by side, at illustrative times. Comparably to Fig. 4.34, the heated zones from the IHCP and those from the DHCP show analogous shapes and sizes, even for $t \rightarrow t_f$; therefore, Y qualitatively agrees with T_3 , at all times examined in Fig. 4.38. Adding Gaussian noise to initial condition \tilde{Y} and boundary conditions on Γ_g does not produce easily noticeable black zones as in Fig. 4.34, since ξ falls below that in Case 1.1. Actually, temperature $\min_t Y$ in Fig. 4.38(a) is higher than T_3 on two nodes in the vicinity of Γ_u , as can be observed by carefully contrasting temperatures in folder `Case_2.1/DHCP` with those in `Case_2.1/3` (Bergagio (2018b)). The heating process is detailed in video `Case_2.1/Case_2.1_vid.mp4` (Bergagio (2018b)). It is worth noting that regularization parameter γ is not set according to Eq. (3.44) in Cases 2.1, 2.2, and 2.3; instead, γ is set to $1 \times 10^{-10} \text{ K}^2 \text{ m}^4 \text{ W}^{-2}$. The effectiveness of the fixed-point method from Viloche Bazán (2008) is now being investigated; if this technique proves ineffective, more appropriate methods for computing γ in this type of nonlinear problem should be applied instead. It is worth stressing that, in a non-regularized problem, $\mathcal{J}'(q_{u,k}(\mathbf{x}, t_{\max})) = 0$ (see Eqs. (3.37) and (3.38b)); therefore, $\hat{p}_k(\mathbf{x}, t_{\max}) = 0$ (see Eqs. (3.43a) and (3.43b)), which implies that $q_{u,k}(\mathbf{x}, t_{\max})$ cannot be updated based on Eq. (3.45); that is, the selection of initial guess $q_{u,0}(\mathbf{x}, t_{\max})$ has to be carefully thought over. The difficulty can be circumvented by, e.g., examining Sobolev space H^1 . This and other alternatives are explored in Bourquin and Nassiopoulos (2011).

Temperatures Y_u and T_3 on Γ_u are presented in Fig. 4.39. Temperatures are saved at 400 polar angles and 41 times. All sampling times are indicated by black lines, analogously to Fig. 4.35. As in Test Problem 1, the initial stages of the heating process appear better reproduced: altogether, the method implemented here seems to correctly predict T_u up to $t \approx 5$ s. At later times, smoothed temperature fields delay heating in areas around $\theta = \pm\pi/2$. Nevertheless, error $\max |Y_u - T_{u,3}|$ over all polar angles, for times smaller than t_f , is observed at the very start of the heating; namely, at $(\theta, t) = (-2.12 \text{ rad}, 0.4 \text{ s})$. This error equals 24.75 K, or 19.7% of the temperature range.

A mesh independence study is shown in Fig. 4.40. Here, time-integrated error η from Eq. (4.6) is represented as a function of iteration number k , in Cases 2.1, 2.2, and 2.3. In these cases, the stopping criterion is met at $k = 3$, when η reaches its minimum value. Accordingly, differently from Case 1.2, stopping criterion and η appear perfectly matched here. In order to demonstrate that $\min_k \eta$ is attained at $k = 3$, η at $k = 4$ and 5 is included in Fig. 4.40. The lowest η is returned in Case 2.1 (fine mesh), while the next-to-lowest η comes from Case 2.2 (medium mesh).

Nevertheless, $\eta \approx 8 \times 10^{-3}$ in Cases 2.1, 2.2, and 2.3, which backs the effectiveness of the method implemented here.

Since T and ϕ (i.e., the solution to the dual problem) are to be saved on the whole space domain at every time t , the mesh should be refined only where strictly necessary; here, it can be adaptively refined according to error estimators for goal functionals of interest. To this purpose, ϕ can be merged into the error representation, analogously to the method applied to a 2D steady-state IHCP in Li *et al.* (2011).

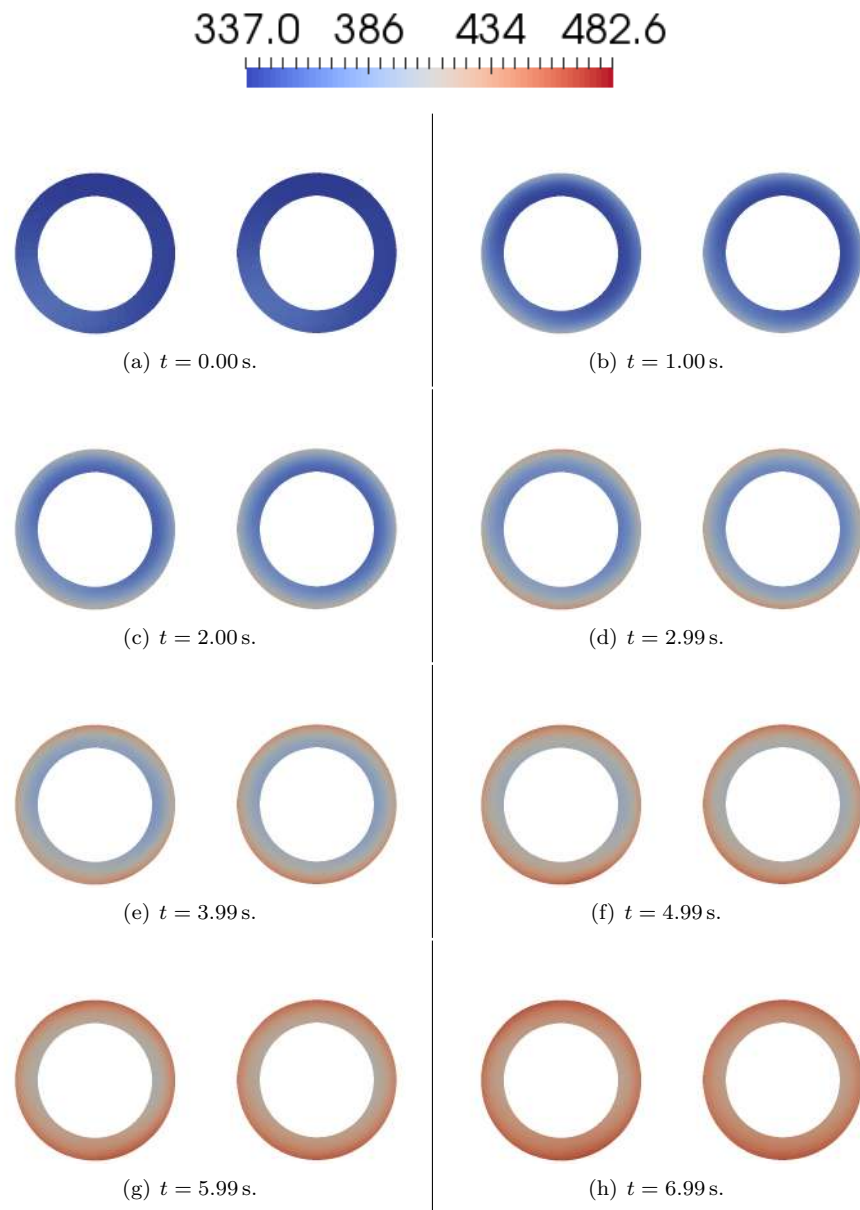


Figure 4.38: Temperature distributions. Left of each subfigure: for the forward problem; that is, Y . Right of each subfigure: for the inverse problem (Case 2.1); specifically, T at $k = 3$. Temperatures are in K. $t_{\max} = 10$ s. T at $t \geq 8$ s is ignored.

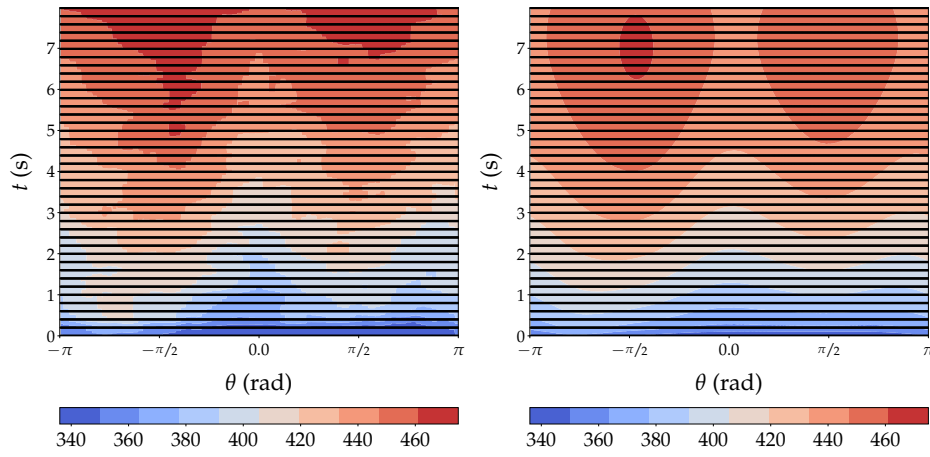


Figure 4.39: Left: temperature Y_u . Right: temperature T_u (Case 2.1) at $k = 3$. Temperatures are in K. $t_{\max} = 10$ s. T at $t \geq 8$ s is ignored.

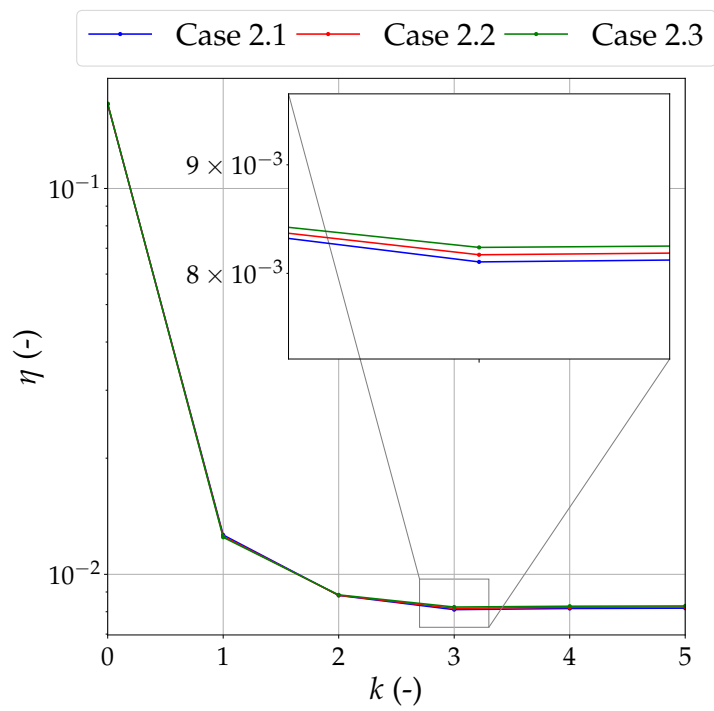


Figure 4.40: Time-integrated errors in Cases 2.1 (fine mesh), 2.2 (medium mesh), and 2.3 (coarse mesh). The inset depicts the above errors at the iteration when the stopping criterion is met and the time-integrated error reaches its minimum value. The stopping criterion does not end the while loop here.

Chapter 5

Conclusions and outlook for future work

5.1 Conclusions

Experiments and simulations of mixing in a vertical annulus between two stainless steel tubes have been performed under BWR conditions ($\Delta T = 216\text{ K}$, $p = 7.2\text{ MPa}$). In the annulus, turbulent mixing of cold water flowing upwards and hot water flowing downwards occurs. Cold water enters the annulus through two inlets facing each other at $z = 0.15\text{ m}$, while hot water enters the annulus through two inlets facing each other at $z = 0.80\text{ m}$, at 90° from the cold inlets.

Temperatures measured at the inner radius of the above annulus are called inner-surface temperature time series and suggest extensive mixing, if they exhibit periodic, commensurate oscillations; incipient mixing, if they present abrupt peaks; or no mixing, if they are nearly constant during the experiment time.

In all experimental cases, incipient mixing is found at $z \geq 0.60\text{ m}$. Altogether, the axial level at which mixing is most nonuniform, along with ranges and variances of inner-surface temperatures there, appears determined by two factors: (1) thermal stratification, which intensifies with higher ΔT ; and (2) penetration of hot flow structures into the annulus, which increases if higher mass fluxes enter the hot inlets. Thermal stratification amplifies the highest mixing non-uniformity, probably because large axial inner-surface temperature gradients weaken mixing uniformity. The penetration of hot flow structures lowers the inner-surface area where low-frequency, high-amplitude fluctuations prevail.

With comparably small hot mass flow rates, these two factors compete: thermal stratification is supposed to spread less extensive mixing over several axial levels, whereas the reduced penetration of hot flow structures is supposed to concentrate this mixing into fewer levels.

The correlation between inner-surface temperatures from the same thermocouple disc, together with the similarity in ranges, means, and dominant frequencies

among inner-surface temperatures at the same measurement position, justifies joining the standard deviations of inner-surface temperatures at a given measurement position into one scalar estimating mixing inhomogeneity. The suggested estimator appears to gauge mixing inhomogeneity in an acceptable way. At a specific z , with high hot mass flow rates, mixing inhomogeneity appears weaker at 180° than at 360° .

The inner-surface temperature time series are typically non-stationary and intermittent in the mixing region. A Hilbert-Huang spectral analysis allows to identify their dominant frequencies because conventional spectral methods are not suited to this end.

At measurement positions with the highest mixing inhomogeneity, inner-surface temperatures fall below adiabatic mixing temperatures and exhibit more pronounced spectral peaks than their axial neighbors. Dominant frequencies range between 0.03 and 0.10 Hz. This band seems widened by higher hot mass flow rates. Dominant frequencies in the Fourier spectra of the same temperatures span a wider band. The above spectral peaks are often due to IMFs evolving on the longest time scales. Parameter $\hat{\delta}$ retains these IMFs in the detrended time series; therefore, $\hat{\delta}$ is crucial for recognizing dominant frequencies.

The uncertainty of inner-surface temperature measurement equals 1.58 K at 1000 Hz and 3.87 K at 100 Hz.

The above mixing has been simulated using LES. The total simulation time is about 10 s. Velocities and temperatures at the inlets, along with pressure, match those from the aforesaid experiments. There appears to be reasonable agreement between LES and experimental inner-surface temperatures in relation to local variances, ranges, time-averaged values at specific axial levels, and IMFs generating dominant spectral peaks at fatigue-prone locations. Both LES and experimental dominant frequencies in the inner-surface temperature spectra at the locations at hand fall below ten times the inverse of the respective time intervals.

Ranges, mean values, and variances of LES inner-surface temperatures are more azimuthally symmetric than their experimental counterparts. Reasons behind this incongruity may include geometry flaws in the HWAT test section, its deformation under thermal loads, and more dissimilar temperatures and velocities at each inlet pair than supposed in the LES.

In the current simulation, intense mixing inhomogeneity involves lower axial levels at 90° and 270° than at 180° and 360° , most likely (1) because hotter vortices moving downwards carry higher momentum water there; or (2) because colder, upright vortices traveling upwards cause more dissipation of kinetic energy there than the 2D structures at 180° and 360° usually do, for the same z .

An FEA of the inner tube under LES pressure and thermal loads has been conducted. Time-averaged hoop stresses are one order of magnitude smaller than time-averaged axial stresses: comparably to mixing tees, (1) the “stripe constraint” (Miyoshi *et al.* (2014); Kamaya and Miyoshi (2017)) outweighs the “circumferential constraint”, and (2) hoop and axial stresses exhibit wider ranges at locations with higher mixing inhomogeneity.

Fatigue damage has been assessed in a part of the inner tube ($0.60 \text{ m} \leq z \leq 1.00 \text{ m}$) from the FEA stress history. The highest CUFs emerge in small spots where mixing inhomogeneity is maximum. Cracking is predicted to initiate after 97h. The mesh has to be fine enough to identify fatigue-susceptible areas.

A robust, accurate technique has been implemented for solving transient IHCPs on 2D domains when no *a priori* information on noise type and statistics is available. An adjoint CGM coupled to Tikhonov regularization has been adopted to this end. Two test problems help to verify the accuracy of the above technique. The solutions to the IHCPs agree qualitatively with those to the DHCPs, even when time tends to t_f . The reconstructed temperature on unreachable boundaries appears less accurate over strongly heated areas, when time tends to 0 or exceeds $t_{\max}/2$. Noise perturbation of initial and boundary conditions for the IHCPs allows to verify the robustness of the technique implemented here. While the fixed-point strategy for tuning the regularization parameter seems adequate in cases from Test Problem 1, it appears unsatisfactory in cases from Test Problem 2. One case from Test Problem 1 reveals a discrepancy between η and CGM stopping criterion.

5.2 Outlook for future work

The vast amount of LES data can be used to study thermal stratification and natural convection; explore the connection between power spectra of temperature and axial velocity in the near-wall region; estimate heat transfer coefficients at the inner surface; and compute radial heat fluxes in the inner tube. Other SGS models can be investigated. As y^+ is deemed high near $z = 0.80 \text{ m}$, finer meshes can be tested. However, time steps should be reduced accordingly, so a DES approach can be favored to save computational time.

The uncertainty at 100 Hz can be trimmed down by measuring appropriate end-to-end calibration data: while the largest uncertainty source at 100 Hz stems from manufacturer's data, the same uncertainty source at 1000 Hz arises from end-to-end calibration data.

Postprocessing of LES and experimental data can be improved by overcoming the mode mixing issue and by comparing the HHT with more conventional time-frequency analysis methods, including wavelets.

The fatigue damage assessment can be enhanced by building an FEA mesh that matches the LES one and by adding environmental fatigue life correction factors (Fen) together with plasticity effects.

Concerning the algorithm for solving IHCPs, efficiency and effectiveness of several techniques for deriving the regularization parameter should be benchmarked. Other stabilizing functionals can be tested. The method implemented here can be generalized to 3D cases and multiply-connected domains. The mesh can be adaptively refined based on some *a posteriori* error indicator. Hilbert-Huang marginal spectra of exact and reconstructed temperatures can be checked for correlation.

Bibliography

- R. Abou Khachfe and Y. Jarny. 2000. Numerical solution of 2-D nonlinear inverse heat conduction problems using finite-element techniques. *Numerical Heat Transfer, Part B: Fundamentals*, 37(1).
- Y. Addad, U. Gaitonde, D. Laurence, and S. Rolfo. 2008. Optimal Unstructured Meshing for Large Eddy Simulations. *Quality and Reliability of Large-Eddy Simulations*, 12:93–103.
- T. Alexandrov, S. Bianconcini, E.B. Dagum, P. Maass, and T.S. McElroy. 2012. A review of some modern approaches to the problem of trend extraction. *Econometric Reviews*, 31(6):593–624.
- O.M. Alifanov. 1974. Solution of an inverse problem of heat conduction by iteration methods. *Journal of Engineering Physics and Thermophysics*, 26(4):471–476.
- O.M. Alifanov. 1994. *Inverse heat transfer problems*. International Series in Heat and Mass Transfer. Springer. ISBN 978-3-642-76436-3.
- M. Alnæs, J. Blechta, J. Hake, A. Johansson, B. Kehlet, A. Logg, C. Richardson, J. Ring, M.E. Rognes, and G.N. Wells. 2015. The FEniCS project version 1.5. *Archive of Numerical Software*, 3(100):9–23.
- K. Angele, Y. Odemark, M. Cehlin, B. Hemström, C.M. Högström, M. Henriksson, H. Tinoco, and H. Lindqvist. 2011. Flow mixing inside a control-rod guide tube - Experimental tests and CFD simulations. *Nuclear Engineering and Design*, 241(12):4803–4812.
- H. Anglart, M. Bergagio, S. Hedberg, S. Rydström, and W. Frid. 2015. Measurement of wall temperature fluctuations during thermal mixing of non-isothermal water streams. In *Proceedings of the 16th International Topical Meeting on Nuclear Reactor Thermal Hydraulics*, volume 1, pages 807–818.
- W. Aquino and J.C. Brigham. 2006. Self-learning finite elements for inverse estimation of thermal constitutive models. *International Journal of Heat and Mass Transfer*, 49(15):2466–2478.
- ASME. 2015a. *ASME Boiler & Pressure Vessel Code 2015 - Section III, Appendices*.

- ASME. 2015b. *ASME Boiler & Pressure Vessel Code 2015 - Section III, Division 1*.
- H. Ayhan and C.N. Sökmen. 2012. CFD modeling of thermal mixing in a T-junction geometry using LES model. *Nuclear Engineering and Design*, 253:183–191.
- J.V. Beck, B. Blackwell, and C.R. St. Clair Jr. 1985. *Inverse Heat Conduction: Ill-Posed Problems*. Wiley-Interscience. ISBN 0-471-08319-4.
- A. Belmiloudi and F. Mahé. 2014. On nonlinear inverse problems of heat transfer with radiation boundary conditions: Application to dehydration of gypsum plasterboards exposed to fire. *Advances in Numerical Analysis*, 2014:1–18.
- M. Bergagio. 2018a. Large eddy simulation of thermal mixing under boiling water reactor conditions, Mendeley Data, v1.
- M. Bergagio. 2018b. Two-dimensional nonlinear inverse heat conduction problem, Mendeley Data, v1.
- M. Bergagio and H. Anglart. 2017. Experimental investigation of mixing of non-isothermal water streams at BWR operating conditions. *Nuclear Engineering and Design*, 317:158–176.
- M. Bergagio, W. Fan, R. Thiele, and H. Anglart. 2018a. Large eddy simulation of thermal mixing with conjugate heat transfer at BWR operating conditions. Submitted to *Nuclear Engineering and Design*.
- M. Bergagio, S. Hedberg, S. Rydström, and H. Anglart. 2015. Instrumentation for temperature and heat flux measurement on a solid surface under BWR operating conditions. In *Proceedings of the 16th International Topical Meeting on Nuclear Reactor Thermal Hydraulics*, volume 7, pages 5962–5975.
- M. Bergagio, H. Li, and H. Anglart. 2018b. An iterative finite-element algorithm for solving two-dimensional nonlinear inverse heat conduction problems. *International Journal of Heat and Mass Transfer*, 126:281–292.
- M. Bergagio, R. Thiele, and H. Anglart. 2017. Analysis of temperature fluctuations caused by mixing of non-isothermal water streams at elevated pressure. *International Journal of Heat and Mass Transfer*, 104:979–992.
- S. Bergholz and F. Bruckmueller. 2012. AREVA Fatigue Concept (AFC). Live demonstration of a modern fatigue monitoring system FAMOS i. In *Annual Meeting on Nuclear Technology*.
- R.B. Bird, W.E. Stewart, and E.N. Lightfoot. 2007. *Transport Phenomena*. John Wiley & Sons.

- F. Bourquin and A. Nassiopoulou. 2011. Inverse reconstruction of initial and boundary conditions of a heat transfer problem with accurate final state. *International Journal of Heat and Mass Transfer*, 54(15-16):3749–3760.
- F. Bozzoli, L. Cattani, S. Rainieri, F.S. Viloche Bazán, and L.S. Borges. 2014. Estimation of the local heat-transfer coefficient in the laminar flow regime in coiled tubes by the Tikhonov regularisation method. *International Journal of Heat and Mass Transfer*, 72:352–361.
- O. Braillard and D. Edelin. 2009. Advanced experimental tools designed for the assessment of the thermal load applied to the mixing tee and nozzle geometries in the PWR plant. In *First International Conference on Advancements in Nuclear Instrumentation Measurement Methods and their Applications (ANIMMA), 2009*, pages 1–7.
- A. Cebula and J. Taler. 2014. Determination of transient temperature and heat flux on the surface of a reactor control rod based on temperature measurements at the interior points. *Applied Thermal Engineering*, 63(1):158–169.
- S. Chapuliot, C. Gourdin, T. Payen, J.P. Magnaud, and A. Monavon. 2005. Hydrothermal-mechanical analysis of thermal fatigue in a mixing tee. *Nuclear Engineering and Design*, 235(5):575–596.
- M.-S. Chen, H.-E. Hsieh, Y.-M. Ferng, and B.-S. Pei. 2014. Experimental observations of thermal mixing characteristics in T-junction piping. *Nuclear Engineering and Design*, 276:107–114.
- M.J. Ciałkowski, A. Frąckowiak, and K. Grysa. 2007. Solution of a stationary inverse heat conduction problem by means of Trefftz non-continuous method. *International Journal of Heat and Mass Transfer*, 50(11):2170–2181.
- P. Cladé. 2010. PyDAQmx: a Python interface to the National Instruments DAQmx driver. <https://github.com/clade/PyDAQmx>. Online; accessed 30 September 2018.
- O. Costa Garrido, S. El Shawish, and L. Cizelj. 2015. Stress assessment in piping under synthetic thermal loads emulating turbulent fluid mixing. *Nuclear Engineering and Design*, 283:114–130.
- M. Dahlberg, K.F. Nilsson, N. Taylor, C. Faigy, U. Wilke, S. Chapuliot, D. Kalkhof, I. Bretherton, J.M. Church, J. Solin, *et al.* 2007. Development of a European procedure for assessment of high cycle thermal fatigue in light water reactors. *Final Report of the NES-C-Thermal Fatigue Project. EUR*, 22763.
- I. Daubechies, M. Defrise, and C. De Mol. 2004. An iterative thresholding algorithm for linear inverse problems with a sparsity constraint. *Communications on pure and applied mathematics*, 57(11):1413–1457.

- S. Deng and Y. Hwang. 2007. Solving the temperature distribution field in nonlinear heat conduction problems using the Hopfield neural network. *Numerical Heat Transfer, Part B: Fundamentals*, 51(4):375–389.
- B.H. Dennis and G.S. Dulikravich. 2012. Inverse determination of unsteady temperatures and heat fluxes on inaccessible boundaries. *Journal of Inverse and Ill-posed Problems*, 20:791–803.
- N.S. Dhamankar, G.A. Blaisdell, and A.S. Lyrintzis. 2015. An Overview of Turbulent Inflow Boundary Conditions for Large Eddy Simulations (Invited). In *22nd AIAA Computational Fluid Dynamics Conference*. American Institute of Aeronautics and Astronautics.
- P.E. Dimotakis. 2005. Turbulent mixing. *Annual Review of Fluid Mechanics*, 37:329–356.
- K. Dussarlapudi, B.K. Nashine, D. Bai, and C.S. Babu. Simulation of fast response thermocouple for the nuclear reactor core. In *Proceedings of the 2011 COMSOL Conference*.
- C. Eckart. 1948. An analysis of the stirring and mixing processes in incompressible fluids. *J. mar. Res.*, 7(3):265–275.
- K. El Omari and Y. Le Guer. 2010. Alternate rotating walls for thermal chaotic mixing. *International Journal of Heat and Mass Transfer*, 53(1-3):123–134.
- DTU Wind Energy. 2016. WindEnergyToolbox. Collection of HAWC2, HAWC-Stab2 tools etc from DTU Wind Energy. <https://gitlab.windenergy.dtu.dk/toolbox/WindEnergyToolbox>. Online; accessed September 3, 2018.
- C. Faidy, T. Courtois, E. Fraguier, J. Leduff, A. Lefrancois, and J. Dechelotte. 2000. Thermal fatigue in French RHR system. In *International Conference on Fatigue of Reactor Components, Napa, CA*.
- Farley. 1987. Unit Shut Down due to Pressure Boundary Leakage. Licensee Event Report 364-87-10-01.
- A. Fissolo, S. Amiable, O. Ancelet, F. Mermaz, J.M. Stelmaszyk, A. Constantinescu, C. Robertson, L. Vincent, V. Maillot, and F. Bouchet. 2009. Crack initiation under thermal fatigue: An overview of CEA experience. Part I: Thermal fatigue appears to be more damaging than uniaxial isothermal fatigue. *International Journal of Fatigue*, 31(3):587 – 600.
- M.G. Frei and I. Osorio. 2007. Intrinsic time-scale decomposition: time–frequency–energy analysis and real-time filtering of non-stationary signals. In *Proceedings of the Royal Society of London A: Mathematical, Physical and Engineering Sciences*, volume 463, pages 321–342. The Royal Society.

- A. Frąckowiak, J. von Wolfersdorf, and M. Cialkowski. 2015. An iterative algorithm for the stable solution of inverse heat conduction problems in multiply-connected domains. *International Journal of Thermal Sciences*, 96:268–276.
- N. Fukushima, K. Fukagata, N. Kasagi, H. Noguchi, and K. Tanimoto. 2003. Numerical and experimental study on turbulent thermal mixing in a T-junction flow. In *The 6th ASME-JSME Thermal Engineering Joint Conference*, pages 16–20.
- I. Gallego-Marcos. 2013. Thermal Mixing CHT Simulations with OpenFOAM: URANS and LES. Master's thesis, KTH Royal Institute of Technology.
- P. Gauder, P. Karthick Selvam, R. Kulenovic, and E. Laurien. 2016. Large eddy simulation studies on the influence of turbulent inlet conditions on the flow behavior in a mixing tee. *Nuclear Engineering and Design*, 298:51–63.
- M.R. Golbahar Haghighi, M. Eghtesad, and P. Malekzadeh. 2008. A coupled differential quadrature and finite element method for 3-D transient heat transfer analysis of functionally graded thick plates. *Numerical Heat Transfer, Part B: Fundamentals*, 53(4):358–373.
- S.R. Gosselin, Simonen F.A., Heasler P.G., and Doctor S.R. 2007. *Fatigue Crack Flaw Tolerance in Nuclear Power Plant Piping: A Basis for Improvements to ASME Code Section XI Appendix L*. US Nuclear Regulatory Commission, Office of Nuclear Regulatory Research, Division of Fuel, Engineering and Radiological Research.
- M. Green and C.G. Ferrari. 2016. Desarrollo de un Procedimiento de Cálculo de Fatiga Multiaxial según ASME Sección III Incluyendo la Metodología Fen. In *Mecánica Computacional Vol XXXIV*, pages 1753–1772 (in Spanish).
- K. Grysa. 2003. Heat polynomials and their applications. *Archives of Thermodynamics*, 24(2):107–124.
- Z. Guo, J. Zou, Y. Chen, K. Xu, and T. Lu. 2017. Online monitoring of wall temperature fluctuations of horizontal mixing T-junction pipe. *Applied Thermal Engineering*, 127:580–591.
- D. Haces Manzano. 2013. U-RANS and LES conjugate heat transfer analysis of the thermal fluctuations in a high difference temperature mixing zone using OpenFOAM. Master's thesis, KTH Royal Institute of Technology.
- A. Haji-Sheikh and F.P. Buckingham. 1993. Multidimensional inverse heat conduction using the Monte Carlo method. *J. Heat Transfer*, 115:26–33.
- M.H.C. Hannink and F.J. Blom. 2011. Numerical methods for the prediction of thermal fatigue due to turbulent mixing. *Nuclear Engineering and Design*, 241(3):681–687.

- P.C. Hansen and D.P. O’Leary. 1993. The use of the L-curve in the regularization of discrete ill-posed problems. *SIAM Journal on Scientific Computing*, 14(6): 1487–1503.
- F. Hecht. 2012. New development in FreeFem++. *J. Numer. Math.*, 20(3-4): 251–265.
- Y. Heng, S. Lu, A. Mhamdi, and S.V. Pereverzev. 2010. Model functions in the modified L -curve method – case study: the heat flux reconstruction in pool boiling. *Inverse Problems*, 26(5):055006.
- L.-W. Hu and M.S. Kazimi. 2006. LES benchmark study of high cycle temperature fluctuations caused by thermal striping in a mixing tee. *International Journal of Heat and Fluid Flow*, 27(1):54–64.
- C.-H. Huang and C.-C. Tsai. 1998. An inverse heat conduction problem of estimating boundary fluxes in an irregular domain with conjugate gradient method. *Heat and Mass Transfer*, 34(1):47–54.
- N. E. Huang, Z. Shen, S. R. Long, M. C. Wu, H. H. Shih, Q. Zheng, N.-C. Yen, C. C. Tung, and H. H. Liu. 1998. The empirical mode decomposition and the Hilbert spectrum for nonlinear and non-stationary time series analysis. *Proceedings of the Royal Society A: Mathematical, Physical and Engineering Sciences*, 454(1971): 903–995.
- N.E. Huang, M.-L.C. Wu, S. R. Long, S.S.P. Shen, W. Qu, P. Gloersen, and K.L. Fan. 2003. A confidence limit for the empirical mode decomposition and Hilbert spectral analysis. *Proceedings of the Royal Society of London A: Mathematical, Physical and Engineering Sciences*, 459(2037):2317–2345.
- Y. Huang, L. Biferale, E. Calzavarini, C. Sun, and F. Toschi. 2013. Lagrangian single-particle turbulent statistics through the Hilbert-Huang transform. *Physical Review E*, 87(4):041003.
- P.R. Hurrell, R. Philipson, K.F. Carter, L. Davenport, and K. Wright. 2015. High Cycle Thermal Fatigue Analysis of Pipe Mixing Tee with Internal Sleeve. In *Transactions, SMiRT-23*, page 10, Manchester.
- Y. Hytönen. 1998. Two leakages induced by thermal stratification at the Loviisa power plant. In *Proceedings of the Nuclear Energy Agency*, pages 115–127. Committee on the Safety of Nuclear Installations.
- B. Iglewicz and D.C. Hoaglin. 1993. *How to Detect and Handle Outliers*, volume 16 of *ASQC basic references in quality control*. ASQC Quality Press.
- H.-Y. Jang, P.-C. Tuan, T.-C. Chen, and T.-S. Chen. 2006. Input estimation method combined with the finite-element scheme to solve IHCP hollow-cylinder inverse heat conduction problems. *Numerical Heat Transfer, Part A: Applications*, 50(3):263–280.

- S.T. Jayaraju, E.M.J. Komen, and E. Baglietto. 2010. Suitability of wall-functions in Large Eddy Simulation for thermal fatigue in a T-junction. *Nuclear Engineering and Design*, 240(10):2544–2554. ISSN 00295493.
- M.J. Jhung. 2013. Assessment of thermal fatigue in mixing tee by FSI analysis. *Nuclear Engineering and Technology*, 45(1):99–106.
- JSME. 2003. Guideline for evaluation of high-cycle thermal fatigue of a pipe. *S017-2003*.
- J. Kaipio and E. Somersalo. 2005. *Statistical and computational inverse problems*, volume 160 of *Applied Mathematical Sciences*. Springer. ISBN 978-0-387-27132-3.
- M. Kamaya and K. Miyoshi. 2017. Thermal fatigue damage assessment at mixing tees (elastic-plastic deformation effect on stress and strain fluctuations). *Nuclear Engineering and Design*, 318:202–212.
- M. Kamaya and A. Nakamura. 2011. Thermal stress analysis for fatigue damage evaluation at a mixing tee. *Nuclear Engineering and Design*, 241(8):2674–2687.
- H. Kamide, M. Igarashi, S. Kawashima, N. Kimura, and K. Hayashi. 2009. Study on mixing behavior in a tee piping and numerical analyses for evaluation of thermal striping. *Nuclear Engineering and Design*, 239(1):58–67.
- N. Kasahara, H. Takasho, and A. Yacumpai. 2002. Structural response function approach for evaluation of thermal striping phenomena. *Nuclear Engineering and Design*, 212(1):281–292.
- T. Kawamura, K. Shiina, and M. Ohtsuka. 2003. Study on high-cycle fatigue evaluation for thermal striping in mixing tees with hot and cold water. 2. Type B: characteristics of temperature fluctuations and heat transfer in mixing tees with same pipe diameters. In *ICONE-11: Proceedings of the 11th International Conference on Nuclear Engineering*. Japan Society of Mechanical Engineers.
- J.D. Keller, A.J. Bilanin, A.E. Kaufman, and J. Carey. 2004. Thermal cycling screening criteria and evaluation methodology and application to pressurized water reactor branch line piping. In *Proceedings of the third international conference on fatigue of reactor components, Report NEA/CSNI*.
- J. Kickhofel, H.-M. Prasser, P. Karthick Selvam, E. Laurien, and R. Kulenovic. 2016. T-junction cross-flow mixing with thermally driven density stratification. *Nuclear Engineering and Design*, 309:23–39.
- S.-H. Kim, N.-S. Huh, M.-K. Kim, D.-G. Cho, Y.-H. Choi, J.-H. Lee, and J.-B. Choi. 2013. Hydro-thermo-mechanical analysis on high cycle thermal fatigue induced by thermal striping in a T-junction. *Journal of Mechanical Science and Technology*, 27(10):3087–3095.

- J.H. Konrad. 1977. *An Experimental Investigation of Mixing in Two-dimensional Turbulent Shear Flows with Applications to Diffusion-limited Chemical Reactions*. PhD thesis, California Institute of Technology.
- K.M. Konsoer and B.L. Rhoads. 2014. Spatial-temporal structure of mixing interface turbulence at two large river confluences. *Environmental Fluid Mechanics*, 14(5):1043–1070.
- C.G. Koop and F.K. Browand. 1979. Instability and turbulence in a stratified fluid with shear. *Journal of Fluid Mechanics*, 93(01):135–159.
- D. Krawczyk-Stańdo and M. Rudnicki. 2007. Regularization parameter selection in discrete ill-posed problems – the use of the U-curve. *International Journal of Applied Mathematics and Computer Science*, 17(2):157–164.
- J. Krejsa, K.A. Woodbury, J.D. Ratliff, and M. Raudensky. 1999. Assessment of strategies and potential for neural networks in the inverse heat conduction problem. *Inverse Problems in Engineering*, 7(3):197–213.
- A.K. Kuczaj and E.M.J. Komen. 2010. An Assessment of Large-Eddy Simulation Toward Thermal Fatigue Prediction. *Nuclear Technology*, 170(1):2–15.
- S. Kuhn, O. Braillard, B. Ničeno, and H.-M. Prasser. 2010. Computational study of conjugate heat transfer in T-junctions. *Nuclear Engineering and Design*, 240(6):1548–1557.
- M. Kuschewski, R. Kulenovic, and E. Laurien. 2013. Experimental setup for the investigation of fluid-structure interactions in a T-junction. *Nuclear Engineering and Design*, 264:223–230. ISSN 0029-5493.
- J. Li, J. Xie, and J. Zou. 2011. An adaptive finite element reconstruction of distributed fluxes. *Inverse Problems*, 27(7):075009.
- E. Lillberg. 2013. Predicting Thermal Mixing and Fatigue Inside Control Rod Guide Tubes. In *21st International Conference on Nuclear Engineering*, volume 3: Nuclear Safety and Security; Codes, Standards, Licensing and Regulatory Issues; Computational Fluid Dynamics and Coupled Codes, page V003T10A042, Chengdu, China. ASME.
- A. Logg, K.-A. Mardal, and G. Wells. 2012. *Automated solution of differential equations by the finite element method: The FEniCS book*, volume 84 of *Lecture Notes in Computational Science and Engineering*. Springer. ISBN 978-3-642-23099-8.
- S. Lu, Y. Heng, and A. Mhamdi. 2012. A robust and fast algorithm for three-dimensional transient inverse heat conduction problems. *International Journal of Heat and Mass Transfer*, 55(25-26):7865–7872.

- M. Maegawa. 2006. Thermal fatigue of quench hydrogen piping. In *19th Symposium on the Maintenance of Equipments (The Japan Petroleum Institute)*, pages 12–17.
- M. McDevitt, T. Childress, M. Hoehn, and R. McGill. 2015. Analysis and impact of recent thermal fatigue operating experience in the USA. In *OECD/NEA CSNI WGIAGE; Fourth International Conference on Fatigue of Nuclear Reactor Components*.
- H.-B. Meng, Z.-Q. Liu, Y.-F. Yu, Q. Xiong, and J.-H. Wu. 2011. Intrinsic mode entropy analysis of tube-wall pressure fluctuation signals in the Kenics Static Mixer. *International Journal of Chemical Reactor Engineering*, 9(1).
- F.R. Menter. 2015. Best practice: scale-resolving simulations in ANSYS CFD. Technical report, ANSYS GmbH.
- D. Meresse, S. Harmand, M. Siroux, M. Watremez, and L. Dubar. 2012. Experimental disc heat flux identification on a reduced scale braking system using the inverse heat conduction method. *Applied Thermal Engineering*, 48:202–210.
- K.-J. Metzner and U. Wilke. 2005. European THERFAT project – thermal fatigue evaluation of piping system “Tee”-connections. *Nuclear Engineering and Design*, 235(2–4):473–484. ISSN 0029-5493.
- K. Miyoshi, A. Nakamura, Y. Utanohara, and N. Takenaka. 2014. An investigation of wall temperature characteristics to evaluate thermal fatigue at a T-junction pipe. *Mechanical Engineering Journal*, 1(5):TEP0050–TEP0050.
- M. Mohammadiun. 2016. Time-dependent heat flux estimation in multi-layer systems by inverse method. *Journal of Thermophysics and Heat Transfer*, 30(3): 599–607.
- M.J. Mohlenkamp and M.C. Pereyra. 2008. *Wavelets, their friends, and what they can do for you*. European Mathematical Society.
- P. Movahed and E. Johnsen. 2015. The mixing region in freely decaying variable-density turbulence. *Journal of Fluid Mechanics*, 772:386–426.
- V.S. Naik-Nimbalkar, A.W. Patwardhan, I. Banerjee, G. Padmakumar, and G. Vaidyanathan. 2010. Thermal mixing in T-junctions. *Chemical Engineering Science*, 65(22):5901–5911.
- J.T. Nakos. 2004. Uncertainty analysis of thermocouple measurements used in normal and abnormal thermal environment experiments at Sandia’s Radiant Heat Facility and Lurance Canyon Burn Site. Technical report, Sandia National Laboratories.

- National Instruments. 2004. SCXI-32 Channel Analog Input Modules. <https://manualzz.com/download/21252315>. Online; accessed 30 September 2018.
- National Instruments. 2008. NI 6023E/6024E/6025E Family Specifications. <http://www.ni.com/pdf/manuals/370719c.pdf>. Online; accessed 30 September 2018.
- National Instruments. 2016. Aliasing and Sampling at Frequencies Above the Nyquist Frequency. <https://www.scribd.com/document/305478691/NI-Tutorial-3000-En>. Online; accessed 30 September 2018.
- F. Nicoud and F. Ducros. 1999. Subgrid-scale stress modelling based on the square of the velocity gradient tensor. *Flow, Turbulence and Combustion*, 62(3):183–200. ISSN 13866184.
- F. Nicoud, H. Baya Toda, O. Cabrit, S. Bose, and J. Lee. 2011. Using singular values to build a subgrid-scale model for large eddy simulations. *Physics of Fluids*, 23(8):085106.
- M. Niknam Shahrak, A. Shahsavand, and A. Okhovat. 2013. Robust PSD determination of micro and meso-pore adsorbents via novel modified U curve method. *Chemical Engineering Research and Design*, 91(1):51–62. ISSN 02638762.
- J. Nocedal and S. Wright. 2006. *Numerical optimization*, 2nd edition. Springer Series in Operations Research and Financial Engineering. Springer. ISBN 978-0-387-40065-5.
- Y. Odemark, T.M. Green, K. Angele, J. Westin, F. Alavyoon, and S. Lundström. 2009. High-Cycle Thermal Fatigue in Mixing Tees: New Large-Eddy Simulations Validated Against New Data Obtained by PIV in the Vattenfall Experiment. In *Proceedings of the 17th International Conference on Nuclear Engineering ICONE17*, pages 775–785. ASME.
- OpenFOAM. 2017. *User Guide version 5.0*. The OpenFOAM Foundation.
- H.R.B. Orlande and G.S. Dulikravich. 2012. Inverse heat transfer problems and their solutions within the Bayesian framework. In *ECCOMAS Special Interest Conference – Numerical Heat Transfer*.
- C. Ould-Lahoucine. 2004. A Duhamel integral based solution for the sideways heat equation applied to the non-intrusive temperature measurement. *International Communications in Heat and Mass Transfer*, 31(8):1037–1045.
- C. Ould-Lahoucine and A. Khellaf. 2005. Dynamic characterization of a thermocouple in a fluid crossflow. *Sensors and Actuators A*, 119:48–56.
- M.N. Özisik and H.R.B. Orlande. 2000. *Inverse heat transfer: fundamentals and applications*. CRC Press. ISBN 9781560328384.

- E. Paffumi, K.-F. Nilsson, and Z. Szaraz. 2015. Experimental and numerical assessment of thermal fatigue in 316 austenitic steel pipes. *Engineering Failure Analysis*, 47:312–327. ISSN 13506307.
- T. Pasutto, C. Peniguel, and M. Sakiz. 2005. Chained computations using an unsteady 3D approach for the determination of thermal fatigue in a T-junction of a PWR nuclear plant. In *ASME-PVP Conference*.
- S. Patankar. 1980. *Numerical heat transfer and fluid flow*. CRC Press.
- M.C. Peel, T.A. McMahon, and G.G.S. Pegram. 2009. Assessing the performance of rational spline-based empirical mode decomposition using a global annual precipitation dataset. *Proceedings of the Royal Society of London A: Mathematical, Physical and Engineering Sciences*, 465(2106):1919–1937.
- R. Pegonen, N. Edh, K. Angele, and H. Anglart. 2014. Investigation of Thermal Mixing in the Control Rod Top Tube Using Large Eddy Simulations. *Journal of Power Technologies*, 94(1):67–78.
- S. Qian, S. Kanamaru, and N. Kasahara. 2015. High-accuracy CFD prediction methods for fluid and structure temperature fluctuations at T-junction for thermal fatigue evaluation. *Nuclear Engineering and Design*, 288:98–109.
- V. Radu, E. Paffumi, N. Taylor, and K.-F. Nilsson. 2009. A study on fatigue crack growth in the high cycle domain assuming sinusoidal thermal loading. *International Journal of Pressure Vessels and Piping*, 86(12):818–829.
- V. Radu, N. Taylor, and E. Paffumi. 2008. Development of new analytical solutions for elastic thermal stress components in a hollow cylinder under sinusoidal transient thermal loading. *International Journal of Pressure Vessels and Piping*, 85(12):885–893.
- H.-J. Reinhardt, D. N. Hào, J. Frohne, and F.-T. Suttmeier. 2007. Numerical solution of inverse heat conduction problems in two spatial dimensions. *Journal of Inverse and Ill-posed Problems*, 15(2):181–198.
- G. Rilling, P. Flandrin, and P. Gonçalvès. 2003. On empirical mode decomposition and its algorithms. In *Proceedings of IEEE-EURASIP Workshop on Nonlinear Signal and Image Processing NSIP-03*.
- A. Sakowitz. 2013. *Computation and Analysis of EGR Mixing in Internal Combustion Engine Manifolds*. PhD thesis, KTH, Mechanics.
- A. Sakowitz, M. Mihaescu, and L. Fuchs. 2014. Turbulent flow mechanisms in mixing T-junctions by large eddy simulations. *International Journal of Heat and Fluid Flow*, 45:135–146.

- J. Schijve. 2009. *Fatigue of structures and materials*, 2nd edition. Springer, Dordrecht. ISBN 978-1-4020-6808-9.
- X. Schuler, E. Laurien, K.H. Herter, S. Moogk, D. Klören, R. Kulenovic, and M. Kuschewski. 2012. Thermal fatigue: fluid–structure interaction at thermal mixing events. In *38th MPA Seminar: “Energieerzeugung und Energieeffizienz - Werkstoffe und Bauteilverhalten”*.
- P. Karthick Selvam, R. Kulenovic, E. Laurien, J. Kickhofel, and H.-M. Prasser. 2017. Thermal mixing of flows in horizontal T-junctions with low branch velocities. *Nuclear Engineering and Design*, 322:32–54.
- V.N. Shah, A.G. Ware, C.L. Atwood, M.B. Sattison, R.S. Hartley, and C. Hsu. 1999. Assessment of field experience related to pressurized water reactor primary system leaks. *ASME-PUBLICATIONS-PVP*, 395:23–32.
- JAHM Software Inc. 2015. Material Properties Database (MPDB) v. 8.21. North Reading, USA. <https://www.jahm.com/>.
- H. Song, Y. Bai, L. Pinheiro, C. Dong, X. Huang, and B. Liu. 2012. Analysis of ocean internal waves imaged by multichannel reflection seismics, using ensemble empirical mode decomposition. *Journal of Geophysics and Engineering*, 9(3):302.
- STAR-CCM+. 2018. *User Manual. V13.02.011*. CD-adapco.
- T. Sugano, T. Sakai, T. Ueno, and Y. Kutomi. 2000. Leakage from CVCS pipe of regenerative heat exchanger induced by high-cycle thermal fatigue at Tsuruga Nuclear Power Station Unit 2. In *Proceedings of NTHAS2: Second Japan-Korea Symposium on Nuclear Thermal Hydraulics and Safety*. Atomic Energy Society of Japan.
- P.K. Sweby. 1984. High resolution schemes using flux limiters for hyperbolic conservation laws. *SIAM journal on numerical analysis*, 21(5):995–1011.
- G.R. Tabor and M.H. Baba-Ahmadi. 2010. Inlet conditions for large eddy simulation: A review. *Computers and Fluids*, 39(4):553–567. ISSN 00457930.
- S. Taheri, L. Vincent, and J.-C. Le-roux. 2013. A new model for fatigue damage accumulation of austenitic stainless steel under variable amplitude loading. *Procedia Engineering*, 66:575–586.
- J. Taler and P. Duda. 2006. *Solving Direct and Inverse Heat Conduction Problems*. Springer, Dordrecht.
- J. Taler, B. Węglowski, W. Zima, S. Grądziel, and M. Zborowski. 1997. Monitoring of transient temperature and thermal stresses in pressure components of steam boilers. *International journal of pressure vessels and piping*, 72(3):231–241.

- M.T. Taner, F. Koehler, and R.E. Sheriff. 1979. Complex seismic trace analysis. *Geophysics*, 44(6):1041–1063.
- M.P. Tarvainen, P.O. Ranta-Aho, P.A. Karjalainen, *et al.* 2002. An advanced detrending method with application to HRV analysis. *IEEE Transactions on Biomedical Engineering*, 49(2):172–175.
- R. Thiele. 2015. *Mechanistic Modeling of Wall-Fluid Thermal Interactions for Innovative Nuclear Systems*. PhD thesis.
- R. Throne and L. Olson. 2001. The steady inverse heat conduction problem: A comparison of methods with parameter selection. *Journal of Heat Transfer*, 123(4):633–644.
- N. Tian, W. Xu, J. Sun, and C.-H. Lai. 2011. Estimation of unknown heat source function in inverse heat conduction problems using quantum-behaved particle swarm optimization. *International Journal of Heat and Mass Transfer*, 54(17):4110–4116.
- A.N. Tikhonov and V.Y. Arsenin. 1977. *Solutions of ill-posed problems*. Scripta series in mathematics. V.H. Winston & Sons. ISBN 0-470-99124-0.
- A. Timperi. 2014. Conjugate heat transfer LES of thermal mixing in a T-junction. *Nuclear Engineering and Design*, 273.
- H. Tinoco. 2013. CFD as a Tool for the Analysis of the Mechanical Integrity of Light Water Nuclear Reactors. In *Nuclear Reactor Thermal Hydraulics and Other Applications*. InTech. ISBN 978-953-51-0987-7.
- H. Tinoco, A. Darelius, E. Bernerskog, and H. Lindqvist. 2009. Forsmark 3 - time dependent flow simulations of the mixing process between crud and bypass flows inside the control rod guide tube. Technical Report FT-2008-3425, Forsmark.
- H. Tinoco, H. Lindqvist, Y. Odemark, C.-M. Högström, and K. Angele. 2010. Flow Mixing Inside a Control-Rod Guide Tube – Part I: CFD Simulations. In *18th International Conference on Nuclear Engineering*, pages 645–654, Xi’an, China. ASME.
- M. Torbacke and Å. C. Rasmuson. 2004. Mesomixing in semi-batch reaction crystallization and influence of reactor size. *AIChE Journal*, 50(12):3107–3119.
- M.E. Torres, M. A. Colominas, G. Schlotthauer, and P. Flandrin. 2011. A complete ensemble empirical mode decomposition with adaptive noise. In *2011 IEEE International Conference on Acoustics, Speech and Signal Processing (ICASSP)*, pages 4144–4147. IEEE.
- R. Tuominen. 2015. Coupling Serpent and OpenFOAM for neutronics-CFD multi-physics calculations. Master’s thesis, Aalto University.

- F.S. Viloche Bazán. 2008. Fixed-point iterations in determining Tikhonov regularization parameter. *Inverse Problems*, 24(3).
- W. Wagner, J. R. Cooper, A. Dittmann, J. Kijima, H.-J. Kretzschmar, A. Kruse, R. Mareš, K. Oguchi, H. Sato, I. Stöcker, O. Šifner, Y. Takaishi, I. Tanishita, J. Trübenbach, and Th. Willkommen. 2000. The IAPWS Industrial Formulation 1997 for the Thermodynamic Properties of Water and Steam. *Journal of Engineering for Gas Turbines and Power*, 122(1):150.
- C. Walker, M. Simiano, R. Zboray, and H.-M. Prasser. 2009. Investigations on mixing phenomena in single-phase flow in a T-junction geometry. *Nuclear Engineering and Design*, 239:116–126.
- J. Westin, F. Alavyoon, L. Andersson, and P. Veber. 2006. Experiments and unsteady CFD-calculations of thermal mixing in a T-junction. In *Proceedings of the workshop on Benchmarking of CFD Codes for Application to Nuclear Reactor Safety (CFD4NRS)*, pages 494–508.
- J. Westin, P. Veber, L. Andersson, C. ‘t Mannetje, U. Andersson, J. Eriksson, M.E. Henriksson, F. Alavyoon, and C. Andersson. 2008. High-Cycle Thermal Fatigue in Mixing Tees: Large-Eddy Simulations Compared to a New Validation Experiment. In *16th International Conference on Nuclear Engineering*, volume 2: Fuel Cycle and High Level Waste Management; Computational Fluid Dynamics, Neutronics Methods and Coupled Codes; Student Paper Competition, pages 515–525.
- J. Wilson, C. Currie, M. Jones, and L. Davenport. 2016. A Case Study Evaluating the Effects of High Cycle Thermal Loading Within a Pressurised Water Reactor Mixing Tee Using Conjugate CFD/FE Methods. In *ASME 2016 Pressure Vessels and Piping Conference*, page V003T03A050, Vancouver, British Columbia, Canada. American Society of Mechanical Engineers.
- Z. Wu and N.E. Huang. 2009. Ensemble empirical mode decomposition: a noise-assisted data analysis method. *Advances in Adaptive Data Analysis*, 01(01):1–41.
- Z. Yang, B. W.-K. Ling, and C. Bingham. 2013. Trend extraction based on separations of consecutive empirical mode decomposition components in Hilbert marginal spectrum. *Measurement*, 46(8):2481–2491.
- J.-R. Yeh, J.-S. Shieh, and N.E. Huang. 2010. Complementary ensemble empirical mode decomposition: A novel noise enhanced data analysis method. *Advances in Adaptive Data Analysis*, 2(02):135–156.
- Y. Zhang and T. Lu. 2016. Study of the quantitative assessment method for high-cycle thermal fatigue of a T-pipe under turbulent fluid mixing based on the coupled CFD-FEM method and the rainflow counting method. *Nuclear Engineering and Design*, 309:175–196.

O.C. Zienkiewicz, R.L. Taylor, and J.Z. Zhu. 2005. *The Finite Element Method: Its Basis and Fundamentals (6th Ed.)*. Elsevier, Butterworth-Heinemann. ISBN 9780080472775.